Experimental and Theoretical Studies on Unmixed Combustion for Heat Transfer Applications

THESIS

Submitted in partial fulfillment
of the requirements for the degree of
DOCTOR OF PHILOSOPHY

by

DESHPANDE AMOL ANILRAO

Under the Supervision of
Prof. Srinivas Krishnaswamy

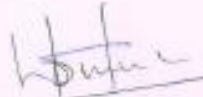**BIRLA INSTITUTE OF TECHNOLOGY AND SCIENCE, PILANI**
2016

BIRLA INSTITUTE OF TECHNOLOGY AND SCIENCE, PILANI

CERTIFICATE

This is to certify that the thesis entitled "Experimental and Theoretical Studies on Unmixed Combustion for Heat Transfer Applications" and submitted by DESHPANDE AMOL ANILRAO ID No 2010PHXF442G for award of Ph.D. of the Institute embodies original work done by him under my supervision.

Signature of the Supervisor

Name in capital letters   PROF. SRINIVAS KRISHNASWAMY

Designation   Professor

Date: 12|12|16

ABSTRACT

Unmixed Combustion (UMC), a novel variant of combustion, occurs when air and fuel alternately pass over an Oxygen Storage and Release Material (OSRM), mainly metal/metal oxides which undergo oxidation and reduction reactions. In this study, the potential of UMC is demonstrated for heat transfer applications. A purpose-built test rig, based on a dynamically operated Packed Bed Reactor (PBR) concept was designed, fabricated and commissioned. Experiments were conducted using a Cu based OSRM along with methane (CH_4) and zero air (21 mol% O_2) as reactive gases. The energy generated in both oxidation and reduction due to exothermicity was radially transferred by conduction and convection to coolant air. For a specific loading of 1.25 kg of OSRM and fixed reaction cycle times, the effect of varying zero air, coolant and CH_4 flowrate and reactive gas inlet temperature on the radial heat transfer was investigated. The radial heat transfer rate was maximized at 95 ± 2 % of total energy in the bed at an inlet temperature of 873.15 K and zero air, coolant and CH_4 flowrates of 15 LPM, 150 LPM and 2 LPM (corresponding to 10 mol % concentration) respectively. Under "cyclic" steady state conditions, the variation of bed temperature and coolant outlet temperature was restricted to within ± 30 K and ± 3 K respectively and the combustion process was observed to be self-sustaining.

In addition a separate experimental investigation related to estimating kinetic parameters of oxidation of Cu and reduction of CuO, encountered in UMC, was carried out using a Pulsed Micro-reactor (PMR) technique. Plug flow condition in the reactor, essential for accurate estimation of kinetic parameters, was confirmed using a Residence Time Distribution (RTD) approach. A simple generic methodology, based on a uniform reaction model is presented and has been validated for both reactions which were found to be surface reaction controlled. The estimated values of reaction orders and activation energies for both reactions and the pre-exponential factor for oxidation were found to be in good agreement with those obtained using Thermo Gravimetric Analysis (TGA). A lower value of pre-exponential factor for reduction however was obtained.

A dynamic, 2-D pseudo-homogeneous model for UMC based PBR, integrated with heat transfer to a coolant has also been developed. A commercial software COMSOL^{TM} was used for model implementation. The model predicts the temperature profiles in the bed and total heat transfer for prescribed operating conditions used in the experimental runs. The model results obtained for one cycle comprising of oxidation and reduction were compared with experimental data and good agreement to within ± 9 % was obtained in all cases. No adjustment factors were incorporated in the model.

The results obtained present a strong argument for using UMC based reactor systems as an alternative to "premixed" combustion for process heat transfer applications subject to suitable combination of operating conditions inclusive of cycle time, reactor material of construction and choice of OSRM. PMR technique was found to be a simple and viable alternative to determine kinetics of non-catalytic gas-solid reactions. The study also validates the use of a pseudo-homogeneous model in predicting the behaviour of dynamically operated UMC systems under relatively mild conditions.

ACKNOWLEDGMENTS

Dedicated to my Parents

<u>CONTENTS</u>

Nomenclature

Symbols

a	stoichiometric coefficient of solid reactant
a_c	external surface area per unit volume of catalyst bed ($m^2\,m^{-3}$)
A_o	number of moles present in one pulse of reactive gas (mol)
b	stoichiometric coefficient of gaseous reactant
c_g	concentration of gaseous reactant (mol m^{-3})
c_{gi}	concentration of gaseous reactant at the end of ith pulse (mol m^{-3})
c_{go}	initial concentration of gaseous reactant (mol m^{-3})
$c_{go,N}$	initial concentration of gaseous reactant (based on N pulses) (mol m^{-3})
c_{gs}	concentration of gaseous reactant on the surface of the catalyst (mol m^{-3})
c_s	concentration of solid reactant (mol m^{-3})
c_{si}	concentration of solid reactant at the end of ith pulse (mol m^{-3})
c_{so}	initial concentration of the solid reactant (mol m^{-3})
C_{pc}	specific heat at constant pressure of coolant ($J\,mol^{-1}K^{-1}$)
C_{pg}	specific heat at constant pressure of gaseous component ($J\,mol^{-1}K^{-1}$)
C_{ps}	specific heat at constant pressure of solid component ($J\,mol^{-1}K^{-1}$)
C_{WP}	Weisz- Prater parameter
d_p	average particle diameter (m)
d_t	diameter of reactor tube (m)
D_{AB}	gas phase molecular diffusivity ($m^2\,s^{-1}$)
D_e	effective diffusivity ($m^2\,s^{-1}$)
D_{er}	effective radial mass dispersion coefficient (m^2s^{-1})
D_{ez}	effective axial mass dispersion coefficient (m^2s^{-1})
Di	Dispersion number
e	thermo-emf
E	activation energy ($J\,mol^{-1}$)
G	component of rate of deformation in $k-\epsilon$ turbulent model ($m^{-1}s^{-1}$)

h_c	heat transfer coefficient – coolant section (W m^{-2} K^{-1})
h_e	effective heat transfer coefficient (W m^{-2} K^{-1})
h_w	wall heat transfer coefficient (W m^{-2} K^{-1})
ΔH_{rx}	standard heat of reaction (J mol^{-1})
ΔH_{rxn}^o	standard enthalpy of reaction (kJ mol^{-1})
i	pulse number
k	turbulent kinetic energy (m^{2}s^{-2})
k_c	external mass transfer coefficient (m s^{-1})
k_e	effective reaction rate constant (mol^{1-m-n} m$^{3m+3n-3}$ s^{-1})
k''_e	effective reaction rate constant (mol^{1-m-n} m$^{3m+3n-2}$ s^{-1})
k_o	pre-exponential factor (mol^{1-m-n} m$^{3m+3n-3}$ s^{-1})
k_o''	pre-exponential factor (mol^{1-m-n} m$^{3m+3n-2}$ s^{-1})
k_1''	reaction rate constant (mol^{1-m-n} m$^{3m+3n-2}$ s^{-1})
$L1$	length of inert domain – I in physical model (m)
m	reaction order with respect to solid reactant
$\dot{m}_c$	coolant mass flowrate (kg s^{-1})
M_g	molecular weight of gas (O$_2$, N$_2$, CH$_4$) (g mol^{-1})
M_s	molecular weight of solid (Cu, CuO) (g mol^{-1})
n	reaction order with respect to gaseous reactant
n_c	number of cycles
N	total number of pulses required to completely convert solid reactant
P_b	pressure in the packed bed section (Pa)
P_c	pressure in the coolant section (Pa)
P_g	pressure of the gas stream (Pa)
$Pe_{m,r}$	Peclet number (mass transfer)
q	carrier gas flowrate (m^3 s^{-1})
q_c	inward heat flux of coolant section (W m^{-2})
Q	total amount of energy generated due to reaction (J)
Q_c	total energy transfer to coolant (J)
$\dot{Q}_{ext}$	external power supply (W)

Q_{ext}	external energy supplied (J)
r	radial coordinate (m)
$-r_g$	rate of reaction ((mol of gas) m^{-3} s^{-1})
$-r''_g$	rate of reaction ((mol of gas) m^{-2} s^{-1})
$-r''_g(exp)$	experimental rate of reaction ((mol of gas) m^{-2} s^{-1})
$-r_s$	rate of reaction (mol of solid component m^{-3} s^{-1})
$-r''_s$	rate of reaction ((mol of solid component) m^{-2} s^{-1})
R	average radius of the particle (m)
R'	Universal gas constant (J mol^{-1}K^{-1})
R_i	radius of the inner pipe of an annular reactor system (m)
R_o	radius of the outer pipe of an annular reactor system (m)
Re_p	Reynolds number, $Re_p = Ud_p\rho_g/\mu$
S_a	specific surface area (m^2 (kg of catalyst)$^{-1}$)
S_o	chromatogram area for reference gas peak (m^2)
S_i	chromatogram area for unreacted gas peak for i^{th} pulse (m^2)
Sc	Schmidt number, $Sc = \mu/\rho_g D_{AB}$
Sh	Sherwood number, $Sh = k_c d_p/D_{AB}$
t	time (s)
t_1	time at which a reduction-oxidation cycle starts (s)
t_2	time at which a reduction-oxidation cycle ends (s)
t_c	cycle time (s)
T	thermodynamic temperature (K)
T_b	temperature in the packed bed section (K)
T_{bo}	initial temperature of packed bed section (K)
T_c	time averaged coolant temperature (K)
T_{co}	initial temperature of coolant section (K)
T_g	temperature of the gas stream (K)
$T_{b,PMR}$	temperature of the solid bed in Pulsed Micro-reactor (K)
T_w	reactor wall temperature (K)
ΔT_c	coolant temperature rise (K)

U	superficial velocity of carrier gas (m s^{-1})
v_c	time averaged coolant velocity (m s^{-1})
$v_{c,r}$	time averaged radial component of coolant velocity (m s^{-1})
$v_{c,z}$	time averaged axial component of coolant velocity (m s^{-1})
v_g	reactive gas velocity (m s^{-1})
V_b	active bed reactor volume (m^3)
$\dot{V}_c$	volumetric flowrate of coolant (m^3 s^{-1})
$\dot{V}_g$	volumetric flowrate of gas stream (m^3 s^{-1})
$\dot{V}_{g,ind}$	volumetric flowrate of gas stream indicated by flowmeters (m^3 s^{-1})
w_{act}	mass fraction of reactive material in the solid
w_g	mass fraction of gaseous component
w_h	heat front velocity (m s^{-1})
w_r	reaction front velocity (m s^{-1})
w_s	mass fraction of solid component
X	conversion
z	axial coordinate (m)

Greek Letters

ε_g	bed voidage
ε_p	particle porosity
ϵ	dissipation rate of turbulent kinetic energy (m^{2}s^{-3})
η	internal effectiveness factor
λ	thermal conductivity (W m^{-1}K^{-1})
λ_c	thermal conductivity of coolant (W m^{-1}K^{-1})
λ_{er}	effective radial thermal conductivity (W m^{-1}K^{-1})
λ_{ez}	effective axial thermal conductivity (W m^{-1}K^{-1})
λ_g	thermal conductivity of pure gaseous component (W m^{-1}K^{-1})
λ_s	thermal conductivity of pure solid component (W m^{-1}K^{-1})
μ	viscosity (Pa.s)

μ_{T} turbulent viscosity (Pa.s)

ρ_{b} solid bed density (kg m^{-3})

ρ_{c} time averaged density of coolant (kg m^{-3})

ρ_{g} density of gaseous reactant (kg m^{-3})

ρ_{s} density of solid component (kg m^{-3})

Subscripts

act   actual operating conditions

cal   operating parameter at which the flowmeter is calibrated for

in   inlet conditions

ox   oxidation

red   reduction

Abbreviations

CLC   Chemical Looping Combustion

OSRM   Oxygen Storage and Release Material

PBR   Packed Bed Reactor

PMR   Pulsed Micro-Reactor

RTD   Residence Time Distribution

TAP   Temporal Analysis of Products

TGA   Thermo Gravimetric Analysis

UMC   Unmixed Combustion

List of Figures

List of Tables

Chapter 1

Introduction

Over the years, combustion has been largely based on "premixing" fossil fuel with excess air in a closed firebox and heating it to produce hot flue gas. The enthalpy of this gas can subsequently be transferred primarily via convection and radiation and used for process applications. This process however has following limitations:

1. NO_x and carbon dioxide (CO_2) emissions in flue gas
2. Difficulties in CO_2 capture from the flue gas
3. Reduced thermal efficiency due to stack losses
4. Excess entropy generation due to high temperatures involved

These limitations pose a dual challenge of improving thermal efficiency and reducing the impact on environment simultaneously. Several researchers have attempted addressing the above issues based on system improvements post combustion or investigating pre-combustion based technologies like gasification and oxy-fuel combustion. The emphasis of these investigations however has been on energy recovery and CO_2 capture for reuse or sequestration. Very few attempts have been made to investigate the possibility of changing the fundamental nature of the combustion process itself which on the whole involves "premixing" fuel and air or oxygen (O_2) along with heat to produce fire inside the firebox.

In this context, it is proposed to investigate the potential of a novel Unmixed Combustion (UMC) process involving an Oxygen Storage and Release Material (OSRM). This process referred to as an "alternative to fire" occurs when air and fuel in alternate cycles pass over the OSRM that undergoes oxidation and reduction. These reactions if exothermic, can release energy in the form of heat that can potentially be transferred by conduction and convection to be subsequently utilized in process applications. Unreacted O_2 and nitrogen exit during oxidation while CO_2 and steam are produced in the reduction

cycle. The pure CO_2 is then available for storage, sequestration or reuse purposes without any additional unit operations except condensing water out. As this process operates at relatively lower temperatures than "premixed" combustion without generating flames, the amount of excess entropy generation can be reduced and formation of NO_x can be avoided. However, the practical possibility of effectively transferring energy from endothermic or exothermic reactions in alternate cycles by conduction and convection on a sustained basis is a challenge and has not been investigated till date.

In the present study, the potential of a dynamically operated UMC based packed bed reactor using representative copper based OSRM has been experimentally investigated for heat transfer applications. This OSRM was chosen because of its high reactivity and stability and that both oxidation-reduction reactions involved are exothermic. A proof-of-concept test rig was designed and fabricated for this purpose. Air was chosen as a representative coolant fluid in these studies. Careful experiments were conducted by using zero air and methane as reactive gases during oxidation and reduction cycles respectively. Reliable, accurate and repeatable measurements have been made covering a wide range of important parameters i.e. reactive gases and coolant flowrates, bed and coolant temperatures and product gas compositions. The radial energy transfer from the bed to coolant has been estimated. The effect of various parameters like reactive gas inlet temperature and reactive gas and coolant flowrates on the total heat transfer and OSRM bed temperature has been investigated.

The energy generation in the OSRM bed is a function of the reaction rate and the design of UMC reactor systems necessitates a knowhow of this rate. A Pulsed Micro-reactor (PMR) technique was used for this purpose and the concentration dependency and kinetic parameters of the non-catalytic gas-solid reactions involved were estimated. A Residence Time Distribution (RTD) approach was adopted to confirm plug flow conditions in this reactor, which is an essential criterion in using this system. A simple methodology to estimate kinetic parameters is proposed and has been validated using reactor data obtained for oxidation of Cu and reduction of copper (II) oxide (CuO), both of which were found to be surface reaction controlled. Reaction orders and values of effective rate

constant have been obtained for both reactions. The specific reaction rate constant and activation energy values have been estimated using Arrhenius equation and the results obtained have been compared with those reported in literature using Thermo Gravimetric Analysis (TGA).

A 2-D pseudo-homogeneous model was also developed to describe transient behaviour during progressive oxidation and reduction of an OSRM in a packed bed reactor. This model was used in conjunction with a standard approach for single phase turbulent flow heat transfer to give a complete model for a UMC – heat transfer system. The model predicts the temperature profiles in the bed along with the total radial heat transfer to coolant. The predicted results were compared and validated using experimental data. Simulation studies to investigate parametric effects on the bed temperature profile were also conducted.

Chapter 2

Literature Survey

2.1   Introduction

In the Unmixed Combustion (UMC) process, air and fuel in alternate cycles pass over an Oxygen Storage and Release Material (OSRM) resulting in oxidation and reduction of the material (Fig. 2.1). Since its introduction in 1993, the process has been studied in detail by several researchers. The main aspects of UMC, emphasized in these studies, include feasibility of this process for potential applications, selection of a suitable OSRM for a specific application, understanding the reaction kinetics involved and development of mathematical models to understand and predict the overall behavior of the system. The progress in each of these areas has been studied by reviewing work done by researchers over the years till date and is presented in detail in the following sections.
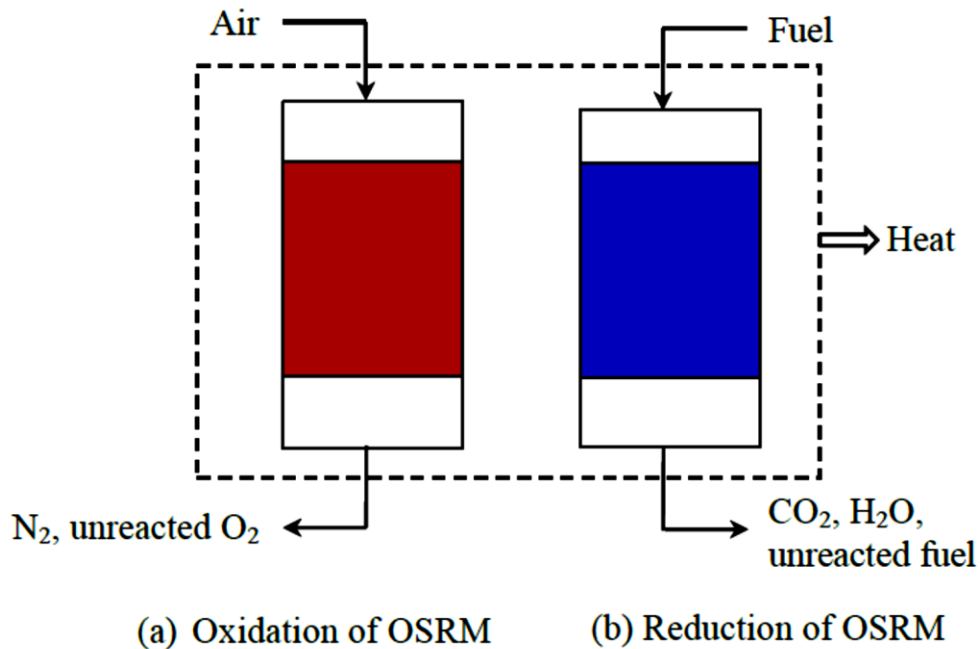
Fig. 2.1 Illustrative sketch of Unmixed Combustion (UMC) in a single reactor showing (a) oxidation and (b) reduction cycles separately

2.2   Unmixed Combustion (UMC)

UMC was first proposed by Lyon [1] in 1993 to be used in rotary kiln incinerators. UMC was used instead of "premixed" combustion in incinerators with an aim to avoid the release of products of incomplete combustion (i.e. puffs of volatile organic compounds) into the environment. In their experimental study, they used a fixed bed consisting of 25.5 wt% of copper (II) oxide (CuO) on alumina as an OSRM and proved that it was possible to oxidize 99.99% of 1900 – 2500 ppmC of various components like pyridine (C_5H_5N), chlorobenzene (C_6H_5Cl), etc. at reaction conditions of 1073.15 – 1093.15 K.

Lyon and Pittstown [2] subsequently studied UMC in detail and suggested methods and systems for transferring heat by using this process in 1998. In another study, Lyon and Cole [3] termed UMC as an alternative to fire and discussed the possible use of UMC for number of applications like providing heat for cold starting of engines, generation of inert gas for airplane fuel tanks, avoiding NO_x emissions and supplying heat for endothermic reactions like steam reforming.

In one of their experimental studies related to the application of transferring heat across a surface, they passed carbon monoxide (CO) and air alternately over 25 wt% copper (Cu) on alumina rings and the enthalpy of reaction was used for heating water, which resulted in a corresponding heat flux of 22.2 W/cm^2. This in turn corresponds to a firing density of 10.9 MW/m^3 as against 1 MW/m^3 typically observed in conventional boilers. The phenomenal increase in recovering energy was mainly due to heat transfer by conduction through the solid phase coupled with convection as against radiation and convection prevalent in "premixed" combustion based boiler systems. However, they have reported that the practical possibility of actually transferring energy in alternate cycles with sustained combustion will pose a major challenge which needs to be addressed.

GE global research team [4] have worked on catalytic unmixed combustion of coal with emphasis on reducing pollution and generating power, wherein the process involved simultaneously converting coal, steam and air, in a circulating fluidized bed, into two

separate streams of high pressure (300 psi) carbon dioxide (CO_2) – rich gas and high-temperature (1273.15 – 1623.15 K) high-pressure (300 – 400 psi) N_2 for producing electricity in gas turbine expanders. In their study, they performed lab scale tests with an objective to characterize metal oxide reduction behavior during the volatization step of coal gasification using 19% methane (CH_4) with N_2 in a fixed bed filled with coal and an iron (Fe) based OSRM. They investigated the effect of temperature, steam flowrate and OSRM to coal ratio on CH_4 reactivity. The results showed maximum CH_4 conversion with minimal CO formation in the temperature range of 1073.15 – 1123.15 K, at a steam flowrate of 1 mL/min and an OSRM to coal ratio of 4. Later they developed a pilot-scale facility using a fluidized bed containing riser (reactor 1) and regenerator (reactor 2) sections. But due to the potential failure of reactor 2, test runs were eventually conducted using reactor 1 by cycling it through both combustion/reduction and oxidation modes to understand the overall operation. The initial temperature for these runs was maintained at 1073.15 K. A coal slurry (45% by weight) was fluidized along with a Fe based OSRM. Steam was introduced in the reactor resulting in coal gasification and OSRM reduction which proceed as given below:

$$CH_{0.8} \text{ (coal)} + H_2O \rightarrow CO + 1.4H_2 \qquad \text{(Gasification)} \qquad (A)$$

$$CO + \text{Oxidized OSRM} \rightarrow CO_2 + \text{Reduced OSRM} \qquad \text{(Reduction using CO)} \qquad (B)$$

$$H_2 + \text{Oxidized OSRM} \rightarrow H_2O + \text{Reduced OSRM} \qquad \text{(Reduction using } H_2) \qquad (C)$$

These endothermic reactions caused the reactor temperature to drop quickly to 943.15 K and then stabilize. In the same reactor, the reduced OSRM was then fluidized using air. The temperature was found to increase in this case to 1073.15 K due to the high exothermicity of oxidation. The temperature decreased after about 7 minutes following which O_2 was detected in the product gases indicating that the OSRM was completely oxidized. Sintering of OSRM particles was observed at temperatures above 973.15 K, mainly because of melting of alkali metals present in the coal ash. While the operation of UMC for coal combustion using a single reactor was demonstrated, the team

faced difficulties in providing a robust auxiliary heating system to maintain required initial operating temperature for the gasification reaction and in removing ash from the OSRM. They also expressed concerns over long term activity and durability of the OSRM and its economic impact.

Researchers at Oak Ridge National Laboratory (ORNL) [5, 6] have done extensive work on the application of unmixed combustion to engines for transportation purposes. ORNL annual reports have reported that specifically 20 – 25% of energy is lost due to uncontrolled entropy generated in "premixed" combustion prevalent in current conventional transportation engines which in turn contributes to the inefficiencies in these engines. They proposed an alternative to address the problem that would significantly reduce entropy generation and subsequently investigated an UMC based process called Staged Combustion with Oxygen Transfer (SCOT) on a theoretical basis. They found that the key benefit of SCOT lies in enabling sustained operation under near isothermal conditions. They however did not investigate the practical feasibility of their idea.

UMC can be carried out in fluidized bed and packed bed reactors, the former being referred to as Chemical Looping Combustion (CLC) [7]. In the fluidized bed reactor system, the OSRM is circulated between a riser (air reactor) and regeneration unit (fuel reactor). In the air reactor, a hot O_2 depleted stream is produced by oxidation of a suitable OSRM while in the fuel reactor, which is normally a bubbling fluidized bed, the same OSRM particles are reduced with fuel gas producing CO_2 with steam as shown in Fig. 2.2.

The focus of CLC has been till date on inherent CO_2 separation from flue gas. Researchers [8 – 12] have reviewed recent advances on CLC and mentioned that it holds great promise as a combustion process and is a viable alternative to "premixed combustion" for minimizing emission of greenhouse gases and also producing hot air streams to be used for power generation purposes. But this technology has a disadvantage of carryover of solid fines in the gas streams.
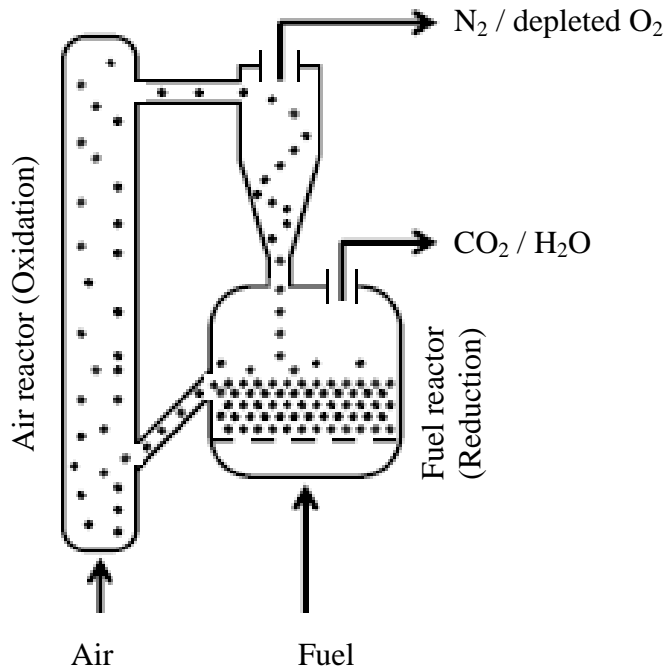
Fig. 2.2 Schematic of fluidized bed UMC reactor system [7, 13]

In an attempt to move away from above mentioned disadvantage of using fluidization in UMC, Noorman, et. al. [13] proposed a new dynamically operated packed bed reactor concept, in which, compared to the interconnected fluidized bed systems, the difficult separation of gas and circulating particles can be intrinsically avoided and the OSRM can be utilized over its entire range of oxidation states. The disadvantage of this system however, is the requirement of a high temperature, high flow gas switching system.

They investigated the feasibility of using packed bed reactor technology for UMC with an objective to generate high temperature product streams at the outlet. An analytical approach was used to derive an expression for the maximum temperature in the oxidation cycle using an energy balance for a system with fixed amount of Cu based OSRM and neglecting heat loss from the reactor wall. The analysis revealed that two fronts namely a reaction front and a heat front propagate through the reactor as shown in Fig. 2.3. At the reaction front, the reactant fed reacts with a known amount of OSRM causing the bed temperature to increase due to reaction exothermicity. At the heat front, the energy stored in the solid material after reaction, as a result of its heat capacity, is transferred to the gas

phase resulting in lowering of bed temperature. The front velocities have been shown to be the functions of properties of reactive gas and OSRM, inlet velocity and reactive gas composition.
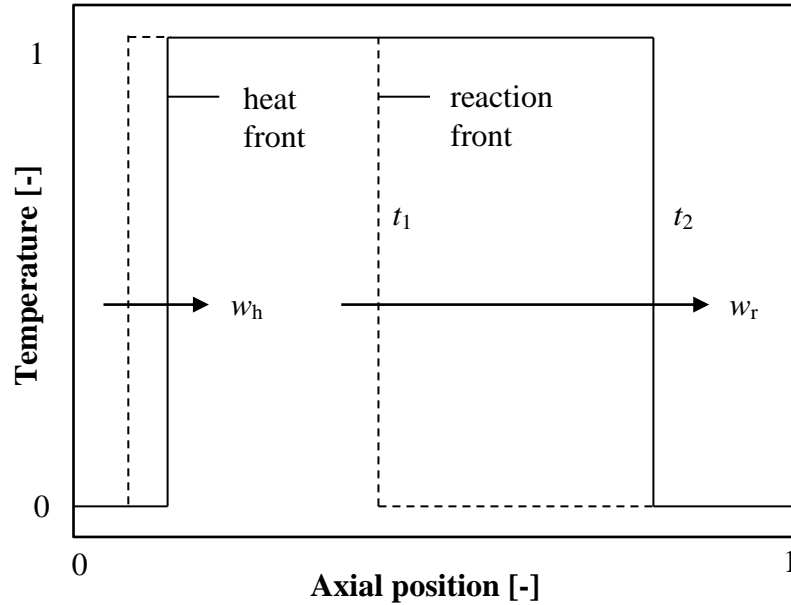
Fig. 2.3 Schematic representation of temperature profiles and heat front in a packed bed UMC reactor (Reproduced from Noorman et. al [13])

Noorman et. al. [14, 15], conducted experiments, wherein 12.5 wt% CuO on alumina particles with an average particle diameter of 1.1 mm was used as the OSRM. The reactor system performance was investigated using zero air and methane as reactive gases in a temperature range of 748.15 – 1273.15 K. The reduction cycle time was decided based on the breakthrough of methane which indicated the complete reduction of the OSRM bed and the oxidation cycle was terminated when the hot air outlet temperature started dropping from the maximum temperature reached. In the first study [14], the operation of packed bed UMC reactor was demonstrated and the reaction and heat front velocities estimated from measurement showed good agreement with those predicted by analytical expressions developed earlier in their studies [13]. In addition, temperature rise during the reduction cycle was found to be much lower (50 K) than that in the oxidation cycle (200 K) due to lower concentrations of methane as well as the lower enthalpy of

reduction reaction. In the other study [15], the effects of initial bed temperatures and steam addition on the performance of packed bed based UMC operation was evaluated. The results indicated that increase in initial bed temperature during the oxidation cycle, did not have significant effect on the observed reaction rate and conversion. In the reduction cycle, at temperatures below 773.15 K, reduction of OSRM was observed to be incomplete, while above 923.15 K, significant side reactions and coke formation was observed. This coke formation can be completely eliminated by addition of steam which would help in improving the performance of the UMC reactor, but would introduce an economic penalty at a large scale. The emphasis of all these investigations however was on obtaining a very high temperature gas stream exiting the reactor for considerably longer duration so as to axially drive the turbines in power plants and simultaneously obtaining pure CO_2 for sequestration purposes. It must also be noted that in all these studies, the reactor was insulated and radial heat transfer was completely avoided.

2.3   Oxygen Storage and Release Material (OSRM)

A suitable choice of OSRM is vital to successful implementation of UMC on a large scale. In this section, literature related to investigations on feasible OSRMs' for UMC applications has been reviewed and reported.

Several researchers over the years have been investigating OSRMs' mainly in relation to fluidized bed based UMC systems [16 – 22]. Hossain and Lasa [10] have presented a detailed review discussing advantages and disadvantages of potential OSRMs'. A summary of their findings is presented herewith.

They have suggested that a suitable OSRM should have the following characteristics:

a. Good oxygen carrying capacity
b. Ability to completely combust a fuel
c. Stability under repeated reduction/oxidation cycles more so at higher temperatures
d. Resistance to agglomeration/sintering at high temperatures

e. Environmentally benign

f. Economically feasible

In addition, physical properties like density, active surface area, pore volume and particle size are also important parameters to be considered. The density and particle size may affect the overall reaction rate, given their influence on mass and heat transfer inside the particles.

They have reported that the transition metal oxides such as nickel (Ni), copper (Cu), cobalt (Co), iron (Fe) and manganese (Mn) are suitable candidates based on their favorable reductive/oxidative thermodynamics. Oxides of Mn, Co and Cu have greater tendency to react with methane (CH_4) in the temperature range of 873.15 – 1473.15 K as compared to those of Fe and Ni. However, Mn and Co based oxides decompose further to different respective oxidation states at relatively lower temperatures, limiting their choice as suitable candidates. Cu also has tendency to decompose from CuO to copper (I) oxide (Cu_2O), but only at a higher temperature of 1303.15 K, and more so when oxygen concentrations are lower. In terms of the ability to completely convert methane during reduction, Mn, Cu, Fe and Ni based OSRMs' are found to be favorable. Cadmium (Cd), zinc (Zn) and cerium (Ce) are unsuitable due to their relatively lower melting points (< 873.15 K). Cu also has a relatively lower melting point of 1358.15 K, but can be used for applications upto 1173.15 K.

For the reasons mentioned above, Hossain and Lasa [10] have reported that majority of the earlier works focused on Fe, Cu and Ni based OSRMs'. Due to abundant availability and low cost, both Cu and Fe based OSRMs' have attracted significant number of research studies. Ni has received extra attention given its superior reactivity, thermal stability and negligible volatility, all these favoring high temperature operation. The reactions involving these OSRMs' along with respective enthalpy of reaction at standard conditions are presented in Table 2.1 below. It is interesting to note that both oxidation and reduction reactions involving Cu are exothermic, while in case of Fe and Ni, only oxidation reactions are exothermic.

Table 2.1

Cu, Fe and Ni based OSRM reactions and respective standard enthalpy of reaction*

Reactions	ΔH^o_{rxn} (kJ/mol)
CuO/Cu	
$CH_4 + 4CuO \longleftrightarrow 4Cu + CO_2 + 2H_2O$	−178.0
$H_2 + CuO \longleftrightarrow Cu + H_2O$	−85.8
$CO + CuO \longleftrightarrow Cu + CO$	−126.9
$O_2 + 2Cu \longleftrightarrow 2CuO$	− 312.1
Fe$_2$O$_3$/Fe$_3$O$_4$	
$CH_4 + 12Fe_2O_3 \longleftrightarrow 8Fe_3O_4 + CO_2 + 2H_2O$	141.6
$H_2 + 3Fe_2O_3 \longleftrightarrow 2Fe_3O_4 + H_2O$	−5.8
$CO + 3Fe_2O_3 \longleftrightarrow 2Fe_3O_4 + CO_2$	−47.0
$O_2 + 4Fe_3O_4 \longleftrightarrow 6Fe_2O_3$	−471.9
NiO/Ni	
$CH_4 + 4NiO \longleftrightarrow 4Ni + CO_2 + 2H_2O$	156.5
$H_2 + NiO \longleftrightarrow Ni + H_2O$	−2.1
$CO + NiO \longleftrightarrow Ni + CO_2$	−43.3
$O_2 + 2Ni \longleftrightarrow 2NiO$	−479.4

 * At 298.15 K and 0.1 MPa (Reproduced from Ref. [19])

To increase reactivity and durability, the above OSRMs' can be prepared by depositing the active metal oxide(s) on an inert support such as silicon oxide (SiO_2), titanium oxide (TiO_2), zirconium oxide (ZrO_2), alumina (Al_2O_3), yttria stabilized zirconia (YSZ) and bentonite. Ni/NiO supported on alumina has limitations of particle agglomeration due to formation of $NiAl_2O_4$ (nickel aluminate) at temperatures above 1273.15 K. Fe supported on alumina increases the reduction rates substantially, but the reaction between Fe and Al_2O_3 may result in loss of particle reactivity.

Reviews presented by Fang et. al. [11] and Adanez et. al. [12] have also discussed prospective OSRMs' and proposed Fe, Cu, Ni and Mn oxides as potential candidates as was suggested by Hossain and Lasa [10]. They have mentioned that development of

oxygen carriers with excellent stability and reactivity will remain a challenge. Adanez, et. al. and de Diego et. al. [12, 17] reported that the methods used in the preparation of the OSRMs' strongly affect the properties of material. Among several preparation methods like freeze granulation, spray drying, co-precipitation, sol-gel, and impregnation methods, OSRMs' prepared by impregnation methods exhibited excellent chemical stability without substantial decay of mechanical strength in multi-cycle testing.

Noorman et. al. [13] have also discussed Fe, Cu and Ni based OSRMs' for packed bed UMC operation. Their investigations revealed that the selection of Ni/NiO results in the undesired phenomena of coke formation during reduction of NiO with methane. This can be suppressed using steam, but addition of steam increases the mass flow through the reactor resulting in substantial pressure drop across the packed bed and increases the cost associated with handling of steam. In case of iron oxide, multiple reduction states will be encountered and selectivity towards CO_2 deteriorates during reduction of Fe_2O_3. For Cu based OSRMs', they expressed concerns about its low melting point, but mentioned that in this case both oxidation and reduction reactions involved are exothermic which eliminates the need for supplying energy to sustain these reactions. This in addition to its relatively lower cost provides a reason for recommending this as a potential OSRM for UMC based studies. They also mentioned that constant and reliable particle behavior over a large number of reduction/oxidation cycles along with chemical, mechanical and thermal stability of the OSRM are of great importance in a packed bed UMC reactor, as replacement of the particles can be costly.

2.4   Kinetic study of non-catalytic gas-solid reactions

The enthalpy of reaction is a function of reaction rate and the design of any reactor system including that for UMC necessitates a knowhow of this rate. In this regard, the estimation of concentration dependency (i.e. reaction orders) and kinetic parameters i.e. pre-exponential factor and activation energy was included in the present study for the representative OSRM reactions involved. A Pulsed Micro-reactor (PMR) was used for this purpose and in this regard related literature review is presented in this section.

Non-catalytic gas-solid reactions like coal gasification or pyrolysis, reduction of ores, oxidation and reduction of metal/metal oxides, coking and regeneration of deactivated catalyst are common in process industries. For such reactions, developing a kinetic rate law to be used in reactor design is challenging as the reaction mechanism involves external and internal pore diffusion along with the surface reaction step. An effective reaction rate constant k''_e can be used to account for these three resistances and the rate equation for such reactions can be expressed using a power law model having form

$$- r''_g = k''_e \, c_g^n \, c_s^m \qquad\qquad\qquad (2.1)$$

where *m* and *n* are reaction orders with respect to solid and gaseous reactant respectively.

Generating accurate and reliable data to estimate k''_e is equally important. Traditionally, Thermo Gravimetric Analysis (TGA) method [23 − 28] has been used to estimate k''_e. This method incorporates a differential reactor for determining kinetic parameters of heterogeneous gas-solid reactions based on suitable changes in solid weight. Pulse methods for kinetic investigations have also found interest for this purpose. These are based on the principle wherein a reactant pulse of defined concentration is allowed to pass over a bed of solids until no change in the shape of the pulse response is observed. A special pulse based technique known as Temporal Analysis of Products (TAP) proposed by Gleaves 1988 [29] has also been used for studying kinetic mechanisms. While this technique is extremely exciting and promising in understanding kinetic phenomena at a microscopic level, its application to a certain extent is restricted by affordability and mathematical treatment is reasonably complex. Till date the emphasis of the use of TAP has been on characterizing the reaction kinetics of chemical conversion over heterogeneous catalysts attempting to bridge the gap between surface science experiments and applied catalysis [30, 31].

As an alternative, a Pulsed Micro-reactor (PMR) method proposed by Attar [32] offers potential for studying kinetics of gas-solid reactions. In this method, a fixed amount of solid placed inside a tubular reactor is swept by an inert stream of carrier gas which flows

into a Gas Chromatograph (GC). Several pulses of reactant gas are subsequently injected into the carrier gas stream and allowed to react with the solid until it is completely saturated. Near plug flow conditions are assumed to prevail at all times inside the reactor. The product stream from each injected pulse along with unreacted feed gas after saturation can be analyzed using the GC. This reactor system integrated with a GC offers a relatively easy method to determine k''_e with several advantages including determination of isothermal rates of reaction and activation energies of highly exothermic or endothermic reactions. This discontinuous character of operation, allowing for direct integration between the reactor and GC as well as absence of manual handling of samples leads to accurate measurement and ease of operation [33].

Zamostny, et. al. [33] have used such a system for studying gas-phase reactions and reported that reactor dimensions normally do not exceed 10 mm in diameter. Such narrow dimensions however do not allow for easy measurement of temperature inside the reactor. In their work, a series of measurements of reactor temperature in relation to the outer wall temperature and gas flowrate was made in the absence of solid catalyst. The reactor temperature during their main test runs with solid was indirectly determined from this measured wall temperature and flowrate.

This reactor system has been used over the years to estimate kinetic parameters, with major emphasis on catalytic gas-solid reactions like thermal cracking of mixture of hydrocarbons, xylene isomerization, cyclohexane dehydrogenation and hydrogenation of benzene [33 – 36]. It has also been used to determine conversion, selectivity and yield for a gamut of such reactions, with emphasis on understanding reaction mechanisms involved, catalyst activity and stability [37 – 43]. Its application however has been mostly limited to cases where the kinetics is linear. Sica et. al. [36] have presented the application of this reactor to investigate non-linear kinetics associated with the catalytic hydrogenation of benzene.

Attar [32] have demonstrated the use of this reactor for determination of rate constant of non-catalytic gas-solid reactions, wherein he estimated the rate of reaction of hydrogen

sulfide (H_2S) gas with an alkaline mineral like calcite at 843.15 K and 0.97 bar. GC data obtained was used to calculate the fraction of unreacted solid present in the reactor after every pulse and the amount of reactive gas required to completely convert the solid. Adopting an uniform reaction methodology based model, the rate constant and hence the reaction rate was estimated. Their results showed that for an assumed reaction order of 2/3 with respect to the solid reactant, an excellent agreement of reaction rate was obtained between the model and experimental data. However, when the experiment was conducted at 973.15 K, the results showed deviation from values obtained using the model. This was attributed to sintering effect prevalent at higher temperatures. In addition, Attar has mentioned the pulse size to be critical in such measurements. Pulses that are too small may result in problems associated with the detection of the products of the reaction and pulses that are too large may cause too rapid a conversion of the solid resulting in lack of sufficient data points for analysis. It must however be noted that the investigations of Attar were also restricted to 1st order reactions with respect to the gaseous reactant.

Till date, this reactor system has gained little attention with regard to estimating kinetic parameters of non-catalytic gas-solid reactions due to a possible challenge in interpretation of experimental data, more so when non-linear kinetics is involved. This technique has also not been used to investigate the kinetics of Cu oxidation and CuO reduction reactions, which are also non-catalytic gas-solid reactions.

Garcia – Labiano et. al. [23] investigated these parameters for 10 wt% CuO on alumina having an average particle size of 0.2 mm using a TGA balance coupled with GC analysis. They have presented results on reduction kinetics using methane (CH_4), hydrogen (H_2) and carbon monoxide (CO) and oxidation with air in the temperature range of 773.15 to 1073.15 K.   However, 30% steam was injected along with 70% CH_4 during reduction to avoid coke formation allowing for kinetic data to be obtained in the temperature range in which the experiments were conducted. The use of steam can have process engineering implications in UMC reactor system**s** and the same has not investigated till date. Adopting a shrinking core model, they determined kinetic

parameters considering surface reaction as the rate limiting step. The results of kinetic parameters obtained are presented in Table 2.2. While the concentration dependency with regard to solid has not been reported directly, the results seem to indicate that the rates are independent of solid concentration i.e. $m = 0$.

Table 2.2

Kinetic parameters for oxidation of Cu and reduction of CuO (using CH_4, H_2 and CO)*

	CH_4	H_2	CO	O_2
$k_o^{''}$ ($mol^{1-n} m^{3n-2} s^{-1}$)	4.5 x 10^{-4}	1.0 x 10^{-4}	5.9 x 10^{-6}	4.7 x 10^{-6}
E (kJ mol^{-1})	60 ± 3	33 ± 1	14 ± 1	15 ± 2
n	0.4	0.6	0.8	1.0

* Ref. Garcia – Labiano, et. al. [23]

2.5 Modeling of Packed Bed Reactor (PBR) systems

Modeling of UMC reactors can provide detailed information on the prevailing concentration and temperature profiles in the reactor and an in-depth understanding of system behavior. This will facilitate more reliable predictions of reactor performance and in turn help design systems with optimum operating efficiency at an industrial scale level. As discussed in section 2.2, UMC can be carried out in fluidized or packed bed reactors. With the focus of the current study being on using a PBR system for UMC, this section summarizes important developments related to PBR modeling in this context.

PBRs′ are amongst the most commonly used reactors in process industries especially when gas-solid and liquid-solid catalytic and non-catalytic reactions are involved. When the fluid containing the reactants flows past the solid, a variety of physical and chemical phenomena like intra-particle and inter-particle concentration and temperature gradients, heat and mass dispersion, wall heat transfer and chemical reaction occur in the reactor. General mathematical models of a PBR incorporate these transport and reaction phenomena that occur in multi-phase systems. Due to enormous complexity of these phenomena, an exact mathematical description of these reactors becomes extremely

challenging. Thus for predicting PBR system behavior, one has to rely on simplified models capturing the most crucial and salient features [44 – 47].

PBRs′ have been modeled using cell models or continuum models [47]. In cell models, modeling equations are framed by considering the solid particle and surrounding fluid as single cell and accounting for the interaction between different such cells. These models however have not gained much attention as they are not supported by enough engineering data and PBR modeling continues to rely on continuum models which are based on the conservation laws of mass, momentum and energy leading to differential and/or algebraic equations. These models have been grouped into two broad categories: pseudo-homogeneous and heterogeneous. In the pseudo-homogeneous model, it is assumed that the solid surface is exposed to bulk fluid conditions ignoring the heat and mass transfer resistances between the fluid and solid. It relies on the use of global kinetics. These are mostly applied to systems where the temperature and concentration of the fluid phase is approximately equal to the temperature and concentration at the solid surface. A heterogeneous model, on the other hand, uses intrinsic kinetics and accounts for intra-phase resistances. Based on the complexities involved, these models have been further classified as depicted in Fig. 2.4 by Lordaninis [47]. A flow chart has been suggested by Hugo Jakobsen [48] as shown in Fig. 2.5, which prima facie can be used to select a model based on the system under consideration.

The general governing equations for each of the models shown in Fig. 2.4 are available in literature [44, 47]. The equations consist of the dispersion fluxes represented in the form of Fick's and Fourier's laws [49] and effective parameters which include:

a. Radial mass dispersion coefficient
b. Axial mass dispersion coefficient
c. Effective radial thermal conductivity
d. Effective axial thermal conductivity
e. Wall heat transfer coefficient
f. Overall heat transfer coefficient
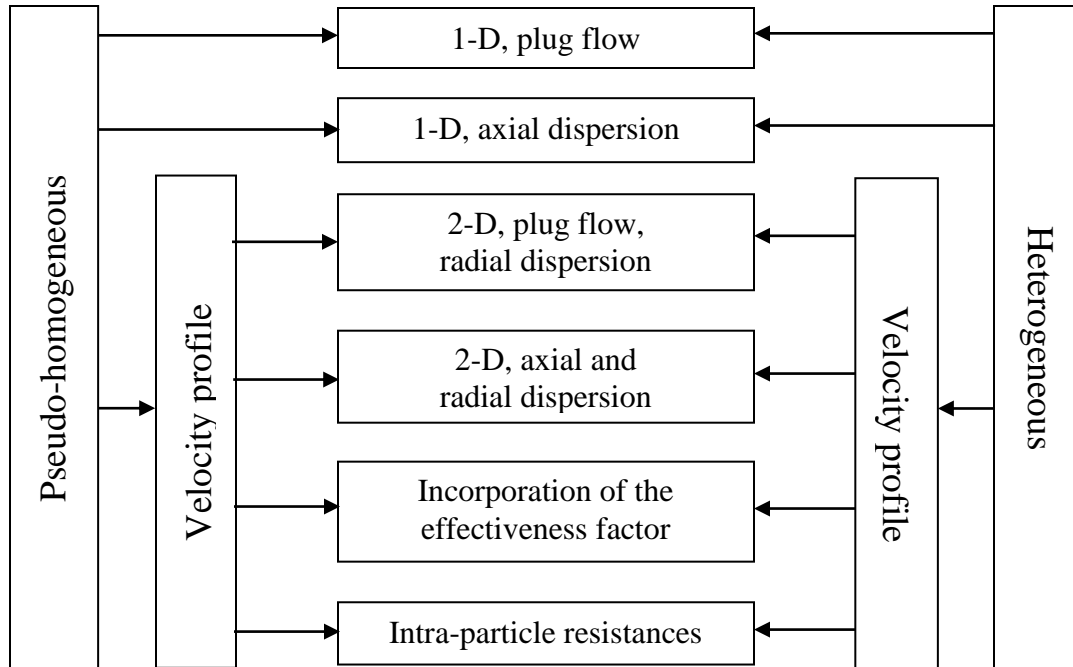
Fig. 2.4 Models for packed bed reactors (Reproduced from ref. [47])

Accurate estimation of these parameters is of importance as it gives more logical and close to realistic prediction of concentration and temperature profiles in the reactor. A review by Kulkarni and Doraiswamy [50] provides detailed information about correlations available for estimation of these parameters. Other parameters like reactor length and the superficial gas velocity per unit reaction area is a trade-off between the gas–solid contact time requirements and the maximum allowable pressure drop along the reactor.

The complexity of processes taking place in PBRs' not only leads to difficulties and uncertainties with their mathematical description, but also to problems related to numerical handling of the resulting equations. This in turn significantly increases the demand of computational requirements. The numerical treatment of these modeling equations has been studied at various levels and is mainly based on finite difference, finite element or finite volume methods [47, 51 – 55].
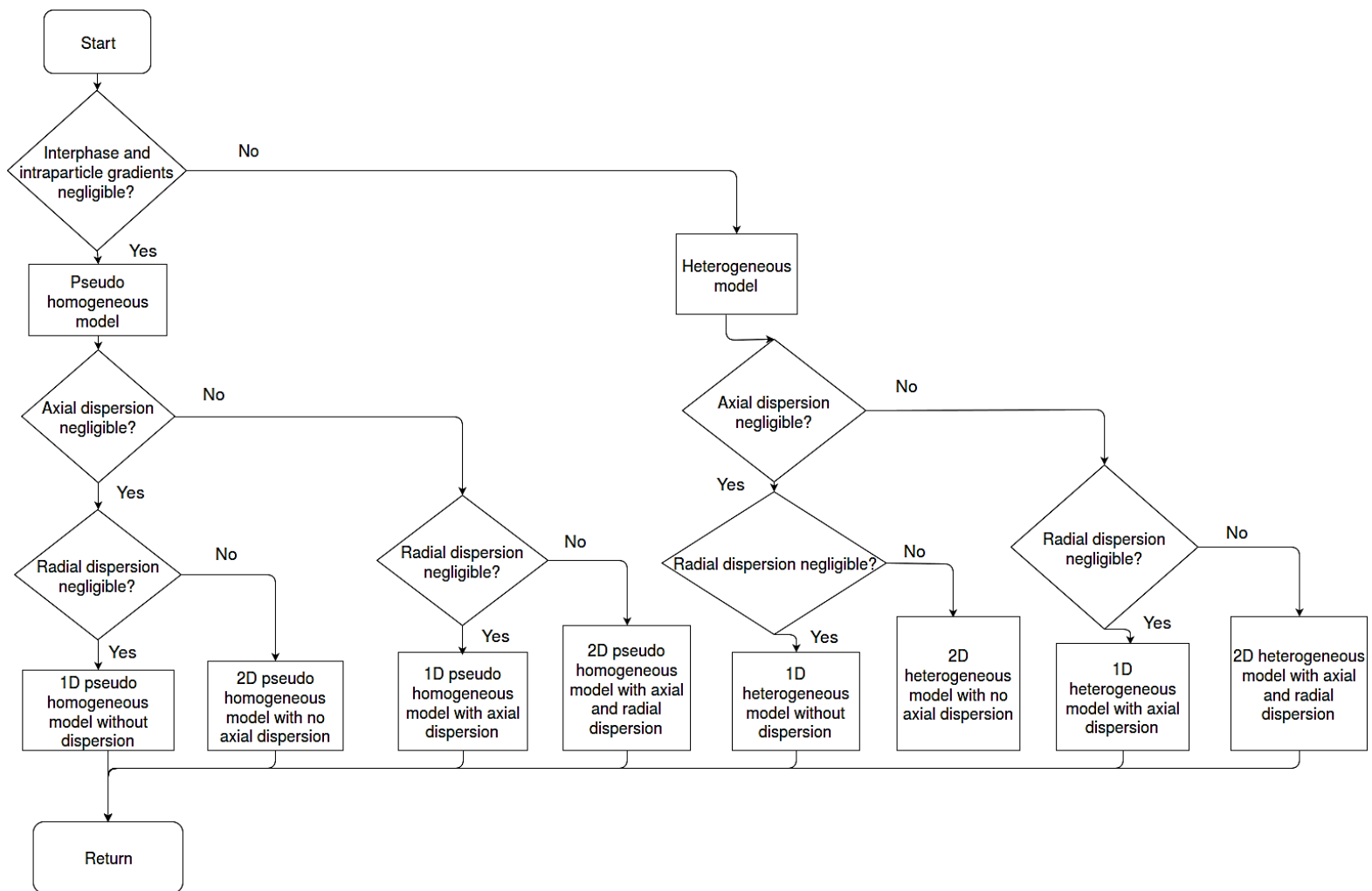
Fig. 2.5 Flowchart for selecting an appropriate PBR model (Reproduced from Ref. [48])

Among the broadly classified models, heterogeneous models incorporate a large number of physico-chemical parameters. These may however be unyielding to analysis or computation and hence impractical to study unless absolutely essential. These models are usually preferred only when the concentration and temperature variations within the particle are significant and affect the overall reactor performance. This significance can be accounted for by using different criteria like the one based on Thiele's modulus and proposed by Mears′ [44, 56]. In certain regions of the parameter space, in which the rates of some of the transport or reaction processes are much slower or faster compared to others, it is possible to simplify heterogeneous models to a pseudo-homogeneous level or have models with lower dimensional state spaces and a smaller number of effective parameters [57]. Generally, it is advised to go for heterogeneous models only if the assumptions made in pseudo-homogeneous models fail.

Pseudo-homogeneous models have been studied in detail and widely used by several researchers [44, 47 − 48, 58 − 62]. Srinivasan et. al. [63 − 65] have presented studies related to investigating a 1-D model for a PBR and validating the same using nitric oxide − carbon monoxide (NO − CO) kinetics. According to these studies, modeling in one dimension is sufficient if the length to diameter ratio of the reactor is high. In this investigation, mass and heat Biot numbers at the wall and pellet for the considered parameters were calculated and found to be less than 10 and 0.1 respectively, which confirmed that diffusion and temperature gradients in the radial direction can be neglected. Their results indicate that a careful consideration of source terms involved in species and energy equations are essential in modeling a packed bed reactor accurately. Parametric studies concluded that conversion characteristics are dependent on effective diffusivity and thermal conductivity.

While modeling UMC or recuperative-regeneration based PBRs′, the additional challenge of operating the reactor in -mode needs to be taken care of. Noorman et. al. [13] have developed a transient 1-D pseudo-homogeneous model to understand the dynamic operation of a packed bed UMC. The focus was however on predicting the duration for which the maximum temperature of the gaseous products can be obtained at the reactor

outlet with an aim to make these hot gas streams available to run a turbine on a sustainable basis. They assumed the absence of gradients in radial direction, heat loss through the reactor wall and that plug flow conditions were prevalent in the axial direction. The proposed governing equations used in their work are as reported below.

Gas phase component mass balance

$$\varepsilon_g \rho_g \frac{\partial w_g}{\partial t} = -\rho_g v_g \frac{\partial w_g}{\partial z} + \rho_g D_{ez} \left[\frac{\partial^2 w_g}{\partial z^2} \right] + r_g \varepsilon_g M_g \qquad (2.2)$$

Solid phase component mass balance

$$(1 - \varepsilon_g) \rho_s w_{act} \frac{\partial w_s}{\partial t} = r_s \varepsilon_g M_s \qquad (2.3)$$

Energy balance

$$(\varepsilon_g \rho_g C_{pg} + (1 - \varepsilon_g) \rho_s C_{ps}) \frac{\partial T_b}{\partial t} = -\rho_g v_g C_{pg} \frac{\partial T_b}{\partial z} - \lambda_{ez} \left[\frac{\partial^2 T_b}{\partial z^2} \right] + \varepsilon_g (\Delta H_{rx})(r_g) \qquad (2.4)$$

Reaction rate

$$-r_g = k_e c_g^n c_s^m \qquad (2.5)$$

where

$$k_e = k_c a_c \eta k_o^{''} S_a \rho_b / (k_c a_c + \eta k_o^{''} S_a \rho_b) \qquad (2.6)$$

In equations (2.1) to (2.6), w_g, w_s, T_b, r_g, c_g, c_s, k_e, η, k_c and $k_o^{''}$ denote mass fraction of gaseous component, mass fraction of solid component, temperature in the packed bed, rate of reaction, concentration of gaseous reactant, concentration of solid reactant,

effective reaction rate constant, internal effectiveness factor, external mass transfer coefficient and pre-exponential factor respectively.

In this model, 21 mol % O_2 (air) and 4 mol% CH_4 were used as reactive gases during oxidation and reduction respectively. The changeover from oxidation to reduction was incorporated when the air outlet temperature dropped below 1200 K and the reduction cycle was stopped when methane composition at the outlet exceeded 5 % by weight. The reaction kinetic parameters used in this study were taken from Garcia − Labiano et. al. [23]. Ergun's equation was used to calculate pressure drop and the usual Dankwart's boundary conditions were applied. The model results were validated with data obtained from their experimental investigation [14]. This agreement suggested that the pseudo-homogeneous model is suitable for UMC based systems.

Fernandez et. al. [66] have also developed and validated a transient 1-D pseudo-homogeneous model to describe the Cu oxidation cycle of a Ca/Cu looping process for hydrogen production in an adiabatic packed bed reactor on a large scale. An ideal plug flow pattern without axial dispersion was assumed. Apart from this, they adopted assumptions of absence of radial temperature or concentration gradients, negligible intra-particle concentrations and temperature gradients, ideal gas behavior, constant void bed fraction and uniform particle size. The mass and energy balance equations developed based on these assumptions were same as those presented earlier in this section excluding the dispersion and conductivity terms. Kinetic data reported by Garcia − Labiano et. al. [23] was used. In the reaction terms of these equations, an effectiveness factor (η) was incorporated to account for internal diffusion limitations normally associated with larger particles (> 0.001 m) and higher operating temperatures (> 973.15 K). A particle size of 0.01 m was chosen for this study and operating temperatures were in the range of 923.15 − 1100.15 K. The model was implemented and solved using MATLAB based on a backward finite difference numerical method. The results showed that Cu oxidation is favored at high pressure and fast reaction rates in this case can be achieved even with low oxygen concentrations (3 − 4 mol %) in the feed. It was also observed that at high flowrates and low concentration levels of oxygen, the heat front advanced much faster

than the reaction front, resulting in cooling of the bed and consequently additional energy was required to initiate the subsequent reduction cycle. However maximum temperature at the outlet of the reactor could be achieved for a specific time period during oxidation. A parametric study showed that inlet gas temperature and not the initial solid temperature affects the maximum temperature. In addition Cu oxidation was favoured at high pressure and having a reasonable proportion of Cu in the solid bed is essential for achieving high energy efficiency. This study also confirmed that pseudo-homogeneous model is suitable to describe PBR performance for UMC involving Cu when used at a larger scale.

The characteristics of the rate of reduction and oxidation that OSRMs' undergo in packed bed UMC process from a theoretical point of view have been studied by developing combined reactor and particle model by Noorman et. al. [67 – 68]. A very efficient finite difference numerical technique with higher order temporal and spatial discretization with local grid and time step adaptation was used to solve respective modeling equations. With the help of these results, an improved understanding of the effect of mass and heat transfer processes on the rate at which OSRMs' are reduced and oxidized have been obtained. With these models, more reliable predictions of the axial concentration and temperature profiles which are necessary to arrive at a proper design and a quantitative assessment of the suitability of packed bed for UMC were obtained. Simulations were performed using Cu based OSRM. In this simulation, they found that the effect of external heat and mass transfer and internal heat transfer limitations was negligible and that there were no temperature gradients within the particle in the oxidation cycle. It was also concluded that internal diffusion limitation in the particle interior needs to be considered when higher conversion of solid material is obtained, which occurs at relatively higher temperatures. In the reduction cycle, where efficient use of fuel and high CO_2 capture efficiency are aimed for, it was concluded that the effect of intra-particle mass transfer limitations need to be included in the model description, specifically when the bulk concentration of the reactive gas is low and operating temperatures are higher. Thus if the operating temperature of the PBR is not relatively high (> 973 K) and conversion and concentrations are maintained above a particular limit, then variations within the particle can be neglected and pseudo-homogeneous model can be used.

With the model description available, a good foundation is possible for a process design that should lead to a detailed assessment of the technical and economical feasibility of cyclically operating packed bed UMC reactor. But all of the above studies however have not taken radial variations of temperature and concentration within the reactor into consideration and limited their investigations only for cases where there is no heat transfer from the wall.

2.6   Summary and Gaps

Unmixed Combustion (UMC) has been proposed as an alternative to fire or premixed combustion [1 – 3]. UMC based adiabatic fluidized bed or packed bed reactor technologies till date have focused mainly on CO_2 capture and utilizing the enthalpy in exit hot streams for power generation. The possibility of utilizing this energy for heat transfer applications by radially transferring the same to a coolant primarily by conduction and convection under sustained conditions with minimal temperature variations (i.e. near isothermal conditions) in the OSRM bed has not been investigated till date. Development of such a reactor system will pose a challenge.

The review related to OSRMs' for UMC based applications, their development and usage suggests that Ni, Fe and Cu supported on inert materials like alumina are potential OSRMs' [10 – 12]. As compared to Ni and Fe, Cu based OSRM supported on alumina prepared by impregnation method can be an inexpensive and reasonable choice if the UMC application does not involve very high temperatures and relatively lower oxygen concentrations are avoided. Exothermic oxidation and reduction reactions involving Cu makes it an even better choice when UMC is to be used for any process applications [10, 13, 22].

In order to estimate the kinetic parameters of non-catalytic gas-solid reactions like the one involved in UMC, different techniques like TGA and TAP are commonly used. A relatively simple and inexpensive Pulsed Micro-reactor (PMR) integrated with a GC can

be a non-competing and viable alternative to these techniques to generate kinetic data for reactions systems having linear or non-linear kinetics [32]. However a suitable methodology to interpret this experimental data for non-catalytic gas-solid reaction needs to be developed.

Packed bed reactors (PBRs') for UMC are generally modeled using pseudo-homogeneous and heterogeneous continuum models. Simple, though robust pseudo-homogeneous models with effective properties are mostly preferred over more complex heterogeneous models, unless the assumptions made while developing the former fail [63 − 65]. A dynamically operating UMC based PBR involving cyclic operation has been successfully modeled using a 1-D pseudo-homogeneous approach by several researchers [13, 66 − 68]. But the temperature variation in the radial direction is not included in these models which have been restricted to investigate performance of an adiabatic PBR dominated by axial gradients. 2-D PBR models with radial heat transfer need to be developed and investigated to understand and predict the performance of UMC for heat transfer applications.

Chapter 3
Aim and Scope of the Work

Based on the literature survey presented in Chapter 2, it is clear that Unmixed Combustion (UMC) offers an alternative to "premixed" combustion and that the enthalpy of the oxidation and reduction reactions involved, if exothermic, can be utilized for heat transfer applications. However sustained cyclic UMC operation under dynamic conditions incorporating radial heat transfer by conduction and convection to a coolant has not been demonstrated at "proof of concept" level till date. The effect of important bed parameters like reactive gas and coolant inlet flowrates and gas inlet temperature on the total heat transfer has also not been investigated. There is also no model reported in literature incorporating transport mechanisms at reactor level to predict performance of such a complex and integrated system. In view of the above gaps, the primary objective of this work was to investigate the practical and theoretical possibility of effectively using a dynamically operated Unmixed Combustion (UMC) reactor for heat transfer applications. It was proposed to conduct the research work with following sub-objectives:

1. To develop a conceptual design and establish a "proof of concept" bench scale facility for studies on UMC and its application for heat transfer
2. To carry out experimental investigations to understand the effect of operating parameters on heat transfer to a coolant with the UMC reactor as a heat source
3. To develop, simulate and validate a mathematical reactor model to predict performance and obtain an insight into behaviour of an integrated UMC – heat transfer system

As an offshoot of the above work, it was decided to investigate the efficacy of using a Pulsed micro-reactor as an alternative to TGA and TAP systems for estimating global kinetic parameters of the non-catalytic gas-solid reactions involved in UMC. The kinetic data obtained was subsequently used in the reactor model to predict the energy generation in the OSRM bed, fraction of which was transferred to the coolant by conduction and convection.

A 'proof-of-concept' test rig consisting of an annular packed bed reactor was designed, fabricated and commissioned to demonstrate the potential of UMC for heating coolant air. Careful experiments were conducted using a copper (Cu) based Oxygen Storage and Release Material (OSRM) over a wide range of relevant variables. The approximate ranges of the variables covered in the test runs are given below.

OSRM loading (kg)	1.25
Reactive gas inlet temperature (K)	873.15 – 923.15
Initial bed temperature (K)	873.15
Zero air flowrate (LPM)	5 – 20
CH_4 flowrate (LPM)	2 – 6 (corresponding to 10 – 30 mol %)
N_2 flowrate (LPM)	14 – 18
Coolant air flowrate (LPM)	100 – 175

For prescribed values of inlet temperatures and flowrates of reactive gases and coolant air flowrate, the total heat transfer to coolant from the OSRM bed was estimated. In each run, the focus was on achieving sustained heat transfer under near isothermal conditions (i.e. minimal temperature variations) in the bed.

Kinetic parameters were determined using a Pulsed Micro-reactor (PMR) technique. A lab scale facility was designed, fabricated and commissioned for this purpose. Test runs for oxidation and reduction were conducted to determine respective reaction order and reaction rate constants at a particular temperature. The approximate ranges of the variables covered in the test runs are

Oxidation

OSRM loading (mg)	100
O_2 concentration in zero air (mol%)	21
Pulse size (cc)	0.5
Temperatures (K)	673.15 – 873.15
Flowrate (SCCM)	35

Reduction

OSRM loading (mg)	100 and 400
CH_4 concentration (mol%)	99.5
Pulse size (cc)	0.1
Temperatures (K)	873.15 – 973.15
Flowrate (SCCM)	35

A simple uniform reaction methodology was adopted to interpret data from the PMR system and estimate reaction orders, pre-exponential factor and activation energy for both reactions. The results obtained compared with those in literature obtained using a TGA.

A 2-D pseudo-homogeneous packed bed reactor model was developed incorporating the phenomena of heat transfer to coolant. For prescribed conditions of OSRM loading, inlet temperatures and flowrates of reactive gases and coolant flowrate, the model predicts the concentration and temperature profiles in the bed, velocity and temperature profiles of coolant and heat transfer rates at the surface. In the context of the present study, the model was validated using experimental data obtained for bed temperature profiles and the total heat transfer to coolant.

Chapter 4

Experimental Set-up and Instrumentation

Two different purpose built test-rigs were designed and fabricated to investigate the potential of Unmixed Combustion (UMC) for heat transfer applications and study OSRM reaction kinetics respectively. The details of these test rigs are presented in sections 4.1 and 4.2.

4.1   UMC based heat transfer test rig

4.1.1   General layout

The test rig comprised of a feed gas and reactor section, the general layouts of which are shown in Fig. 4.1 and 4.2 respectively. Photographs of the assembled test rigs including reactor, furnace assembly and measuring instruments are shown in Fig. 4.3.

Zero air and a mixture of methane (CH_4) and nitrogen (N_2) were used as reactive gases in the test runs for oxidation and reduction respectively. As depicted in Fig. 4.1, these feed gases were supplied to the reactor section via respective rotameters (R1, R2 and R3), thermal mass flow indicators (MFI: 01 - 03) and solenoid valve (SOL: 01 - 02). The valves were provided with a timer which facilitated switching of respective gas flows between the oxidation and reduction runs after fixed pre-determined cycle times. There was provision to measure pressure and temperature and preheat the feed gases to a temperature of 523.15 K prior to entering the reactor section. A 1 kW preheater was used for this purpose.

The reactor section (See Fig. 4.2) consists of a high temperature resistant stainless steel (SS) annular reactor (1 in. ID $\times$ 3 in. OD $\times$ 1 m L) enclosed in a vertically split tubular furnace. While the reactive gases were passed through the annular section facilitating combustion, coolant air was supplied via a pressure regulator (PR), rotameter and mass
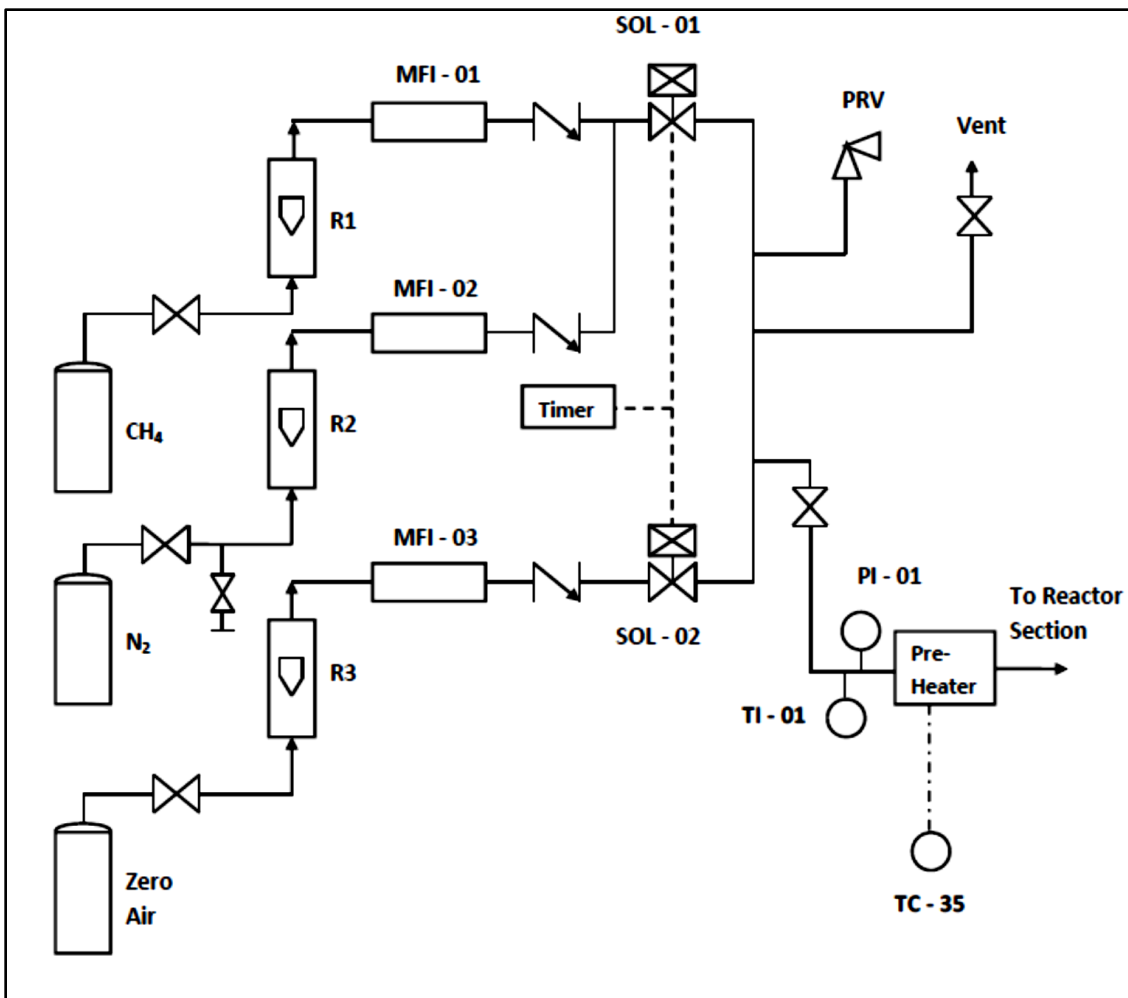
Fig. 4.1 Feed gas section [Notations used: MFI: Mass Flow Indicator; R: Rotameter; SOL: Solenoid valve; PI: Pressure Indicator; TI: Temperature Indicator; TC: Temperature Controller; PRV: Pressure Relief Valve]

flow indicator in a counter flow arrangement through the inner pipe. The furnace was divided into 3 zones of 330 mm each, with independent heating coils with an electric rating of 2.5 kW each and PID temperature controllers driven by thermocouples measuring reactor outer wall temperatures in these zones. The coils were used to preheat and thus maintain the bed in respective zones at a desired operating temperature in the range of 773.15 K – 973.15 K during the test runs and compensate for heat losses from the outer wall. The power supplied to these coils was recorded using digital energy meters.
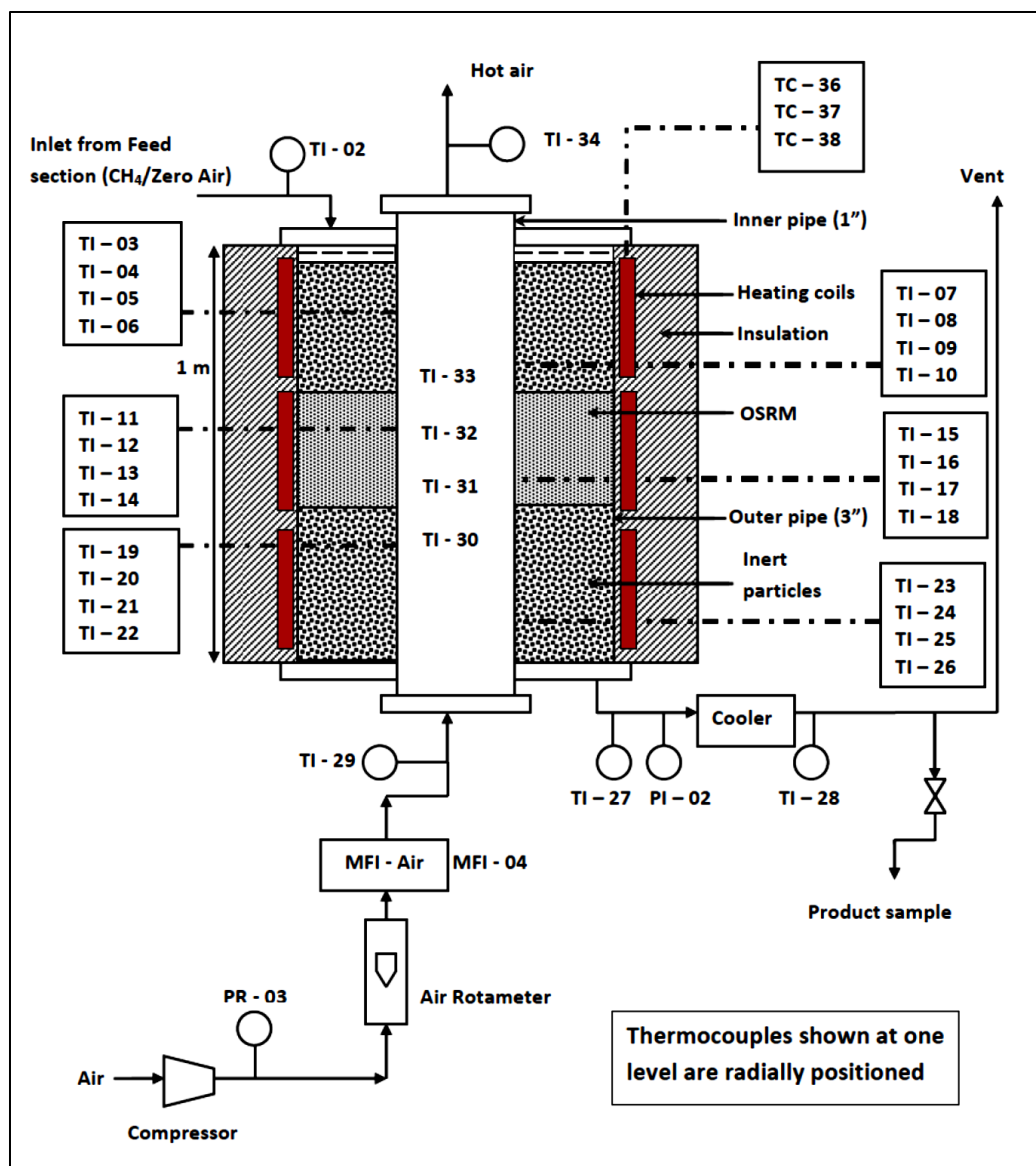
Fig. 4.2 Reactor section (representative sketch only) [Notations used: TI: Temperature Indicator; PR: Pressure Regulator; PI: Pressure Indicator; TC: Temperature controller]

The furnace assembly was adequately insulated and the space between the reactor and a furnace at the top and bottom was filled with insulating material to minimize heat loss. Pressure and temperature of the product gas stream exiting the reactor was recorded.

There was provision for measuring temperatures at 24 different locations (4 radial × 6 axial) in the annular section of the reactor and at 4 different locations in the inner pipe.
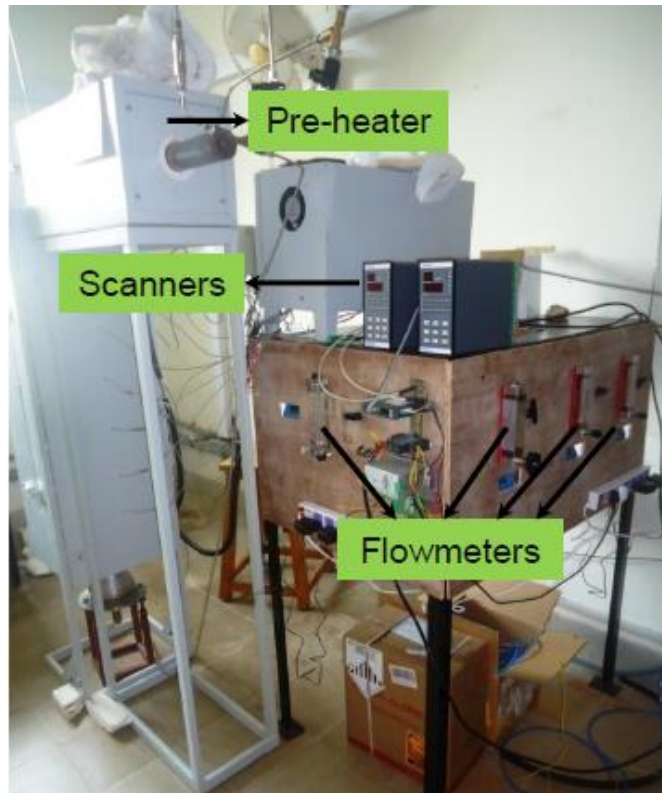
(a)
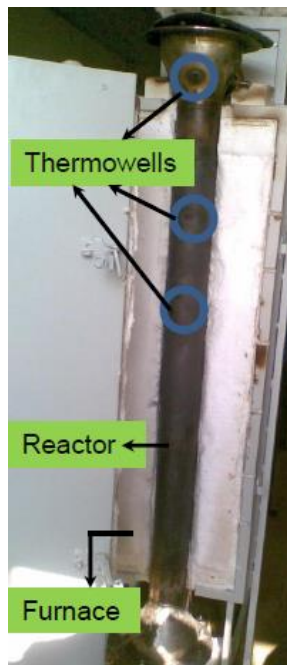
(b)

Fig. 4.3 (a) UMC based test rig (b) Annular packed bed SS reactor and furnace

Nickel-chromium / nickel-aluminium (K-type) thermocouples were used for measuring temperatures. The dimensions of the reactor and exact locations of each of the thermocouples are given in Appendix A. A SCADA based data acquisition system provided by MASIBUS^{TM} was used to record data every second during the test runs.

The product gases from the exit of the reactor were safely released into the atmosphere through an air cooler which facilitated lowering of temperature of the gas. A sampling point was provided in the exit line after the cooler. During sample collection, the gas was directed through this point to a sample tube provided with isolation valves via a condenser in which moisture was removed. The sample tube was purged with product gas for one minute prior to trapping of the gas in the tube. The tube was fitted with a septum and 0.5 to 2 cc of trapped gas was taken out from the tube using a gas syringe. This gas sample was then analyzed using an off-line Gas Chromatograph (GC) fitted with a TCD detector using molecular sieve and Porapak–Q packed columns for oxidation and reduction respectively

4.1.2   Instrumentation

4.1.2.1 Temperatures

The following temperatures were measured using nickel-chromium / nickel-aluminium (K type) thermocouples.

1. OSRM and inert bed at 24 locations (4 radial $\times$ 6 axial)
2. Reactive gas at the inlet of preheater
3. Reactive gas at inlet of reactor section
4. Product gas at outlet of reactor section
5. Product gas at outlet of air cooler
6. Coolant air at 4 axial locations in the inner pipe
7. Coolant air inlet
8. Coolant air outlet

All 34 thermocouples were calibrated against a standard K-type thermocouple in the range of 473.15 K to 1373.15 K. A SCADA based data acquisition system including an indicator, provided by MASIBUS^{TM} with an accuracy ± 0.1 % of full span, was used to record temperature data every second during the test runs. The MASIBUS indicator in turn was calibrated against each of the 34 thermocouples. The details of the calibration runs are given in Appendix B.

4.1.2.2 Pressure

The following gauge pressures were measured using pressure gauges (WIKA make), each having a range of $0 – 2.5$ kg/cm^2 (with an accuracy of ± 1.6 % of full scale).

1. Reactive gas at the inlet of preheater
2. Product gas outlet

These pressures were also recorded using respective pressure transmitters (WIKA make) having a range of $0 – 2.5$ kg/cm^2 (with an accuracy of ± 0.5 % of full scale).

4.1.2.3 Flowrates

Thermal mass flow indicators (MFI) supplied by Flui-Tech Instruments^{TM} were used to record the flowrates of gases reported in Table 4.1. The accuracy of each MFI was ± 1 % of full scale (FS).

Table 4.1

Flowmeter range for gases used in UMC based heat transfer investigations

S. No.	Gas	Range
1	Methane	0 – 20 LPM
2	Nitrogen	0 – 20 LPM
3	Process air	0 – 50 LPM
4	Coolant air	0 – 200 LPM

Rotameters supplied by Eureka Industrial Equipments[TM] were also used to indicate and control the flowrates of these gases and the range of these meters for respective gases was same as those of the MFIs. The accuracy of each meter was ± 3 % of FS. These flowmeters were calibrated at 2.0 bar (g) and 298.15 K.

4.2   Pulsed Micro-reactor (PMR) test rig for kinetic studies

4.2.1   General layout

The general lay-out of the PMR test rig to estimate kinetics of oxidation of Cu and reduction of CuO is shown in Fig. 4.4. Photographs of the assembled test rig and the reactor used in this study are shown in Fig. 4.5.
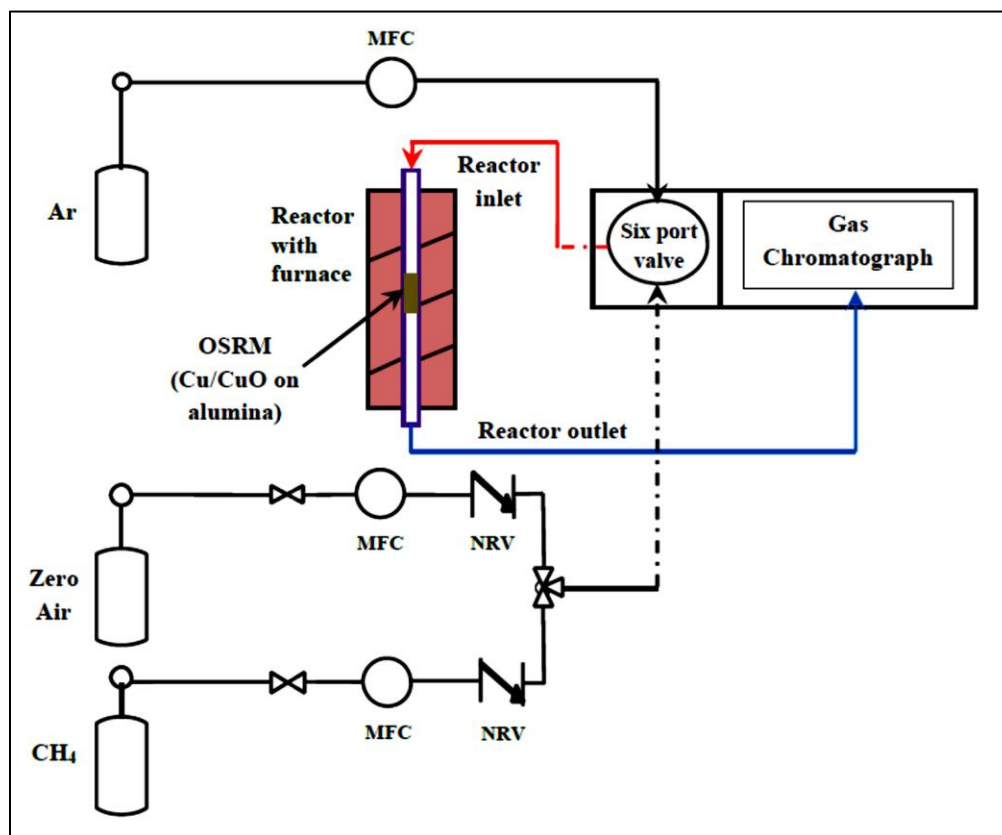
Fig. 4.4 Schematic of Pulsed Micro-reactor (PMR) test rig [Notations used: MFC: Mass Flow Controller; NRV: Non- Return Valve]
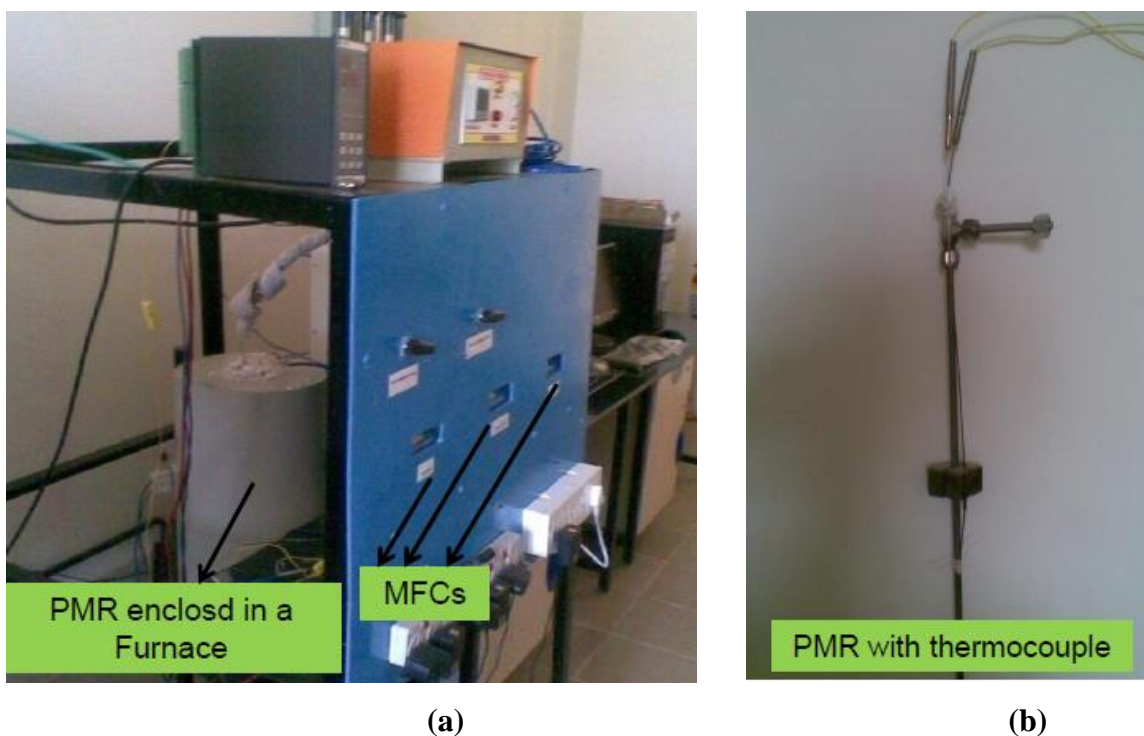
Fig. 4.5 (a) PMR test rig (b) Pulsed Micro-reactor

As shown in Fig. 4.4, the test rig consists of a high temperature stainless steel tubular reactor (3 mm ID x 700 mm length) enclosed in an electric furnace (50 mm ID x 500 mm length) fitted with a thermocouple and a PID temperature controller. This furnace, supplied by SMC instruments[TM], with an electric rating of 2.5 kW was used to heat the reactor system to a desired operating temperature in the range of 773.15 K – 973.15 K and maintain near isothermal conditions during the test runs. The relatively small tube diameter was consciously chosen to ensure that plug flow conditions would prevail in the reactor during the main test runs. The results from RTD study reported in section 7.2.1.1 validated this choice of tube diameter. The space between the reactor and a furnace at the top and bottom was filled with insulating material to avoid any heat loss. A K-type thermocouple was used to measure the reactor wall temperature. Product gases from the reactor were analyzed using an online Gas Chromatograph (GC) (Sigma Instruments[TM] make) fitted with a TCD detector, using molecular sieve and Porapak–Q packed columns for oxidation and reduction respectively.

Zero air (21 mol% O_2) and methane (CH_4) (99.5 mol %) were used as reactive gases for the oxidation and reduction test runs respectively. Argon was used as a carrier gas in the GC. The GC was integrated with an auto injector having a six port valve operated on zero air and a sample loop which facilitated feeding a small pre-determined quantity or pulse of reactive gas into the reactor. In normal operation mode of the six port valve (Fig. 4.6a), the reactive gas is directed through a sample loop to a vent while carrier gas is fed independently on a continuous basis to the reactor. At the time of injection of a pulse, the valve operates in a mode (Fig. 4.6b) wherein the carrier gas is made to flow through the sample loop for a fixed duration of time, directing a known amount of reactive gas, i.e. pulse to the reactor. This ensured that an entire volume of reactive gas hold up in the sample loop was fed to the reactor as a pulse during the test runs. For alternate cycles of oxidation and reduction, a subsequent pulse was injected only after completing the GC analysis of product gases resulting from previous pulse input. The set-up had provision to measure and control flowrates of these gases using respective thermal mass flow controllers (MFC) at the reactor inlet.

(a)   (b)
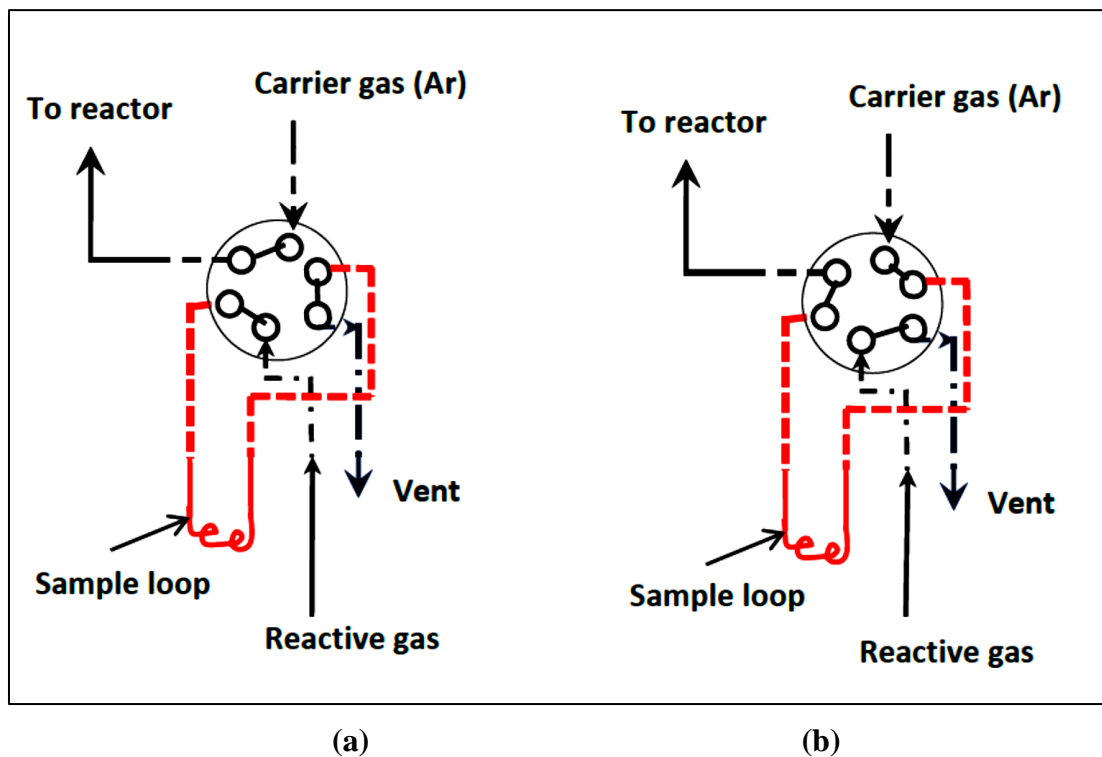
Fig. 4.6 Six port valve (a) during normal operation, (b) during pulse injection

4.2.2   Instrumentation

4.2.2.1 Temperatures

The temperatures at the reactor wall and inside the reactor were measured using nickel-chromium / nickel-aluminium (K type) thermocouples (supplied by Nu-tech Instruments^{TM}). Both thermocouples were calibrated against a standard K-type thermocouple in the range of 473.15 K to 1373.15 K. The standard thermocouple in turn was calibrated by the National Accreditation Board for Testing and Calibration Laboratories (NABL), India with an accuracy ranging from 1 to 2 K in this temperature range. The details of the calibration are given in Appendix B. MASIBUS^{TM} make indicator, with an accuracy of $\pm$ 0.1 % of full span, was used to record these temperatures.

4.2.2.2 Flowrates

Thermal mass flow controllers (MFCs) supplied by Flui-Tech Instruments^{TM} were used to measure and control flowrates of gases reported in Table 4.2. The range of these meters for respective gases is also presented in the same Table.

Table 4.2

Flowmeter range for gases used in PMR based kinetic studies

S. No.	Gas	Range
1	Argon	0 – 100 SCCM
2	Methane	0 – 100 SCCM
3	Air	0 – 100 SCCM

The accuracy of each meter is $\pm$ 1 % of full scale as specified by the vendors.

Chapter 5

Experimental Procedure

The experimental procedures used for investigating UMC for heat transfer applications and estimating kinetic parameters of Cu based OSRM reactions using Pulsed Micro-reactor (PMR) are presented in sections 5.1 and 5.2 respectively.

5.1   Investigation of UMC for heat transfer applications

A fixed quantity of 13 wt% CuO on alumina particles (OSRM) sandwiched between inert alumina particles of average diameter 2 mm was loaded in the 1 m annular section of the reactor. The inert particles provided support and facilitated uniform flow and temperature distribution of process gas at the entry to this zone. The OSRM particles were procured from Sigma Aldrich[TM], having specifications as shown in Table 5.1.

Table 5.1

OSRM specifications (13 wt% CuO on alumina)

Average particle diameter[a]	1.1 mm
BET surface area[b]	210.3 m^2/g
Particle porosity[b]	0.3
Density[b*]	4285 kg/m^3

[a] provided by Sigma-Aldrich[TM]; [b] estimated (Appendix D); * excluding pore volume

The test rig was assembled as shown in Fig. 4.1 and Fig. 4.2 and successfully leak tested at 200 kPa(g) with N_2 gas to assess its integrity under conditions in which the experimental runs were proposed to be carried out. For a prescribed OSRM loading, coolant air flow was first initiated through the inner pipe and set to a pre-desired value. The entire 1 m long bed comprising of the OSRM and inert was then heated to a desired temperature using the external heating coils. Nitrogen was then passed through the bed

simulating "no reaction" conditions. The system was allowed to reach steady state in terms of coolant and bed temperatures.

The OSRM was subsequently subjected to alternate cycles of reduction and oxidation using desired flowrates of methane (CH_4) – nitrogen (N_2) mixture and zero air respectively. The run was continued until a "cyclic" steady state was attained wherein the difference between the highest and lowest temperatures of the OSRM at measured locations in one cycle was found not to vary with time in consecutive oxidation and reduction cycles respectively. Respective temperatures and pressures were continuously recorded. At "cyclic" steady state, product gases were analyzed for N_2 and unreacted O_2 in case of oxidation while CO_2, CO, H_2 and unreacted CH_4 were analyzed in case of reduction. In all 6 samples were collected at pre-determined intervals of 2 minutes and 1 minute during oxidation and reduction respectively.

Experiments were performed using a representative loading of 1.25 kg of OSRM, located at 0.37 m from the top of the reactor and in alignment with zone 2 of the furnace. This corresponded to a bed height 270 mm. Experiments were conducted for different flowrates of zero air, CH_4 and coolant flowrate and reactive gas inlet temperatures. A total of 11 experiments covering all the desired parameters were conducted. Each experiment was repeated three times to confirm consistency in results obtained. The time required to complete a typical experimental run including start-up and shutdown of the test rig was close to 10 hours. All necessary safety precautions were taken by following relevant standard procedures during each of these runs.

The experiments were always initiated with reduction and terminated with oxidation ensuring equal number of respective cycles at the end of each run. The range of parameters covered in the main test runs are summarized in Table 5.2. The flowrates and concentrations chosen ensured reasonable oxidation and reduction cycle times and that no coke was formed in the bed during the test runs. Under these conditions, the bed temperature was maintained between 773.15 K and 973.15 K during the test runs which facilitated sustaining respective reactions in the bed and avoiding formation of coke and

possibility of undesired reactions. The cycle times shown in Table 5.2 allowed for effective switching of reactive gases between oxidation and reduction at which point the bed was considered to have completely reacted. The methane concentration was varied by adjusting CH_4 and N_2 flowrates. The total flowrate of the $CH_4 - N_2$ mixture was however maintained at 20 LPM in all the runs.

Table 5.2

Experimental conditions used in UMC based heat transfer investigations

		1.25 kg OSRM
Reduction	CH_4 flowrate (LPM)	2 – 6
	N_2 flowrate (LPM)	14 – 18
	Cycle time (min)	8
Oxidation	Zero air flowrate (LPM)	5 – 20
	Cycle time (min)	12
Coolant air flowrate (LPM)		100 – 175
Reactive gas inlet temperature (K)		873.15 – 923.15
Reactive gas pressure at the inlet (bar (g))		0.4
Inlet coolant pressure (bar (g))		1.8

At the end of each run, CH_4 and zero air flows to the reactor were first stopped by closing respective valves. N_2 flow through a bypass line was then initiated and coolant air flow through the inner pipe was maintained. Solenoid valves were then switched off. The reactor and preheater temperature was brought down to ambient conditions by slowly reducing the power supply to the furnace. Finally coolant air flow and N_2 flow were stopped and the experiment was terminated by switching off external power to the test rig.

5.2   Estimation of kinetic parameters using Pulsed Micro-reactor (PMR)

5.2.1   Preliminary experiments

A near isothermal zone, 70 mm in height and 200 mm from the reactor inlet, was first identified to ensure that the OSRM bed temperature remained stable during the main test runs. The OSRM material was subsequently placed in this zone in which the temperature variation did not exceed 2 K with depth at any point of time and in the range of 673.15 – 973.15 K.

In the presence of solid, the narrow internal reactor dimensions did not allow for easy measurement of OSRM bed temperature using a thermocouple and the same was therefore determined indirectly by measuring the reactor wall temperature. Using a procedure adopted by Zamostny et. al. [33] a series of measurements without solid at different carrier gas flowrates was first made in relation to the outer wall temperature. The data obtained was fitted using the method of least squares resulting in a 2nd order polynomial equation (with $R^2 \sim 0.99$) as shown below.

$$T_{b,PMR} = 2 \times 10^{-5} T_w^2 + 0.979 T_w + 15.31 \tag{5.1}$$

The relation was found to be independent of carrier gas flowrate within the range of values employed in the main PMR test runs and was subsequently used to estimate the bed temperature during these runs.

A Residence Time Distribution (RTD) approach was used to confirm near plug flow conditions in the PMR and avoid axial dispersion. The presence of axial dispersion can result in non-uniform reaction rates and incorrect estimation of kinetic parameters, more so when non-isothermal conditions prevail as in the case of exothermic/endothermic reactions. In this study, 100 mg sample of oxidized OSRM was placed in the pre-identified isothermal zone in the reactor. The reactor was maintained at a particular temperature of interest using an electric furnace. Pulses of 0.5 cc of zero air (oxygen)

were injected at a fixed flowrate along with a carrier gas. During this process, the reactor wall temperature was continuously recorded for variation if any at all. After every pulse injection, the product gas from the reactor was analyzed using the online GC. The GC data was used as input to determine the RTD response of the reactor to the pulse injection which in turn was then used to estimate the Dispersion number (Di). A similar RTD study was carried for CH_4 flow over completely reduced OSRM at the same temperature and flowrate using a sample loop of 0.1 cc. Plug flow conditions can be assumed in such a reactor system for values of Di < 0.001 [56]. The investigation was carried out over a range of flowrates (30 – 40 SCCM) and temperature (673.15 K – 973.15 K) of interest. The results of this study are discussed in section 7.2.1.1.

The GC parameters used in the present study and retention times of product gases at the PMR exit are presented in Appendix C.

5.2.2   Oxidation and reduction test runs

A fixed quantity of 13 wt% CuO on alumina particles (OSRM) sandwiched between inert quartz wool was placed inside the reactor. The inert material provided support and facilitated uniform flow and temperature distribution of reactive gas through the reactor. The OSRM particles having specifications as shown in Table 5.1 were procured from Sigma Aldrich^{TM}. The pore volume distribution analysis confirmed that no micro-pores were present and primarily meso and macro pores contributed to pore volume. The analysis report is included in Appendix D.

The test rig was assembled as shown in Fig. 4.4 and successfully leak tested at 400 kPa (g) with Argon gas to assess its integrity under conditions in which the experimental runs were proposed to be carried out. Trial runs were first performed to determine the amount of OSRM and sample loop volume required to be injected as a pulse into the reactor system during the main test runs. The bed was first heated to a desired temperature and subsequently subjected to alternate cycles of oxidation and reduction. Increasing the amount of OSRM or reducing sample volume resulted in the injection of an increased

number of pulses required to completely convert the solid reactant. Decreasing the OSRM amount or increasing sample volume resulted in less number of pulses. The results from the trial runs are shown in Table 5.3 which also summarizes the experimental conditions under which the main test runs were carried out. It was anticipated at this stage that quantity of OSRM chosen would yield sufficient data points to estimate the reaction order and rate constant for both reactions. However in the case of reduction, the number of data points was later found to be insufficient for determining the order with respect to solid and for this case, the OSRM quantity was subsequently increased to 400 mg in the main test runs. More details are provided in section 7.2.2.2.

Table 5.3

Experimental parameters used in PMR test runs

Parameters	Oxidation	Reduction
Sample loop volume (cc)	0.5	0.1
Amount of OSRM (mg)	100	100*
Absolute Pressure (kPa)	250	250
Reaction Temperature (K)	673.15 – 873.15	873.15 – 973.15
Carrier gas flowrate (SCCM)	35 – 40	35 – 40

*Increased to 400 mg as discussed in section 7.2.2.2

The main experiments were carried out at temperatures of up to 873.15 K for oxidation and 973.15 K in the case of reduction at intervals of 25 K. Both reactions were investigated independently. However, in both cases, the OSRM was reduced and oxidized in the previous step at 873.15 K using CH_4 and air respectively. The temperature fluctuation in the bed during these runs was not more than ± 2 K due to small quantities of reactive gas injected in every pulse and continuous flow of inert carrier gas. The carrier gas flowrate range was chosen to ensure continuous GC operation and that external mass transfer effects remain negligible. The latter was confirmed using the Mears′ criterion and the same is discussed in section 7.2.3.

Chapter 6

Data Reduction and Methodology

The properties of air, methane, nitrogen, copper, copper (II) oxide and alumina were estimated using the equations listed in Appendix E. Temperatures were measured using nickel-chromium / nickel-aluminium (K type) thermocouples. The resultant MASIBUS indicator readings were converted to actual temperatures using appropriate calibration equations (see Appendix B). The volumetric flowrates of gases indicated by respective flowmeters were corrected for temperature and pressure using the following expression

$$\dot{V}_{g,act} = \frac{P_{g,cal}\ T_{g,act}}{P_{g,act}\ T_{g,cal}}\ \dot{V}_{g,ind}$$ (6.1)

where

g   respective gas flowing through the flowmeter i.e. zero air, methane, nitrogen or coolant air

cal   operating conditions under which respective flowmeters were calibrated

act   actual operating conditions

6.1   UMC based heat transfer investigations

6.1.1   Coolant mass flowrate

The volume flowrate of coolant air flowing through the inner pipe of UMC based heat transfer test rig was measured using a rotameter. The mass flowrate of coolant was calculated as follows:

$$\dot{m}_c = \rho_c \dot{V}_{c,act}$$ (6.2)

where ρ_c is the density of coolant evaluated at the average of time averaged coolant inlet and outlet temperatures of the considered section. $\dot{V}_{c,act}$ is estimated using expression (6.1).

6.1.2 Furnace power

The power dissipated by the heating coils in different zones of the furnace was calculated from kWh readings recorded using respective digital energy meters at specific time intervals.

$$\dot{Q}_{ext} = \frac{(kWh\ reading)_{t_2} - (kWh\ reading)_{t_1}}{(\Delta t/3600)} \qquad (6.3)$$

where

$$\Delta t = \text{time interval} = t_2 - t_1$$

6.1.3 Total heat transfer to the coolant

For each of the main test runs, the total heat transfer to coolant air under "reaction" conditions from the OSRM bed in alignment with zone 2 of the furnace was evaluated using

$$Q_c = \dot{m}_c \times C_{pc} \times \Delta T_c \times \left(n_c \times \left(t_{c,ox} + t_{c,red} \right) \right) \qquad (6.4)$$

where ΔT_c is the coolant temperature rise evaluated based on time averaged inlet and outlet temperatures and n_c is the number of cycles with each cycle including oxidation and reduction.

The percentage of total energy in the bed transferred radially to coolant was then estimated as

$$\text{\% of Radial heat transfer} = \frac{Q_\text{c}}{(Q_\text{ox} + Q_\text{red} + Q_\text{ext})} \times 100 \tag{6.5}$$

where

$$Q_\text{ox} = \Delta H_\text{ox} \times X_\text{ox} \times (\text{moles of } O_2 \text{ fed in } n_\text{c} \text{ oxidation cycles}) \tag{6.6}$$

$$Q_\text{red} = \Delta H_\text{red} \times X_\text{red} \times (\text{moles of } CH_4 \text{ fed in } n_\text{c} \text{ reduction cycles}) \tag{6.7}$$

$$Q_\text{ext} = \dot{Q}_\text{ext} \times \left(n_\text{c} \times \left(t_\text{c,ox} + t_\text{c,red} \right) \right) \tag{6.8}$$

For each run, the reactor conversion X was obtained using

$$X = \frac{\text{moles fed} - \text{moles unreacted}}{\text{moles fed}} \tag{6.9}$$

The number of moles fed and unreacted was calculated from the reactive and product gas composition and flowrate at the reactor inlet and outlet respectively. Steady state coolant and OSRM / inert temperatures attained in the absence of chemical reaction were used as reference temperatures in the heat transfer calculations.

6.2   Methodology adopted in PMR based kinetic studies

For any non-catalytic gas-solid reaction represented by aA (s) + bB (g) $\rightarrow$ products, the rate equation can be expressed using a power law having form

$$- r''_\text{s} = k''_\text{e} \, c_\text{g}^n \, c_\text{s}^m \tag{6.10}$$

where m and n are reaction orders with respect to solid and gaseous reactant respectively. In the absence of external mass transfer, the rate of reaction can be limited by surface reaction or pore diffusion. This methodology is initiated by assuming surface reaction as

48

the rate limiting step. For such reactions, the effective rate constant k''_e in equation (6.10) reduces to k''_1 and the equation can be rewritten as

$$-r''_s = -\left(\frac{a}{b}\right) r''_g = k''_1 \, c_g^n \, c_s^m \tag{6.11}$$

Using the method of excess with respect to gaseous reactant wherein c_g remains constant ($\sim c_{go,N}$), equation (6.11) assuming uniform reaction reduces to

$$-\frac{1}{S_a \rho_b} \frac{dc_s}{dt} = k_2 c_s^m \tag{6.12}$$

where

$$k_2 = k''_1 \, c_{go,N}^n \tag{6.13}$$

$c_{go,N}$ is the concentration corresponding to the total quantity of gaseous reactant fed to the reactor in N pulses required to completely saturate the available solid reactant and is estimated using

$$c_{go,N} = \frac{N \times A_o}{V_b} \tag{6.14}$$

Integrating equation (6.12) gives,

$$\int_{c_{so}}^{c_{si}} \frac{dc_s}{c_s^m} = \int_0^{t_i} k_2 S_a \rho_b \, dt \tag{6.15}$$

where

$$t_i = \frac{i \times V_b}{q} \tag{6.16}$$

The integration yields the following equations for fraction of unconverted solid at the end of the ith pulse for $m \neq 1$ and $m = 1$ respectively.

$$(c_{si}/c_{so})^{1-m} = 1 - \frac{i\,(1-m)\,k_2 S_a\,\rho_b\,V_b}{q\,c_{so}^{1-m}} \quad \text{(for } m \neq 1) \tag{6.17}$$

$$\ln\,(c_{si}/c_{so}) = -\frac{i\,k_2\,S_a\,\rho_b V_b}{q} \quad \text{(for } m = 1) \tag{6.18}$$

At a given temperature of interest, a graph of $(c_{si}/c_{so})^{1-m}$ or $\ln\,(c_{si}/c_{so})$ vs i is plotted assuming different values of m. The value of m for which a particular plot yields a straight line with the best fit is considered as the order of reaction with respect to solid.

Similarly using method of excess, with regard to the solid reactant, wherein c_s remains constant $(\sim c_{so})$, equation (6.11) reduces to

$$-\frac{(a/b)\,dc_g}{S_a\rho_b\,dt} = k_3 c_g^n \tag{6.19}$$

where

$$k_3 = k''_1\,c_{so}^m \tag{6.20}$$

Integrating equation (6.19) gives,

$$\int_{c_{go,N}}^{c_{gi}} \frac{dc_g}{c_g^n} = -\frac{b}{a}\int_0^{t_i} k_3 S_a\rho_b\,dt \tag{6.21}$$

The integration yields the following equations for fraction of unconverted gas at the end of the ith pulse for $n \neq 1$ and $n = 1$ respectively.

$$\left(c_{gi}/c_{go,N}\right)^{1-n} = 1 - \frac{i\,(1-n)\,k_3\,S_a\,\rho_b V_b}{(a/b)\,q\,c_{go,N}^{1-n}} \quad \text{(for } n \neq 1) \tag{6.22}$$

$$\ln\left(c_{gi}/c_{go,N}\right) = -\frac{i\,k_3\,S_a\,\rho_b V_b}{(a/b)q} \quad \text{(for } n = 1) \tag{6.23}$$

For the value of m obtained earlier at a given temperature, a graph of $\left(c_{gi}/c_{go,N}\right)^{1-n}$ or $\ln\left(c_{gi}/c_{go,N}\right)$ vs i is now plotted assuming different values of n. The value of n for which a particular plot yields a straight line with the best fit is considered as the order of reaction with respect to the gas at the same temperature. The slope of this linear plot estimated from equations (6.22) or (6.23) depending on the value of n, is then used to estimate k''_1 at this temperature.

The value of k''_1 is then estimated at different temperatures. k''_o and E can be estimated using an Arrhenius plot of $\ln\left(k''_1\right)$ vs $1/T$.

The uniform reaction methodology was adopted in this study considering the relatively mild conditions under which relevant reactions were investigated and that the solid reactant (in this case Cu / CuO) was uniformly distributed over porous alumina.

6.2.1   Influence of external mass transfer and pore diffusion

The rate limiting step is then confirmed thereafter using the Weisz-Prater and Mears' criteria [56]. While the former provides an estimate on pore diffusion effects on reaction rate of heterogeneous gas-solid reactions, the latter provides an insight into whether external mass transfer is rate limiting. These criteria in terms of respective parameters are explained here in this section.

According to the Mears' criterion, external mass transfer can be neglected if

$$\frac{-r_g^{''}(\exp)S_a\rho_b R\,n}{k_c c_{go,N}} < 0.15 \tag{6.24}$$

where $-r_g^{''}(\exp)$, S_a, ρ_b, R, n, k_c, and $c_{go,N}$ denote the experimental reaction rate per unit surface area of the catalyst, surface area per unit mass, solid bed density, average particle radius, order of reaction, mass-transfer coefficient and concentration of gaseous reactant at inlet respectively.

In the present investigation, the values of parameters in equation (6.24) were estimated under conditions in which the main test runs were carried out. The experimental reaction rate was obtained using the data on fraction of reactant converted at different times. Specific surface area of the solid was determined using a BET surface area analyzer (Model: SMART SORB 93 from Smart Instruments[TM]). The value of mass-transfer coefficient was estimated using the Frossling [56] correlation for flow through a packed bed as follows

$$Sh = 2 + 0.6\left(Re_p\right)^{1/2}Sc^{1/3} \tag{6.25}$$

where Sh, Re_p and Sc are Sherwood, Reynolds and Schmidt numbers respectively. Here the molecular diffusivity (D_{AB}) was estimated using Chapman-Enskog equation [49]. The values of diffusivities were of the order of 10^{-4} and 10^{-5} m^2/s in case of oxidation and reduction respectively.

According to Weisz-Prater criterion pore diffusion can be neglected if

$$C_{WP} = \left(\frac{-r_g^{''}(\exp)S_a\,\rho_b R^2}{D_e c_{gs}}\right) << 1 \tag{6.26}$$

The effective diffusivity (D_e) was calculated using following correlation [69].

$$D_e \approx \varepsilon_p^2 D_{AB} \tag{6.27}$$

Chapter 7

Results and Discussion

In this chapter, the findings and the analysis of the experimental investigations related to UMC based heat transfer to coolant air are presented and discussed first followed by those related to estimation of kinetic parameters of oxidation and reduction reactions involving Cu based OSRM using the Pulsed Micro-reactor (PMR) technique.

7.1   Experimental investigations of UMC for heat transfer applications

7.1.1   Heat transfer

Two illustrative experimental results under a loading of 1.25 kg OSRM are presented in Table 7.1. The flowrates indicated by flowmeters are reported here. Corrected flowrates and results of all experimental test runs are given in Appendix F. The percentage of radial heat transfer from the OSRM bed during the entire combustion process involving 7 cycles was estimated using the methodology suggested in section 6.1. The results indicate that upto 95% of energy in the bed is radially transferred. This energy transfer is primarily by conduction in the solid bed. As discussed later in this section, this energy transfer at "cyclic" steady state was under sustained combustion conditions.

Prior to the start of each of the main test runs, as mentioned in section 5.1, the coolant and bed temperatures were allowed to reach respective steady state values wherein only nitrogen was passed through the system. Under this "no reaction" condition, the coolant heat transfer rate and the total heat transfer from the OSRM and inert bed in alignment with zone 2 of furnace was estimated. This was subtracted from the coolant heat transfer in the main test run under "reaction" conditions to obtain the total heat transfer from the OSRM bed.

Table 7.1

Experimental conditions and percentage of radial heat transfer for two illustrative runs*

Run. No.	Flowrate (LPM)				Gas inlet temperature (K)	Total energy available in the bed in 7 cycles (kJ)	% of Radial heat transfer	External power supply (%)
	Zero air	CH$_4$	N$_2$	Coolant				
1	15	2	18	125	873.15	3686 ± 67	86 ± 2	32
2	15	2	18	150	873.15	3856 ± 71	95 ± 2	35

*Data presented for 7 cycles

For run 1, the OSRM bed temperature measured by thermocouples TI – 12 and TI – 14 at two different radial locations close to reactor inlet is shown in Fig. 7.1. The bed temperature is found to initially increase for the first 5 reduction and oxidation cycles. From the 6th cycle onwards corresponding to 100 minutes of operation, a "cyclic" steady state condition as defined in section 5.1 is attained and the variation of temperature with time under this condition is shown in Fig. 7.2. The test rig was operated for 40 minutes under this condition during which the maximum temperature rise was found not to exceed 10 K and 60 K for reduction and oxidation respectively. The temperature rise is always observed to be greater in the case of oxidation as compared to reduction due to higher reaction enthalpy and reaction rate.

In each oxidation and reduction cycle, the bed temperature increases at first to a maximum and then decreases. As a result of the gas–solid reaction, a reaction front moves axially past every location in the bed at different times wherein the reactive gas fed reacts with a stoichiometric amount of the solid material resulting in temperature rise in the bed during respective reactions. Along with the reaction front, a delayed heat front also propagates past these reacted locations at different times as a consequence of the temperature difference between the bed and subsequent incoming gas flow. At the heat front, the energy stored in the solid material as a result of its heat capacity is transferred to the gas phase due to axial convection and this in combination with the radial heat transfer results in cooling of the bed. The variation of temperature under "cyclic" steady
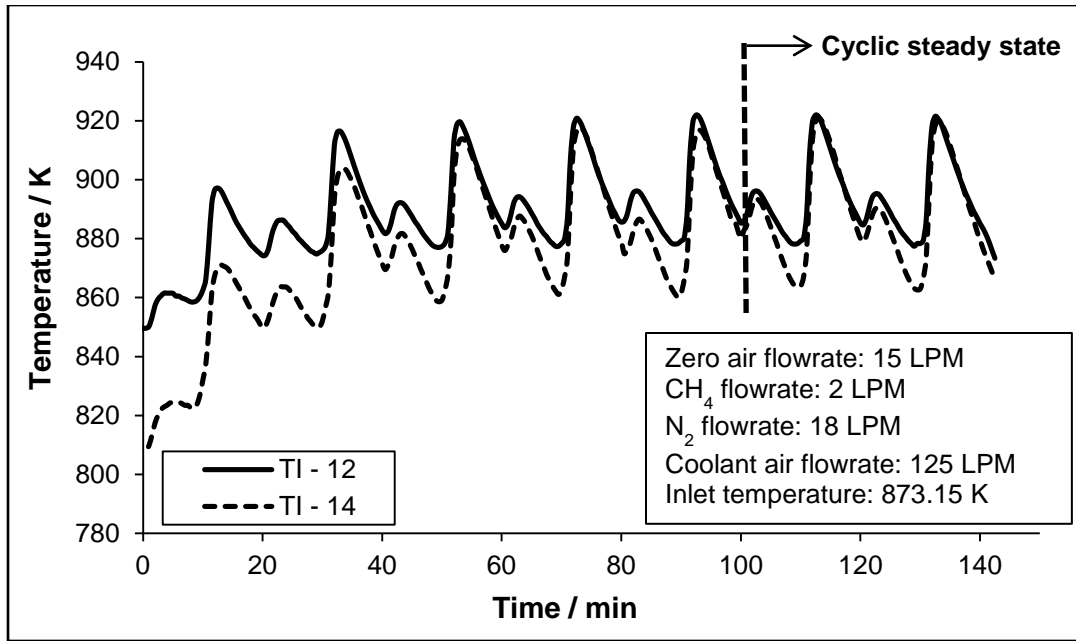
Fig. 7.1 Variation of bed temperature with time at two radial locations ($r = 8$ and 18 mm from the outer wall and at $z = 0.42$ m from top) for run 1
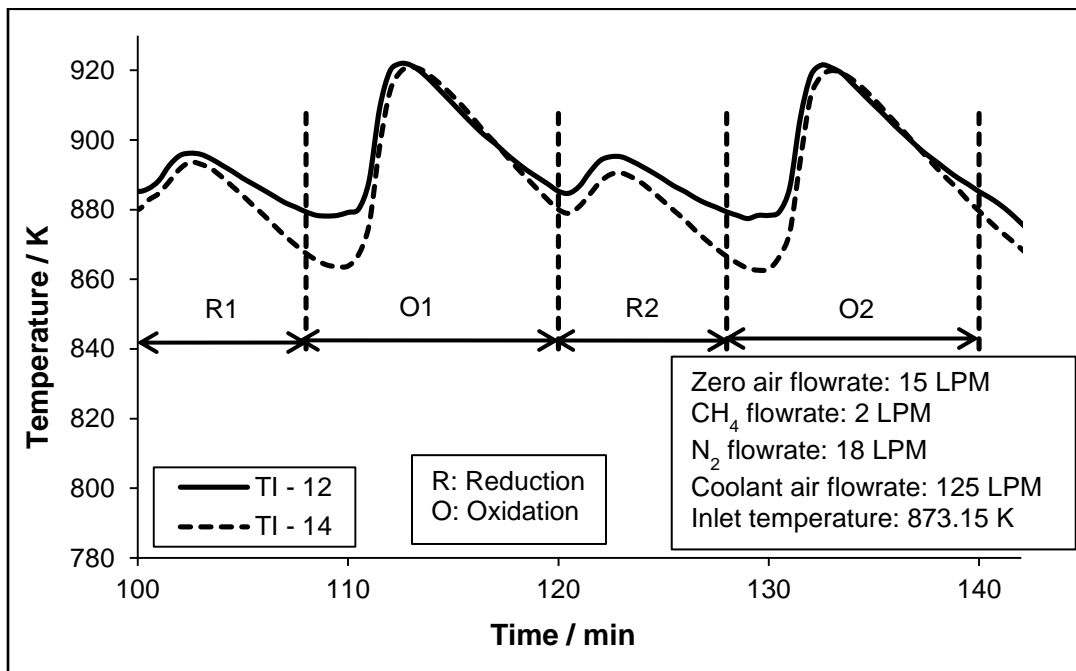
Fig. 7.2 Variation of bed temperature with time at two radial locations ($r = 8$ and 18 mm from the outer wall and at $z = 0.42$ m from top) at "cyclic" steady state for run 1

state conditions is shown in Fig. 7.2. It may be noted that the start of oxidation and reduction shown in this figure corresponds to the time at which switchover occurs and respective gases enter the reactor. However the temperatures at these two thermocouple locations continue to decrease beyond this time and then increase indicating the start of respective reactions. The overall decrease in both cycles prior to start of respective reactions at TI – 12 and TI – 14 can be attributed to the combined effect of coolant air heat transfer and convective gas flow from the previous cycle prior to changeover.

The rate of cooling after the reduction cycle at the TI – 14 location is comparatively higher due to close proximity of this location to the coolant. It is interesting to note that 86% of radial heat transfer to coolant air was possible in run 1 under cyclic operating conditions in the bed. Similar trends were obtained for run 2 and the same is presented in Fig. 7.3 and Fig. 7.4. Due to higher coolant air flowrate, the maximum bed temperature rise at "cyclic" steady state (after the 5th cycle) was lower (~8 K for reduction and 40 K for oxidation) as compared to rise obtained in run 1. The fraction of radial heat transfer in this case is also higher i.e. 95%.
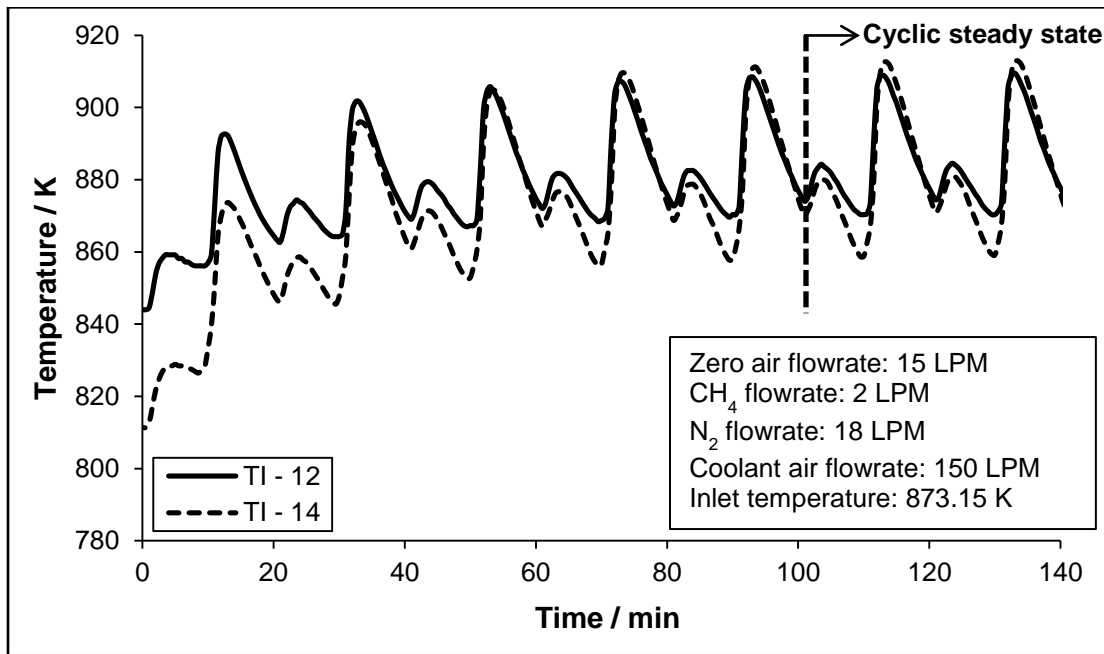
Fig. 7.3 Variation of bed temperature with time at two radial locations ($r = 8$ and 18 mm from the outer wall and at $z = 0.42$ m from top) for run 2
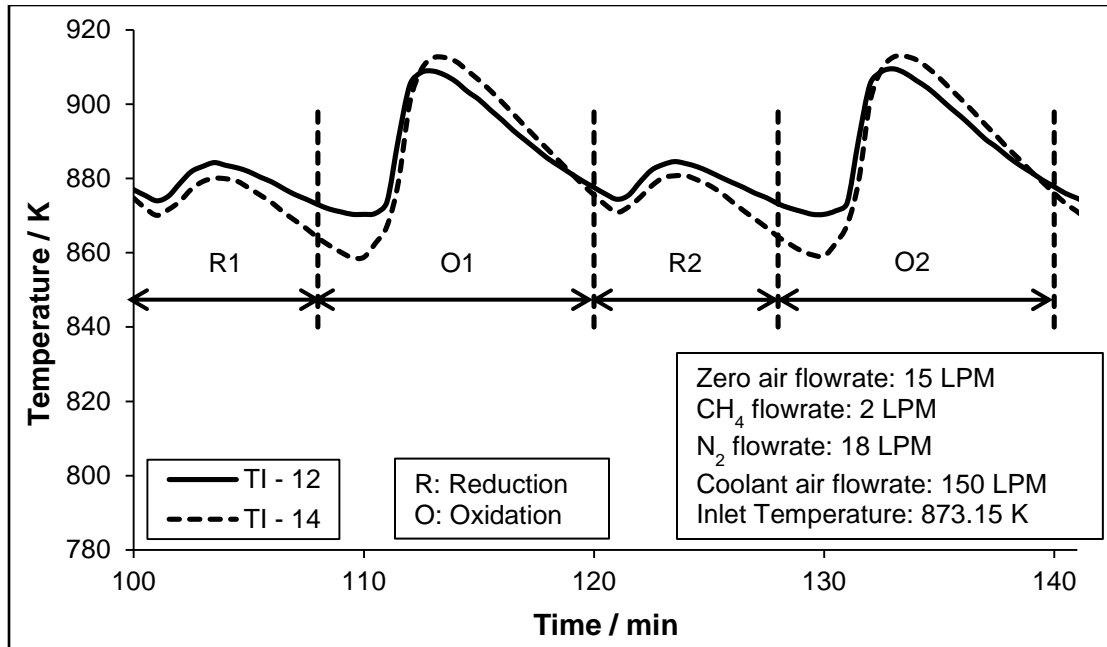
Fig.7.4 Variation of bed temperature with time at two radial locations ($r = 8$ and 18 mm from the outer wall and at $z = 0.42$ m from top) at "cyclic" steady state for run 2

The coolant air temperature rise with time for both runs at the outlet of the zone under consideration is shown in Fig. 7.5 and Fig. 7.6 respectively. The temperature in both cases was found to increase initially for the first 100 minutes prior to reaching a "cyclic" steady state condition wherein the difference between highest and lowest temperatures was less than 5 K, i.e. stable.

The percentage of radial heat transfer to coolant air shown in Table 7.1 is inclusive of the heat generated during respective reactions and power supplied by external heater coil in zone 2. For both runs, this power supply contributed to 32% and 35% of the total energy available in the bed for transfer across all 7 cycles. Of this, approximately 26% and 28% was confined to the first 5 cycles prior to the system reaching a "cyclic" steady state.

After the 5th cycle, the power supply contribution was restricted to 6% and 7% indicating that most of the energy transferred radially was from the heat generated in respective reactions and that the combustion process was self-sustaining. The variation of external power supply in kW with time for the two illustrative runs at coolant flowrates of 125 and
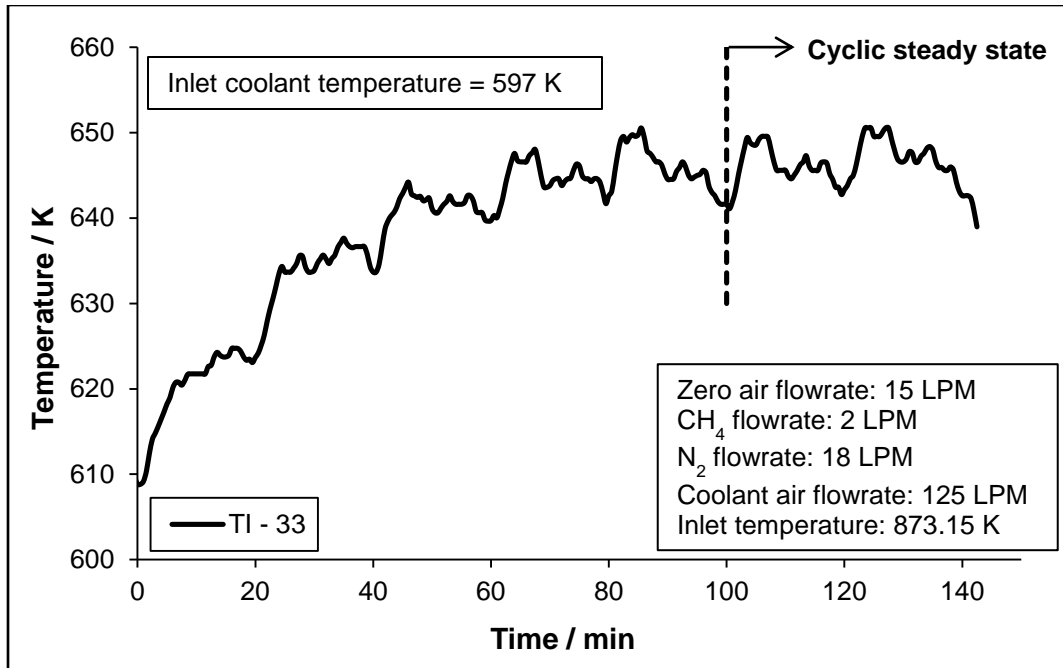
Fig. 7.5 Variation of coolant air outlet temperature as measured by TI – 33
with time for run 1
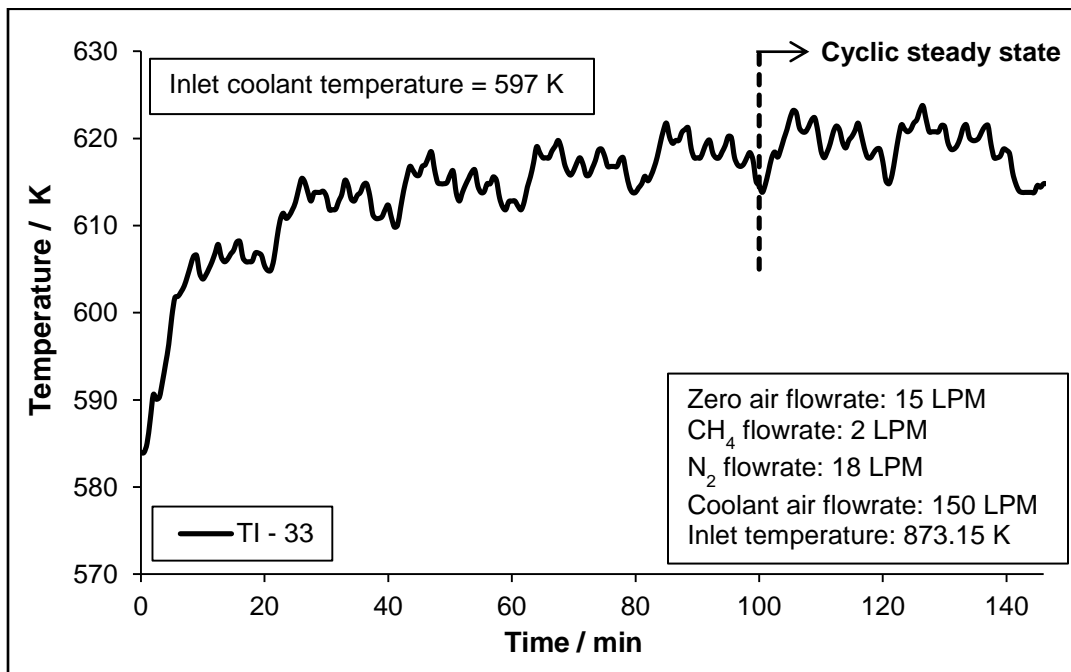
Fig. 7.6 Variation of coolant air outlet temperature as measured by TI – 33
with time for run 2

150 LPM is shown in Fig. 7.7. It is observed that the power requirement decreases with time and under "cyclic" steady state operation attains a near fixed value of 126 and 175 kW for respective flowrates wherein the combustion process becomes self-sustained. The external supply is higher in the case of 150 LPM to compensate for the relatively larger decrease in OSRM bed temperature as compared to 125 LPM.
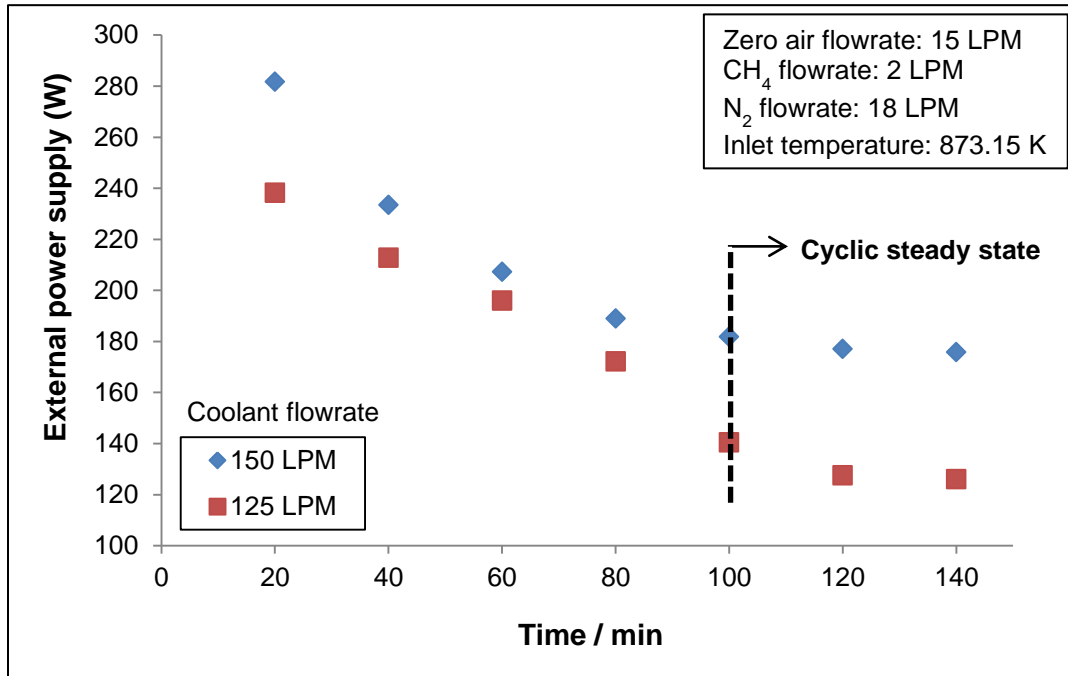
Fig. 7.7 Variation of external power supply with time for two illustrative runs

The variation of bed temperature measured by thermocouples TI – 14 and TI – 18 at two axial locations is shown in Fig. 7.8. After an initial increase, the bed temperature measured by TI – 18 as in the case of TI – 14 reaches a "cyclic" steady state. The propagation of the reaction and heat front is also seen in Fig. 7.9 with respect to the two locations. The response of TI – 18 lags that of TI – 14 by almost 5 minutes. The bed temperature rise at the TI – 18 location is approximately 14 K and 12 K lower for oxidation and reduction respectively as compared to the rise measured at the TI – 14 location due to increased temperature difference between the bed and the coolant as a result of the counter current flow arrangement resulting in increased radial heat transfer. The heat transfer as a result of convective gas flow from the previous cycle adds to this

cooling effect. It is more pronounced in the case of reduction as seen in Fig. 7.9 where a temperature rise of only ~2 K is observed.
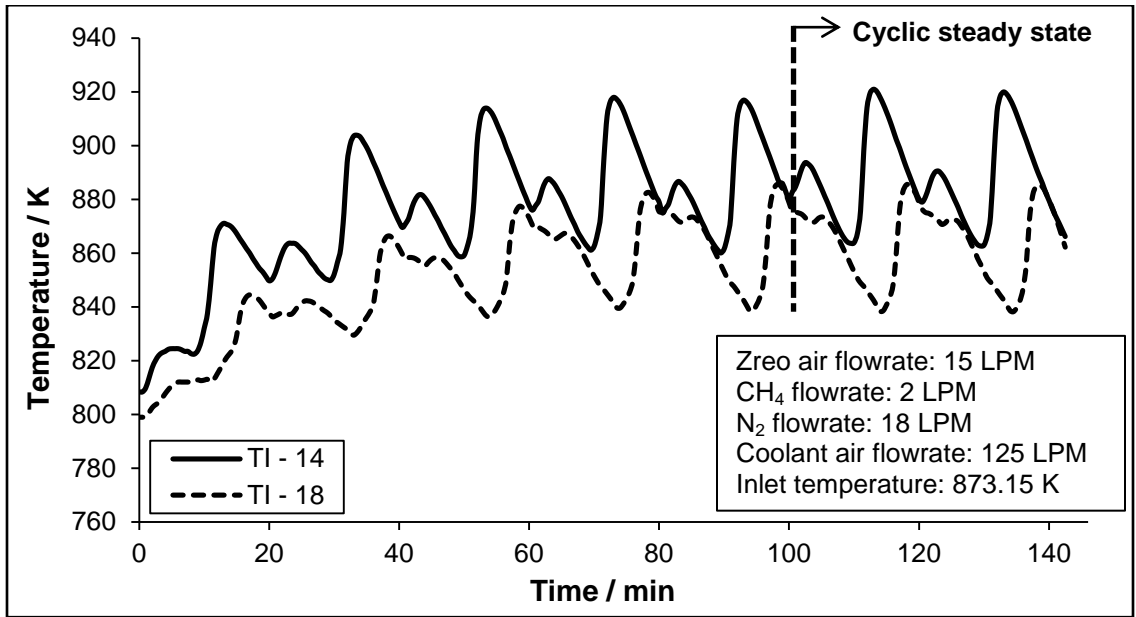
Fig. 7.8 Variation of bed temperature with time at two axial locations (at $z = 0.42$ m and $z = 0.58$ m from the top and at $r = 18$ mm from outer wall) for run 1
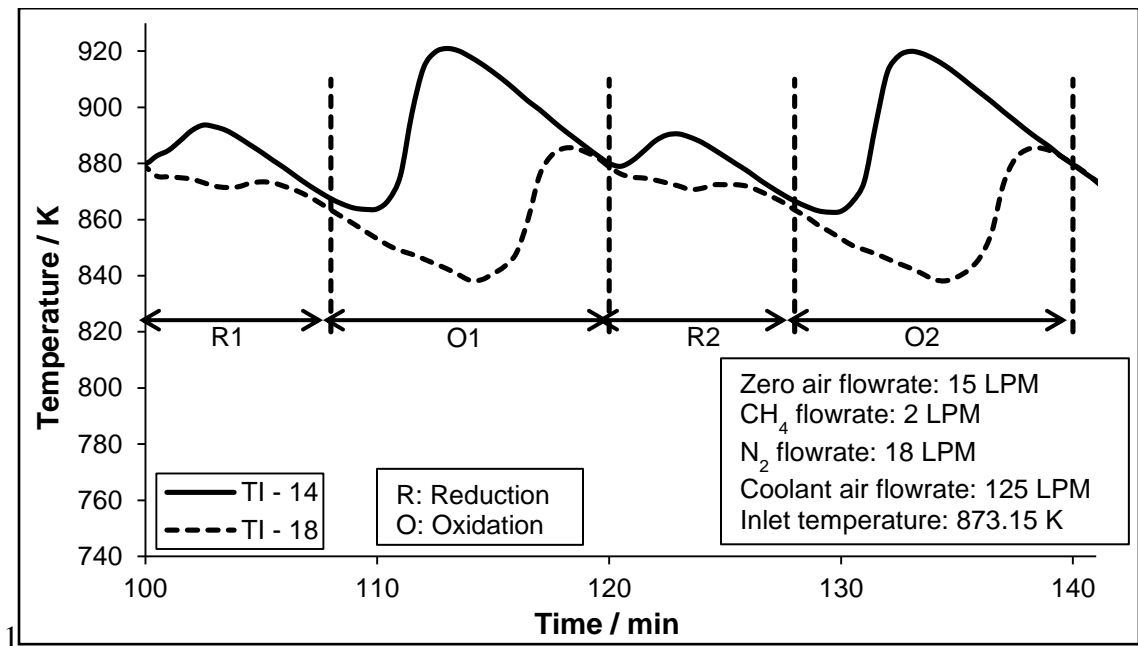
Fig. 7.9 Variation of bed temperature with time at two axial locations (at $z = 0.42$ m and $z = 0.58$ m from top and at $r = 18$ mm from outer wall) at "cyclic" steady state for run 1

Similar trends were obtained for run 2 and the same is presented in Fig. 7.10 and 7.11 with reduction temperature rise almost negligible due to a higher coolant flowrate.
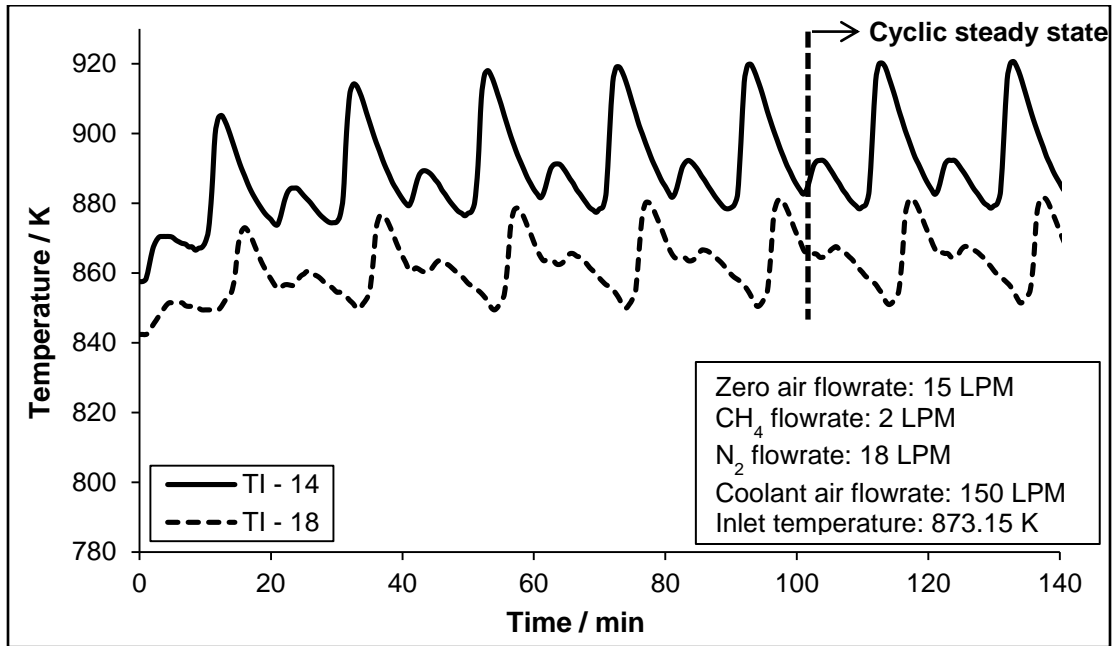
Fig. 7.10 Variation of bed temperature with time at two axial locations (at $z = 0.42$ m and $z = 0.58$ m from the top and at $r = 18$ mm from outer wall) for run 2
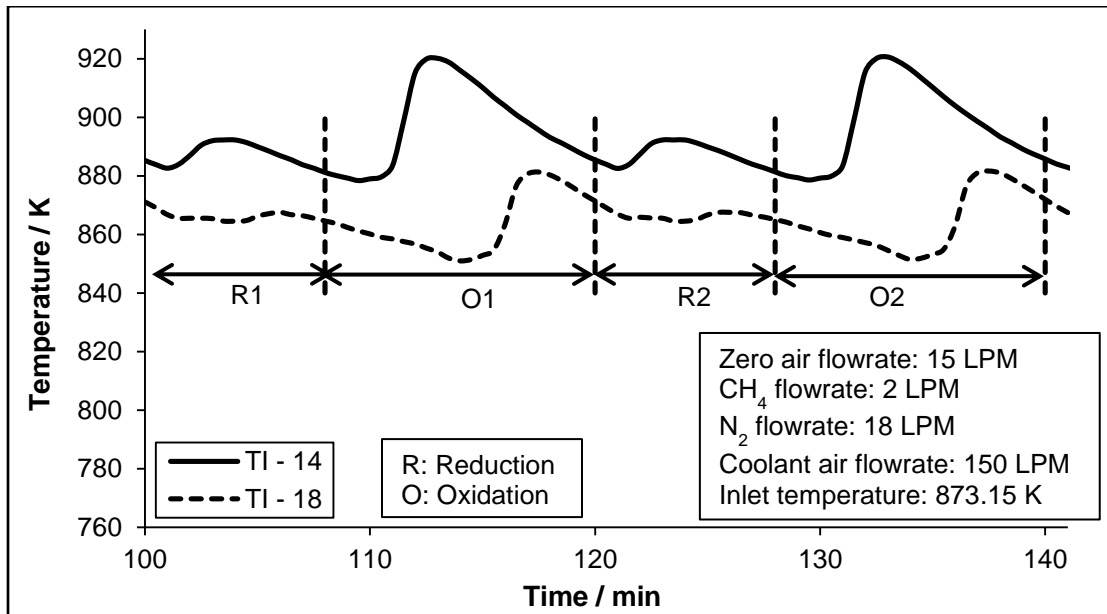
Fig. 7.11 Variation of bed temperature with time at two axial locations (at $z = 0.42$ m and $z = 0.58$ m from top and at $r = 18$ mm from outer wall) at "cyclic" steady state for run 2

In addition, the effect of relevant operating parameters was investigated and the same is presented in this section. For a change in a specific parameter, all other operating conditions were maintained the same as those in run 1. The measured temperature profiles at two radial and two axial locations for flowrates of 15 LPM zero air, 2 LPM methane, 125 / 150 LPM coolant and inlet temperature of 873.15 K have been presented and discussed in previous section (Fig. 7.1, 7.3, 7.8 and 7.10). Similar profiles were obtained for all other parameters presented in this section. The profiles for the extreme cases (zero air flowrates of 5 LPM and 20 LPM, methane flowrates of 4 and 6 LPM, coolant flowrates of 100 and 175 LPM and inlet temperature of 893.15 K) have been included in Appendix G.

7.1.2.1 Effect of zero air flowrate

The percentage of radial transfer from the OSRM bed for different zero air flowrates ranging between 5 and 20 LPM is presented in Table 7.2. With the oxygen concentration constant at 21%, an increase in flowrate results in an increase in the number of moles of oxygen available. At higher flowrates (> 15 LPM), the reaction and hence the amount of energy generated is limited by the amount of solid available in the bed.

Table 7.2

Effect of zero air flowrate on radial heat transfer

Zero air flowrate (LPM)	Radial heat transfer (%)	External power supply (%)
5	53 ± 1	48
10	81 ± 2	42
15	86 ± 2	32
20	87 ± 2	41

At these flowrates, a larger fraction of this energy generated during the oxidation reaction

is transferred in the axial direction due to convective flow of gas over the reacted portion of the bed which results in cooling of the bed. This in turn reduces the temperature difference between the bed and coolant, thereby limiting the radial heat transfer. The decrease in bed temperature is compensated by external power supply which in turn increases the temperature and sustains the radial heat transfer. As seen in Table 7.2, the percentage of radial heat transfer in the case of 20 LPM is same as that at 15 LPM within experimental uncertainties. However the external power supply contributes to 41% of the total energy in the bed at 20 LPM as compared to 32% at 15 LPM. Any further increase in flowrate would result in a decrease in bed temperature to a level where combustion becomes unsustainable. In the case of 5 and 10 LPM, the external heating contributed to 48% and 42% of the total energy in the bed. A decrease in flowrate results in a decrease in the number of moles of oxygen available which in turn limits the reaction and results in incomplete oxidation of the bed. In subsequent reduction cycles, the convective flow of methane and nitrogen results in cooling of an already partially reduced bed, thereby decreasing the temperature difference required for radial transfer. This in turn is compensated for by external heating. For a cycle time of 12 minutes, at these relatively lower flowrates no slip of oxygen in the outlet gas stream was detected, confirming that the oxidation reaction was not complete.

7.1.2.2 Effect of methane flowrate

Apart from 2 LPM, the effect of increased methane flowrate on the radial heat transfer was investigated at 4 and 6 LPM. With nitrogen as a diluent, this corresponded to varying methane concentrations of 20% and 30% respectively. The total flowrate of methane and nitrogen was maintained at 20 LPM in all the runs. Table 7.3 shows the total radial heat transfer at these flowrates for a reduction cycle time of 8 min.

At 4 LPM, the bed temperature decreases due to convective flow of gas and external power supply contribution increased overall to 38%. The percentage of heat transfer under these conditions however remains unchanged as it is sustained by the external power source. Test runs were then carried out at 6 LPM. However the bed temperature

was found to decrease significantly enough to inhibit the oxidation reaction in the next cycle. The experiment at 6 LPM was repeated by reducing the reduction cycle time to 5 minutes, wherein it was possible to maintain the bed temperature with a decreased external power contribution of 32%, which was same as that for 2 LPM. The radial transfer however, was restricted to 69%. This can be attributed to convective cooling in the axial direction at 6 LPM wherein the number of moles of methane are in excess of that required for reaction. In addition the higher specific heat of methane as compared to that of nitrogen compensated for the decrease in nitrogen flowrate. The radial heat transfer was thus maximized at 2 LPM.

Table 7.3

Effect of methane flowrate (i.e. concentration) on radial heat transfer

Methane flowrate (LPM)	Nitrogen flowrate (LPM)	Radial heat transfer (%)	External power supply (%)
2	18	86 ± 2	32
4	16	87 ± 2	38
6*	14	69 ± 2	32

* Cycle time changed

7.1.2.3 Effect of coolant flowrate

Apart from carrying out runs at 125 LPM reported earlier, the effect of varying coolant flowrates of 100, 150 and 175 LPM on radial heat transfer is shown in Table 7.4.

Table 7.4

Effect of coolant flowrate on radial heat transfer

Coolant flowrate (LPM)	Radial heat transfer (%)	External power supply (%)
100	78 ± 2	20
150	95 ± 2	35
175	93 ± 2	41

At 100 LPM, the coolant flowrate was insufficient to maximize radial heat transfer which

was limited to 78%. With an increase in flowrate, the heat transfer was found to increase and as high as 95 % of the energy in the bed was transferred at 150 LPM. The external supply in this case contributed to 35% overall and 7% under "cyclic" steady state conditions. At 175 LPM, though the heat transfer was 93%, the bed temperature was found to decrease as was indicated by the overall increase in external power supply contribution to 41%. This can be attributed to the lower temperature difference between the bed and coolant at this high flowrate which limits the radial heat transfer.

7.1.2.4 Effect of reactive gas inlet temperature

The effect of three different reactive gas inlet temperatures on radial heat transfer is presented in Table 7.5.

Table 7.5

Effect of reactive gas inlet temperature on radial heat transfer

Reactive gas inlet temperature (K)	Radial heat transfer (%)	% of External power supply
873.15	86 ± 2	32
898.15	85 ± 2	35
923.15	91 ± 3	40

With an increase in inlet temperature, the reaction rate increases resulting in a rise in OSRM bed temperature. This in turn increases the temperature difference between the bed and coolant thereby felicitating increased radial heat transfer which is 91% at 923.15 K. However the overall external power supply contribution in this case increases to 40% as against 32% at 873.15 K. This can be attributed to the fact the OSRM bed gets saturated prior to completion of respective cycle times because of the higher reaction rate at 923.15 K as a result of which convective cooling takes place until cycle switchover occurs. The combined cooling effect due to radial and axial convective heat transfer is subsequently compensated for by the external power supply. The heat transfer is maximized at 873.15 K under sustained combustion conditions.

7.2 Kinetic study of oxidation and reduction of Cu based OSRM

As mentioned in the section 5.2, the experiments were carried out to determine the kinetics of oxidation and reduction of Cu and CuO respectively using a Pulsed Micro-reactor (PMR) technique. In this section, the results of preliminary experiments followed by those of oxidation and reduction test runs are discussed in detail.

7.2.1 Preliminary experiment

7.2.1.1 Confirmation of plug flow using RTD study

Experiments were performed to confirm plug flow conditions in the PMR. These experiments were conducted in the range of temperatures and flowrates of interest in the main test runs shown in Table 5.3. Representative results for Dispersion number (*Di*) using zero air and CH_4 at a temperature of 873.15 K and flowrate of 35 SCCM is shown in Table 7.6 with 95% confidence interval. In both cases, the reactant concentration was obtained from chromatogram data of product gases based on retention time. This data was then used to calculate *Di* using the procedure mentioned in Appendix H. The concentration vs time data for representative oxidation and reduction runs has been provided in the Appendix I.

Table 7.6

Representative results of RTD study

Tracer	Dispersion no. (*Di*) $\times 10^3$	*(95% Confidence Interval) $\times 10^3$
Oxygen	0.694	[0.664 – 0.726]
Methane	0.079	[0.072 – 0.087]

* t-value based confidence interval

In the entire range of flowrates of 30 – 40 SCCM and temperatures of 673.15 – 1073.15 K covered as part of this study for oxygen and methane, the value of *Di* was found not to

exceed 0.00073 confirming plug flow conditions at all times in the reactor during the main test runs and that the effect of wall slip if any, was insignificant.

7.2.2   Estimation of kinetic parameters

Prior to estimating kinetic parameters, typical chromatograms for a single pulse of 0.5 cc zero air (21 mol% O_2) and 0.1 cc CH_4 (99.5%) were obtained as shown in Fig. 7.12 and Fig. 7.13 respectively by injecting related gases through the reactor at room temperature under 'no reaction' conditions. The chromatogram areas in both cases correspond to the exit of more than 99% of O_2 and CH_4 injected. No significant integration errors were observed as is indicated by the final results obtained. These chromatograms were then used as references in further studies.
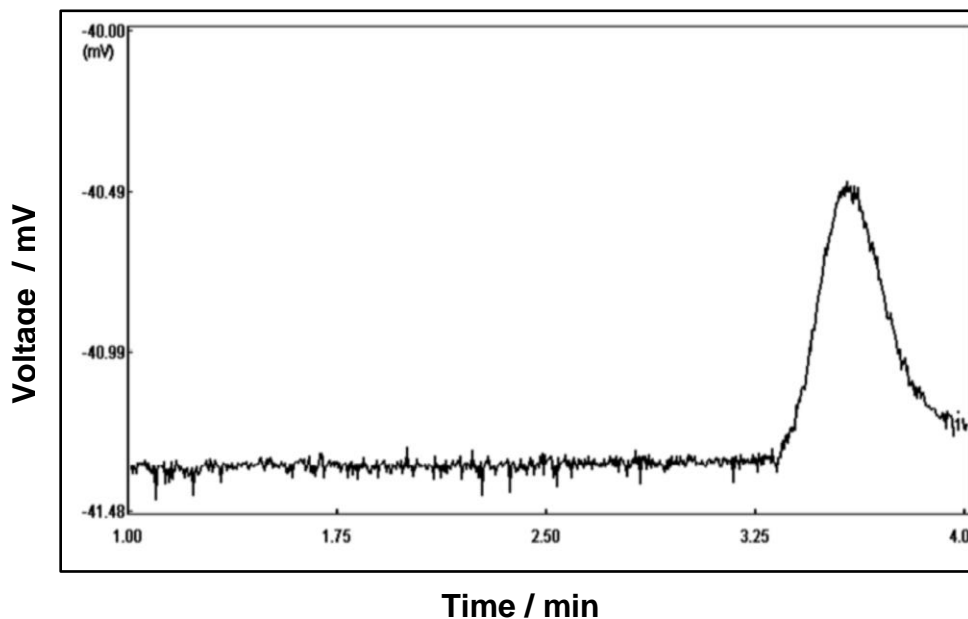
Fig. 7.12 Gas chromatogram indicating O_2 peak for 0.5 cc zero air

For oxidation and reduction of Cu based OSRM, Garcia – Labiano et. al. [23, 70] have reported surface reaction as the rate limiting step and that pore diffusion and external mass-transfer resistances can be neglected. Both reactions were therefore initially assumed to be surface reaction controlled in the present study.
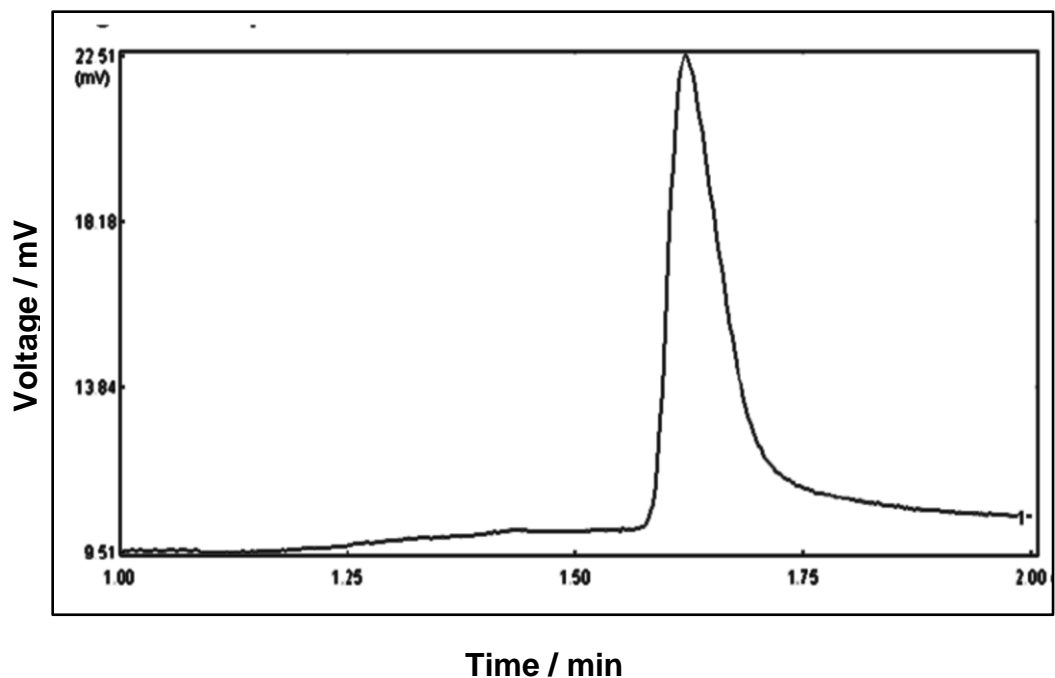
Fig. 7.13 Gas chromatogram indicating methane peak for 0.1 cc CH_4

7.2.2.1 Oxidation

Fig. 7.14 shows the relative magnitudes of peaks for O_2 resulting from injection of 10 continuous pulses of zero air at 873.15 K. No peak was observed for the first 6 pulses during which O_2 reacts with Cu to form CuO as given below

$4Cu + O_2 \rightarrow 4CuO$
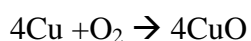
With less solid being available for reaction with every subsequent injected pulse, an O_2 break-through was observed at the outlet of the reactor as indicated by peaks 7 to 9. No further change in peak height was observed with injected O_2 passing through a completely saturated bed unreacted. The peak height of O_2 corresponding to the 10th pulse was found to match that of the reference peak shown in Fig. 7.12.

The analysis was continued for 30 minutes prior to injection of the next pulse during which only carrier gas was passed through the reactor. Neither an additional peak nor a

shift in baseline was observed confirming that the solid did not undergo any transformation during this period and oxygen un-coupling from the bed did not take place.
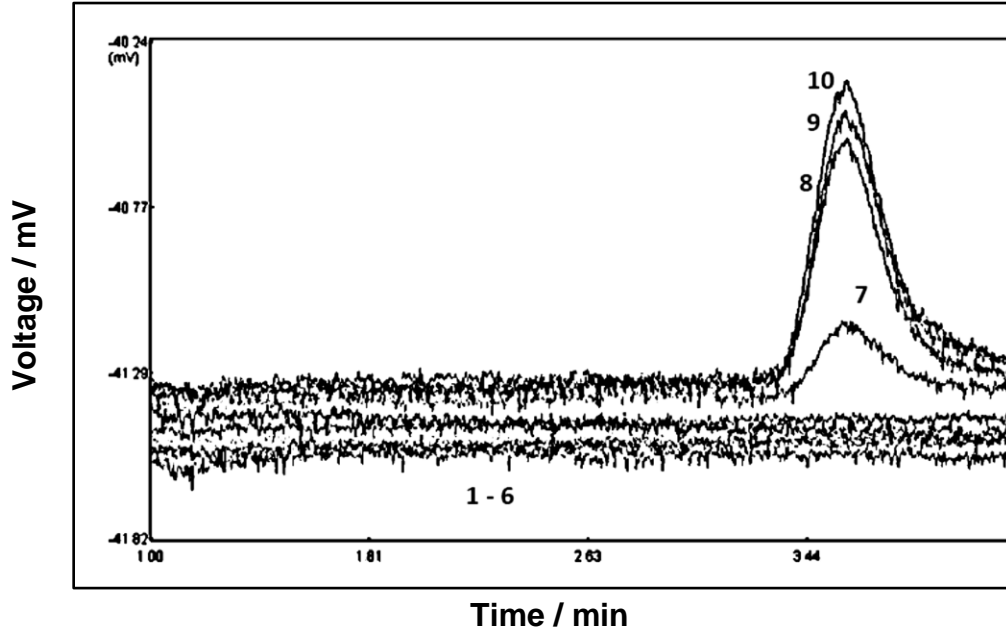
Fig. 7.14 Chromatogram peaks for O_2 from each pulse

The fraction of unconverted solid and gaseous reactant was estimated from the chromatogram data in Fig. 7.14, thus

$$\frac{c_{si}}{c_{so}} = 1 - i\frac{S_o}{S_T} + \frac{\sum_{i=1}^{i} S_i}{S_T} \tag{7.1}$$

$$\frac{c_{gi}}{c_{go,N}} = 1 - \frac{i}{N} + \frac{\sum_{i=1}^{i} S_i}{NS_o} \tag{7.2}$$

where S_o and S_i correspond to the areas of the reference gas peak and that for i^{th} pulse respectively. S_T represents the total amount of gas reacted in N pulses and was calculated using

$$S_\text{T} = \sum_{i=1}^{N}(S_\text{o} - S_i) \tag{7.3}$$

Adopting the methodology discussed in section 6.2, reasonably good linear fits were obtained for $m = 0.1$ and $n = 1$ with R^2 values greater than 0.99 in both cases. Representative results at two extremes of temperatures in which the test runs are carried out are shown in Fig. 7.15 (for m) and Fig. 7.16 (for n) and the corresponding data is given in Appendix J. The procedure was repeated at 9 different temperatures in the temperature range of $673.15 – 873.15$ K. The corresponding plots yielded straight line fits in all cases confirming reaction orders of 0.1 and 1 with respect to Cu and O_2 respectively. The slope of the line in each of the plots was used to estimate k''_1 at these temperatures (using equation (6.22)). Data points beyond 95% conversion were neglected due to uncertainty associated with acquiring accurate values of fraction of unreacted reactants as the reaction goes to completion.
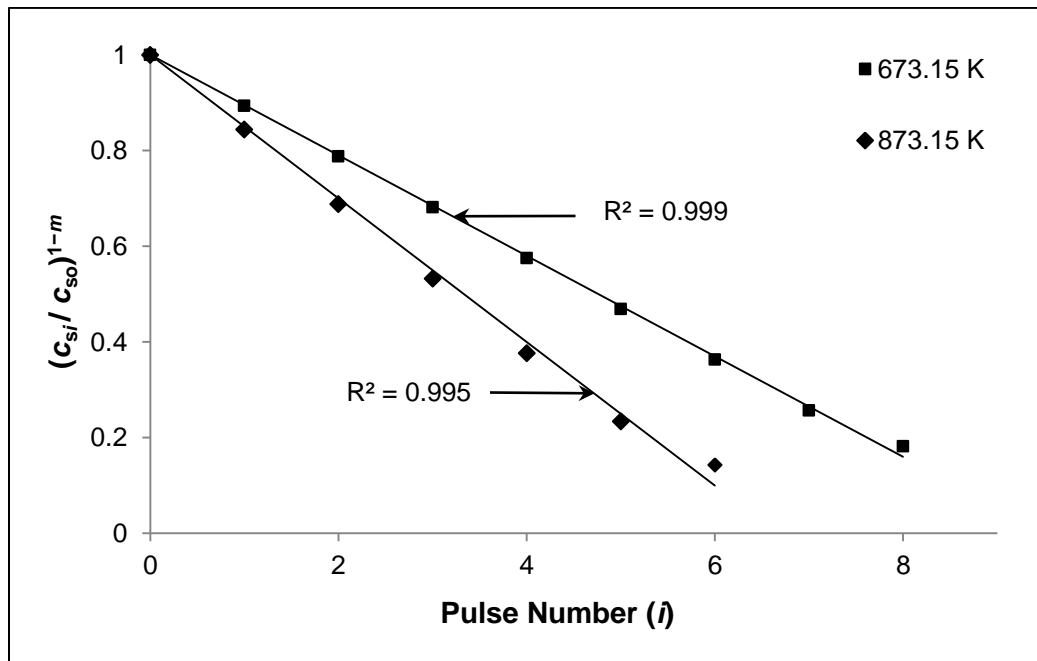
Fig. 7.15 $(c_{si}/c_{so})^{1-m}$ vs i for oxidation (for $m = 0.1$)
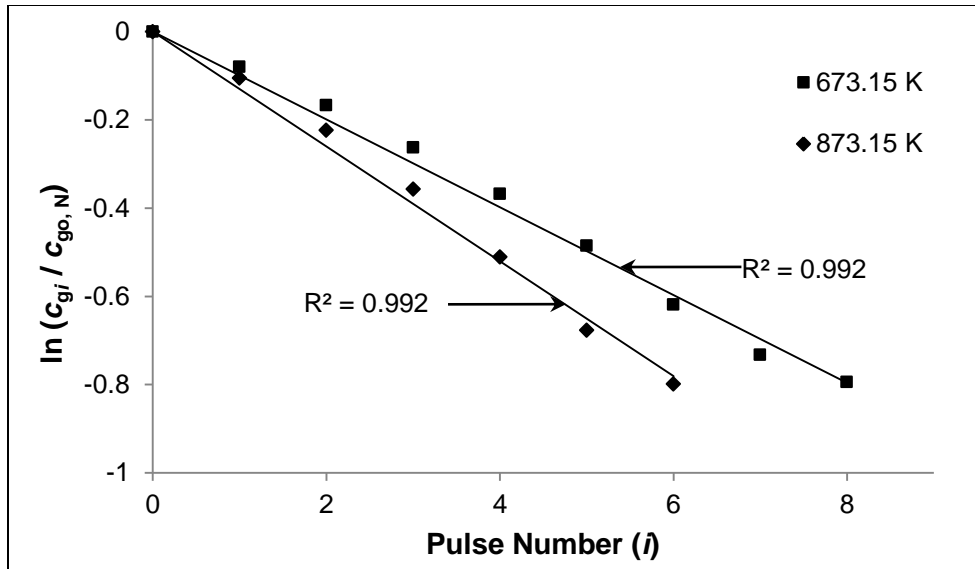
Fig. 7.16 $\ln\left(c_{gi}/c_{go,N}\right)$ vs i for oxidation (for $n = 1$)

By linearly fitting an Arrhenius plot corresponding to $\ln k''_1$ vs. $1/T$ data (see Fig. 7.17 and Appendix J), the values of kinetic parameters k''_o and E were obtained for oxidation as $(4.20 \pm 0.05) \times 10^{-6}$ m/s and 15.32 ± 0.43 kJ/mol respectively. These values are found to be in excellent agreement with those estimated by Garcia – Labiano et.al. [23] using a TGA (see Table 7.7).
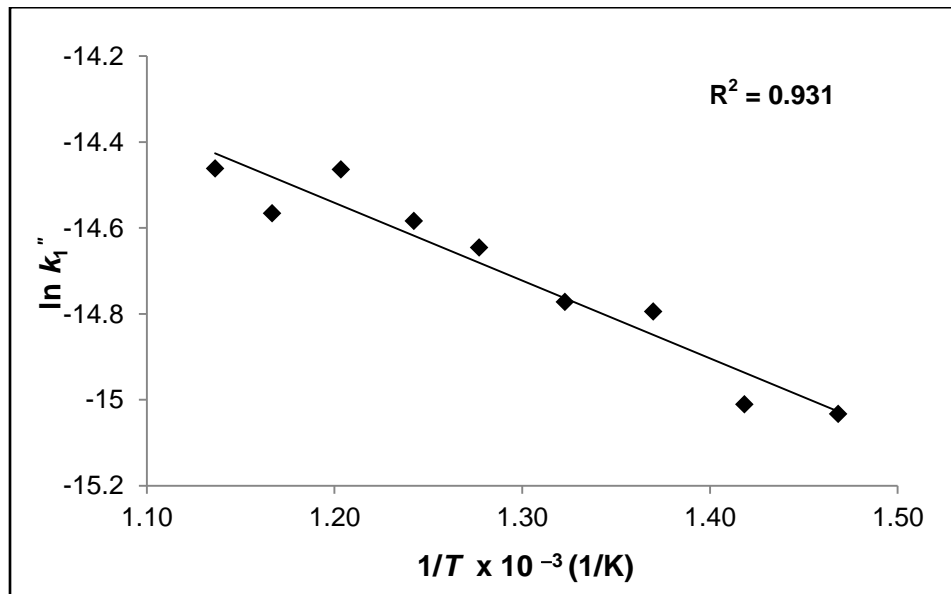
Fig. 7.17 Temperature dependence of oxidation rate constant

The analysis of product gases of reduction of CuO at 873.15 K for 9 continuous pulses of CH_4 is shown in Fig. 7.18. No peak was observed for the first 3 pulses during which CH_4 reacts with CuO to form CO_2 and water as given below:

$$4CuO + CH_4 \rightarrow 4\ Cu + CO_2 + H_2O$$
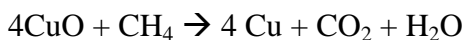
CH_4 break through was subsequently observed from the 4th pulse with increasing amount of unreacted methane exiting the reactor (corresponding to pulse injection nos. 4 to 8).
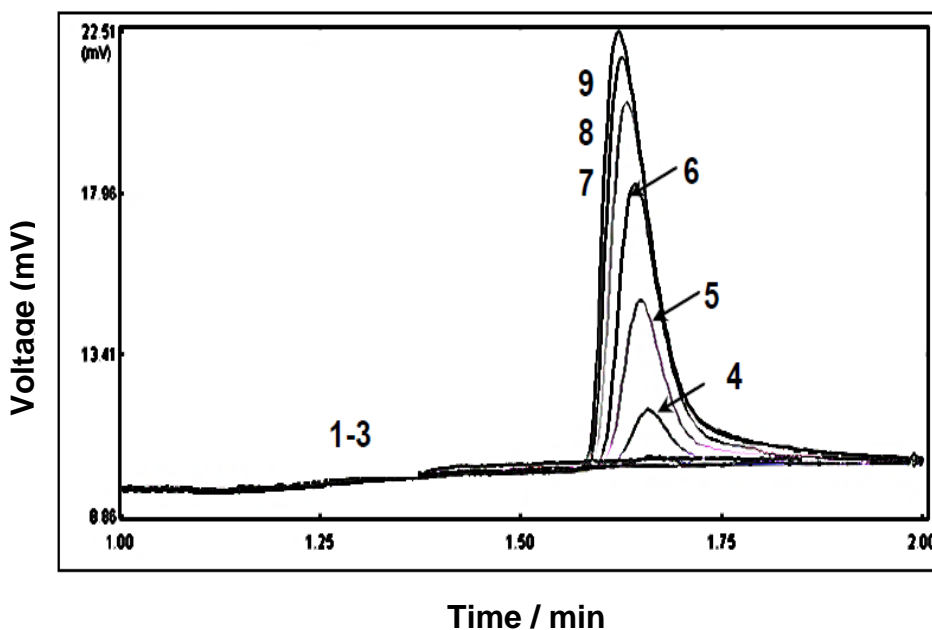
Fig. 7.18 Chromatogram peaks for CH_4 from each pulse

With no further change in peak height and no CO_2 observed at the exit after the 8th pulse, it was concluded that the bed had been completely reduced back to Cu. The peak height of CH_4 corresponding to the 9th pulse was found to match that of the reference peak shown in Fig. 7.13.

As in the case of oxidation, the areas of corresponding peaks were used to determine (c_{si}/c_{so}) and $(c_{gi}/c_{go,N})$. The methodology discussed in section 6.2 was then adopted to determine reaction orders. No linear plot was however obtained for assumed values of m ranging from 0.1 to 2. It was concluded that for the given amount of OSRM, i.e. 100 mg, the number of data points obtained was not sufficient to determine the order with respect to solid reactant. This can attributed to the larger conversion of solid per pulse injected in the case of reduction as compared to the conversion per pulse in the case of oxidation. It was expected that reducing the sample volume or increasing the quantity of OSRM would help address this issue. It was decided to subsequently increase the OSRM amount to 400 mg, after which the entire set of experiments was repeated. A reasonably good linear fit with R^2 values greater than 0.99 was now obtained for $m = 0$ and $n = 0.4$ as shown in Fig. 7.19 and Fig. 7.20 at two representative extremes of temperatures and the corresponding data is given in Appendix J. As in oxidation, data points beyond 95% conversion were neglected. Similar straight line fits were obtained when the procedure was repeated at five different temperatures in the range $873.15 - 973.15$ K. This confirmed reaction orders of 0 and 0.4 for reduction with respect to CuO and CH_4 respectively which are in good agreement with those reported in literature [23].
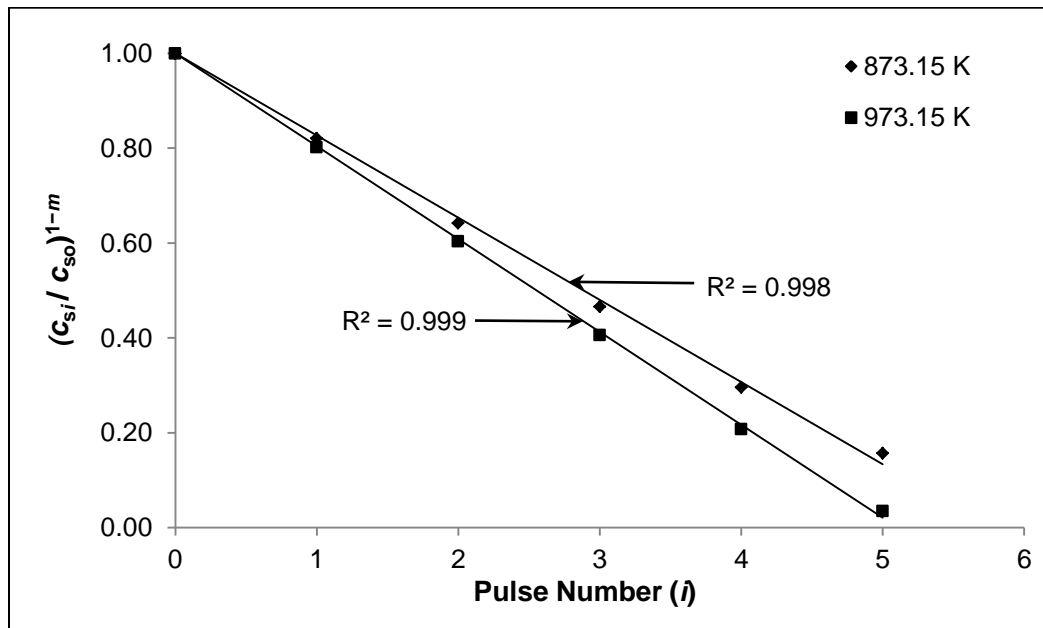
Fig. 7.19 $(c_{si}/c_{so})^{1-m}$ vs i for reduction (for $m = 0$)

The kinetic parameters k''_o and E values using the Arrhenius plot (see Fig. 7.21) were obtained as $(1.28 \pm 0.12) \times 10^{-4}$ $mol^{0.6}/m^{0.8}$.s and 58 ± 3.5 kJ/mol respectively. The data of $\ln k''_1$ vs. $1/T$ is provided in Appendix J. The value of activation energy is in close agreement to that obtained by Garcia – Labiano et. al. [23] i.e. 60 ± 3 kJ/mol. The value of k''_o obtained in the present study is however lower than that reported by Garcia – Labiano et. al. (see Table 7.7). This can be attributed to the use of 30 % steam in the feed by Garcia – Labiano et. al. at all temperatures during reduction to avoid coke formation which facilitated exposing the entire coke free solid surface to CH_4 at all times. No steam was used in the present study. Coke formation was observed in the present runs only when reduction experiments were performed at temperatures above 973.15 K.
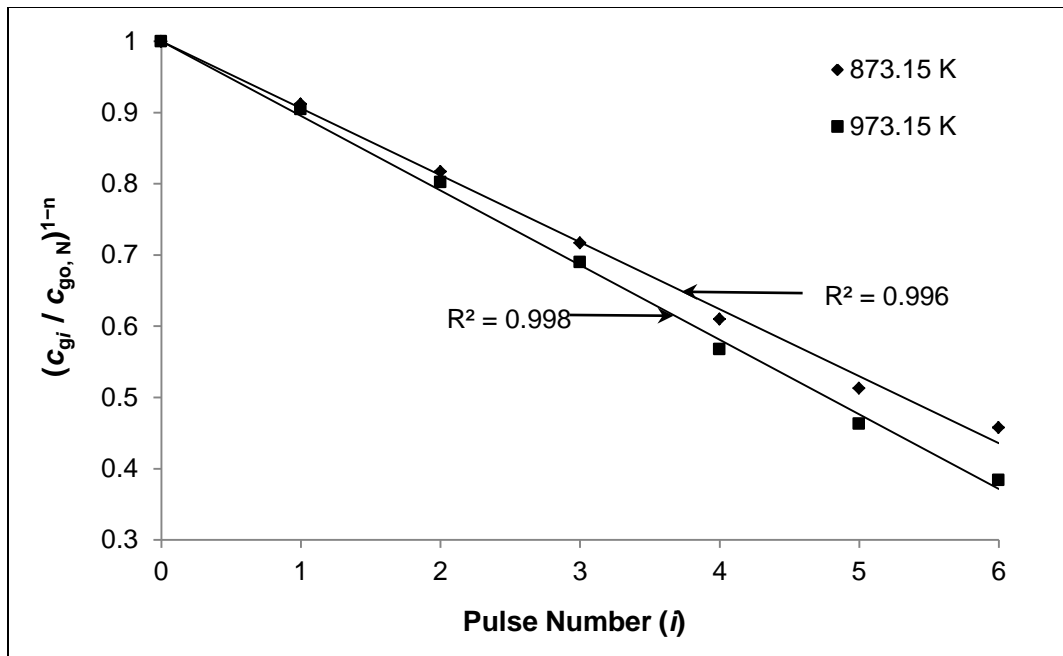
Fig. 7.20 $(c_{gi}/c_{go,N})^{1-n}$ vs i for reduction (for $n = 0.4$)
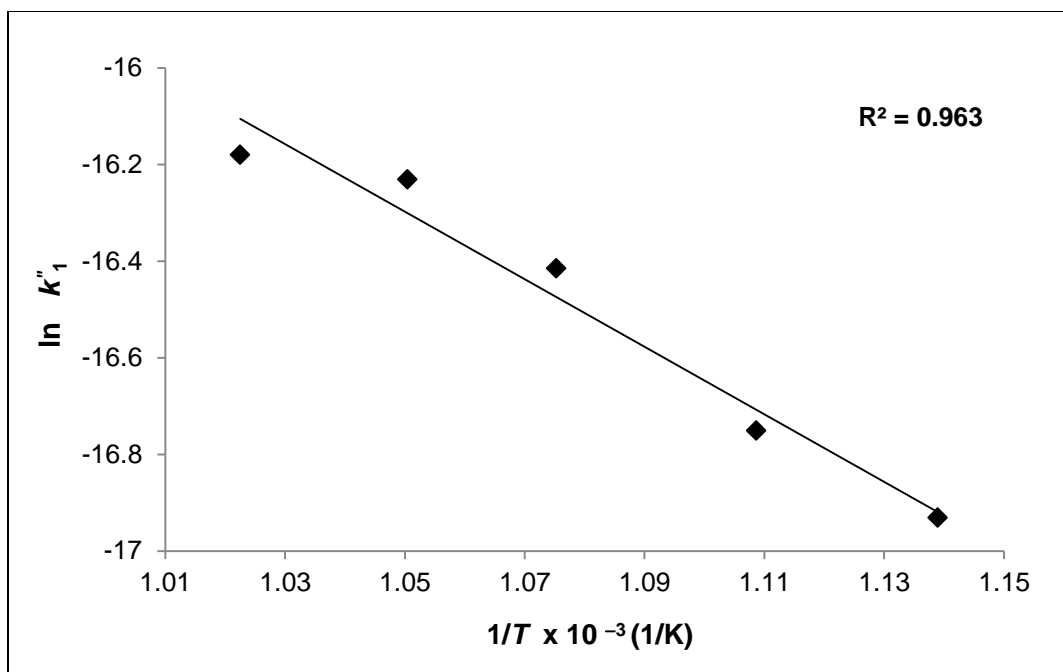
Fig. 7.21 Temperature dependence of reduction rate constant

Table 7.7

Comparison of results for kinetic parameters with literature

		Order	Pre-exponential factor	Activation
		(m, n)	(k''_o)	Energy (E)
			$(mol^{1-m-n}\, m^{3m+3n-2}\, s^{-1})$	(kJ/mol)
Oxidation of Cu	Present study	(0.1, 1.0)	$(4.20 \pm 0.05) \times 10^{-6}$	15.32 ± 0.43
	Literature[23]	(**, 1.0)	$4.7 \times 10^{-6}*$	15*
Reduction of	Present study	(0, 0.4)	$(1.28 \pm 0.12) \times 10^{-4}$	58 ± 3.5
CuO	Literature[23]	(**, 0.4)	$4.5 \times 10^{-4}*$	60 ± 3

*uncertainty not reported   ** not reported

7.2.3   Influence of external mass transfer and pore diffusion

For both reactions, the left hand side of equation (6.24) results in values of $0.143n$ and $0.0048n$ respectively. External mass transfer effects can subsequently be neglected for

n < 1.05 (oxidation) and *n* < 31 (reduction). The present investigation using the PMR confirms reaction orders of 1 and 0.4 for oxidation and reduction respectively. For these reaction orders, the largest estimated values of Mears' parameter and C_{WP} (using equations 6.24 and 6.26) in the range of temperatures in which the experiments were carried out as presented in Table 7.8 are less than 0.15 and 1 respectively indicating that both external mass transfer and pore diffusion effects can be neglected as explained in section 6.2.1.

Table 7.8

Estimated values of important parameters

Parameter	Oxidation	Reduction
External mass transfer coefficient (k_c in m/s)	0.423 ± 0.032	0.201 ± 0.005
Mears' parameter (eq. (6.24))	0.143 ± 0.001	0.0024 ± 0.0002
Weisz - Prater parameter (eq. (6.26))	0.48 ± 0.026	0.035 ± 0.0029

While the value of C_{WP} < 1 for oxidation, it is comparatively higher as compared to that in reduction. Unlike reduction which seems to be kinetically limited, there is a possibility that this reaction may be controlled by some form of pore transport limitation although this effect may not be significant. The effect of pore diffusion was also investigated by reducing the particle size which was expected to increase the surface area and hence the reaction rate. The OSRM particles were crushed to an average particle size of 0.7 mm. The value of BET surface area was 215.3 m^2/g, which is not very different from the value reported in Table 5.1 for uncrushed particles.

So prima facie, the oxidation reaction seems to be kinetically controlled with the effect of pore diffusion being minimal or just about starting to play a role. In this regime, the kinetic parameters obtained are in good agreement with those reported in literature [23] validating the use of the PMR technique to study non-catalytic gas-solid reactions.

It is interesting to note that the Mears' parameter value for oxidation is closer to 0.15 as compared to that of reduction. This can be attributed to relatively higher reaction rate for

oxidation compared to reduction. It is therefore important that while collecting rate law data using a PMR system, the gas flowrate is so chosen that the reaction is not mass transfer limited and allows for sufficient number of pulses to be injected so as to obtain accurate information on the kinetics of the reaction.

While the proposed uniform reaction based methodology has been validated using surface reaction controlled systems, it can be extended to pore diffusion limited reactions. The PMR data obtained can also be used in conjunction with other particle reaction models established in literature if external or internal transport limitations are significant. A suitable methodology to interpret the data needs to be accordingly developed.

7.3   Engineering implications

The present study in addition to demonstrating the potential of UMC for heat transfer applications also brought out a few important implications which could impact design and operation of UMC reactor systems. Large scale application of UMC will be contingent upon the choice of a suitable OSRM. The use of Cu/CuO system as an OSRM is favorable from a point of view that both oxidation and reduction are exothermic reactions. This material was found to be stable and reactive for 150 cycles of oxidation and reduction.

In the study on reaction kinetics using a PMR involving Cu based OSRM, at higher temperatures (> 973.15 K), the presence of CO was detected at the reactor outlet during reduction. This can be attributed to possible oxidative conversion of methane at higher concentrations to form higher carbon number products in the presence of a metal oxide [71]. The reaction mechanism involves oxidation of methane to methyl radicals and water. The methyl radicals subsequently form higher hydrocarbon products through a series of thermal reactions, which then degrade to form non-selective products like coke and carbon-di-oxide. Coke induced degradation of performance of the PMR needs to be investigated further. The formation of coke can be avoided by the use of steam, which would however introduce an economic penalty at a large scale. At temperatures above

1073.15 K, the reactor material (SS) was found to oxidize imposing constraints on the Material of Construction (MOC) of the UMC reactor.

The use of Cu/CuO is also limited by its comparatively low melting point which can result in fusing and hardening of the metal at high temperatures (> 1300 K) caused by local hot spots in the bed.

While Cu/CuO with its exothermic reactions systems is a favorable OSRM, its use in UMC reactors may be limited to temperatures below 973.15 K. The above arguments will therefore place a large demand on researchers to continuously look for newer alternatives to Cu/CuO as an OSRM for high temperature applications and also address challenges of oxidation associated with the commonly used MOC at these temperatures. The solutions to the above problems will be key drivers to the success of UMC applications in the near future.

Chapter 8

Modeling and Simulation of UMC based PBR with Heat Transfer

A mathematical model for a proposed UMC based Packed Bed Reactor (PBR) integrated with heat transfer to a coolant system has been developed. For prescribed inlet conditions of reactive gas and coolant temperatures and flowrates, the model predicts the temperature along the bed and the total heat transfer rate.

8.1   Outline of a model

A 2-D model was developed for an annular UMC based PBR wherein the annular region corresponds to the packed bed section consisting of the OSRM and inert particles and the inner pipe represents the coolant flow section. Counter current flow arrangement of reactive gas and coolant was considered. The reactions involved in this system are non-catalytic gas-solid reactions with solid as the limiting reactant. Fig. 8.1 depicts a schematic view of the physical model.

Based on the arguments presented in literature section 2.5, a pseudo-homogeneous model was chosen for the PBR section assuming the solid surface to be completely exposed to bulk fluid conditions and considering volume of only the fluid phase. Transient modeling equations were framed based on species mass and energy balance, neglecting momentum variation (i.e. constant velocity) and incorporating the reaction rate and enthalpy in respective source terms. These source terms were considered only for the OSRM in packed bed section and for a time frame in which solid reactant gets completely converted. This constraint was incorporated into the model using reaction and heat front velocities, which were estimated using expressions developed by Noorman et. al. [13, 14]. Global kinetics with surface reaction as rate limiting step was adopted and rate expressions in the form of a power law were used for respective reactions. The effective
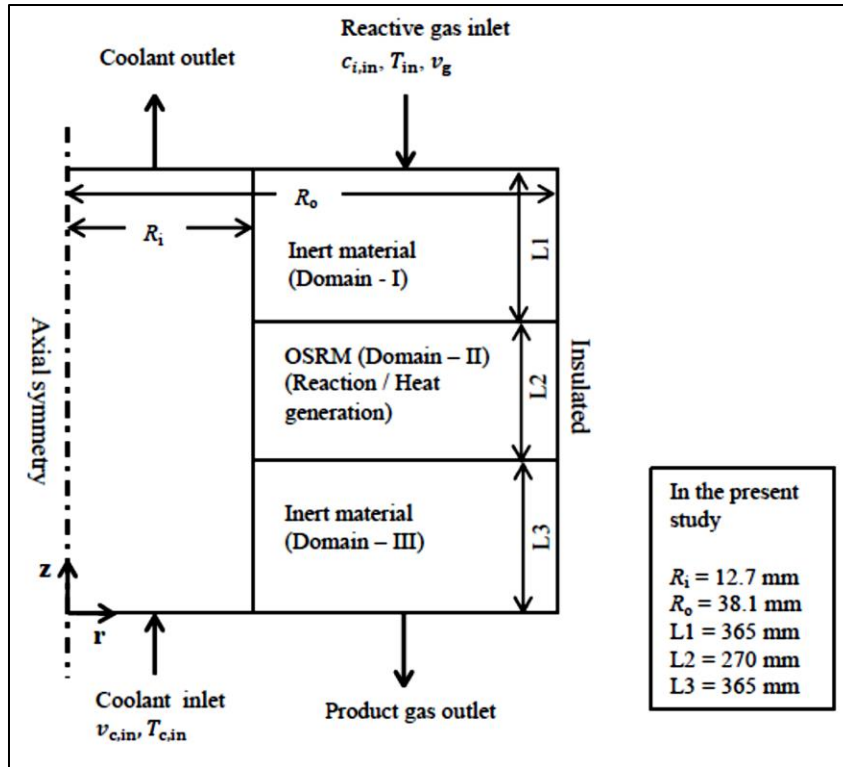
Fig. 8.1 Schematic view of physical model

mass dispersion coefficient and thermal conductivity were used in the diffusion and conduction terms respectively and these parameters were estimated using suitable empirical correlations proposed by Kulkarni and Doraiswamy [50]. Thermal insulation at the outer wall and no mass transfer conditions at the inner and outer walls of the reactor were considered. Standard Dirichlet inlet boundary conditions for temperatures and concentrations were used.

Coolant flow through the inner pipe was modeled using the momentum and energy balance for turbulent flow under transient conditions. The velocity profiles, obtained by solving the momentum balance equation based on a $k - \epsilon$ turbulence model, were used in conjunction with the energy balance to predict temperature profiles within the pipe. In this case as well, standard Dirichlet inlet conditions were used.

The energy balance based heat transfer models of the PBR and coolant flow sections

were coupled using a convective heat transfer boundary condition across the interface (i.e. at inner pipe surface). The modeling equations were solved independently for oxidation and reduction.

The details of modeling equations, kinetic scheme and related initial and boundary conditions are given in the next section. Commercial CFD software COMSOL Multiphysics 5.1^{TM} was used for model implementation and simulation, details of which are presented in section 8.3.

For simulation purposes, an annular reactor of 1 m length with an outer diameter of 3" (76.2 mm) and inner diameter of 1" (25.4 mm) was considered. 13 wt% Cu / CuO supported on alumina was used as a representative OSRM. Zero air and a mixture of CH_4 and N_2 were used as reactive gases for oxidation and reduction respectively. The simulation time considered was fixed at 12 min for oxidation and 8 min for reduction based on experimental determination of respective reaction cycle times presented in section 5.1. The reactions considered in this study are

(A) Oxidation of Cu $\qquad$ $4Cu + 2O_2 \rightarrow 4CuO$

(B) Reduction of CuO $\qquad$ $CH_4 + 4CuO \rightarrow 4Cu + CO_2 + 2H_2O$
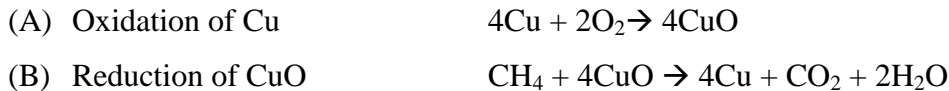
8.2   Modeling equations

8.2.1   Packed bed section

Assumptions:

1. Negligible intra-particle concentration and temperature gradients
2. All gases are ideal
3. Constant bed void fraction and uniform particle size
4. Radial convection, axial dispersion and conduction are neglected.
5. Constant velocity of the reactant in the z-direction (i.e. v_z = constant)

Governing equations:

Species mass balance equation:

$$\varepsilon_g \frac{\partial c_g}{\partial t} + v_g \frac{\partial c_g}{\partial z} - D_{er}\left[\frac{\partial^2 c_g}{\partial r^2} + \frac{1}{r}\frac{\partial c_g}{\partial r}\right] = -r_g \varepsilon_g \tag{8.1}$$

Energy equation:

$$(\varepsilon_g \rho_g C_{pg} + (1 - \varepsilon_g)\rho_s C_{ps})\frac{\partial T_b}{\partial t} + v_g \rho_g C_{pg}\frac{\partial T_b}{\partial z} - \lambda_{er}\left[\frac{\partial^2 T_b}{\partial r^2} + \frac{1}{r}\frac{\partial T_b}{\partial r}\right] = -\varepsilon_g(\Delta H_{rx})(M_g)(r_g) \tag{8.2}$$

Initial / boundary conditions

At $t = 0$ (for all z and r) $c_g = c_{go}$; $T_b = T_{bo}$ $\qquad$ (8.3a, 8.3b)

At $z = 0$ (for $t > 0$) $\qquad$ $c_g = c_{g,in}$; $T_b = T_{b,in}$ $\qquad$ (8.4a, 8.4b)

At $r = R_o$ (for all z)

$$\frac{\partial c_g}{\partial r} = 0; \frac{\partial T_b}{\partial r} = 0 \tag{8.5a, 8.5b}$$

At $r = R_i$ (for all z)

$$\frac{\partial c_g}{\partial r} = 0; -\lambda_{er}\frac{\partial T_b}{\partial r} = h_e(T_b - T_c) \tag{8.6a, 8.6b}$$

In equations (8.1) to (8.6), c_g, T_b, r_g, v_g and ΔH_{rx} denote concentration of gaseous reactant, temperature in the packed bed, rate of reaction, velocity of gaseous reactant and heat of reaction respectively. D_{er} and λ_{er} are the radial effective mass dispersion coefficient and thermal conductivity respectively. h_e is the effective convective heat transfer coefficient. These coefficients were estimated using correlations given in Appendix K.

<u>Kinetic scheme</u>

The kinetic expression used for both oxidation and reduction was of form

$$-r_{\mathrm{g}} = k_{\mathrm{e}} c_{\mathrm{s}}^m c_{\mathrm{g}}^n \qquad (8.7a)$$

where the effective rate constant k_{e} was estimated using Arrhenius equation thus,

$$k_{\mathrm{e}} = k_{\mathrm{o}}^{''} S_{\mathrm{a}} \rho_{\mathrm{b}} \exp(-E/\acute{R}T_{\mathrm{b}}) = k_{\mathrm{o}} \exp(-E/\acute{R}T_{\mathrm{b}}) \qquad (8.7b)$$

<u>Constraint</u>

$$\text{If } t < \frac{1 - z - \mathrm{L1}}{w_r} \qquad \text{then} \qquad r_{\mathrm{g}} = 0 \qquad (8.8a)$$

where w_r is reaction front velocity and was calculated using following expression

$$w_r = \frac{v_{\mathrm{g}} \rho_{\mathrm{g}} w_{\mathrm{g},in} M_{\mathrm{s}}}{(1 - \varepsilon_{\mathrm{g}}) \rho_{\mathrm{s}} M_{\mathrm{g}} X (b/a)} \qquad (8.8b)$$

This expression for reaction front velocity indicates that the rate at which the solid reactant in the packed bed gets completely converted when the reactive gas is supplied with a constant desired flow rate. It gives an indication of how fast the reaction front is moving along the axis of the bed.

8.2.2 Coolant section

Governing equations

Continuity equation:

$$\frac{\partial \rho_c}{\partial t} + \frac{1}{r}\frac{\partial}{\partial r}\left(\rho_c r v_{c,r}\right) + \frac{\partial}{\partial z}\left(\rho_c v_{c,z}\right) = 0 \tag{8.9}$$

Momentum equations:

The k-epsilon $(k - \epsilon)$ turbulence model is the most commonly used model in Computational Fluid Dynamics (CFD) to simulate mean flow characteristics under turbulent flow conditions. It is a two transport equation model which gives a general description of turbulence and involves two variables k and ϵ. The first variable k accounts for turbulent kinetic energy in the fluid and the second variable ϵ accounts for the rate of dissipation of the turbulent kinetic energy.

The corresponding modeling equations are

$$\left(\frac{\partial (\rho_c v_c)}{\partial t} + (v_c.\nabla)(\rho_c v_c)\right) = \nabla.\left[-P_c I + (\mu + \mu_T)\left(\nabla v_c + (\nabla v_c)^T\right)\right] \tag{8.10}$$

$$\frac{\partial (\rho_c k)}{\partial t} + (\nabla.\rho_c k v_c) = \nabla.\left(\frac{\mu_T}{\sigma_k}\nabla k\right) + 2\,\mu_T G - \rho_c \epsilon \tag{8.11}$$

$$\frac{\partial (\rho_c \epsilon)}{\partial t} + (\nabla.\rho_c \epsilon v_c) = \left(\nabla.\left(\frac{\mu_T}{\sigma_\epsilon}\nabla \epsilon\right)\right) + C_{1\epsilon}2\frac{\epsilon}{k}\mu_T G - C_{2\epsilon}\rho_c\frac{\epsilon^2}{k} \tag{8.12}$$

where

$$\mu_T = \rho_c C_\mu \frac{k^2}{\epsilon} \tag{8.13}$$

The values of the constants appearing in the above equations were fixed by numerous iterations of data fitting for a wide range of turbulent flows and are as given below.

$C_\mu = 0.09$; $\sigma_k = 1.00$; $\sigma_\epsilon = 1.30$; $C_{1\epsilon} = 1.44$; $C_{2\epsilon} = 1.92$

where μ_T is the turbulent viscosity and is a function of turbulent kinetic energy (k) and dissipation rate (ϵ) and G is the component of rate of deformation.

Energy equation:

$$\rho_c C_{pc} \left(\frac{\partial T_c}{\partial t} + v_c . \nabla T_c \right) - \lambda_c [\nabla^2 T_c] = 0 \tag{8.14}$$

Initial / boundary conditions

At $t = 0$ $\qquad\qquad v_{c,r} = v_{c,z} = 0$; $P_c(g) = 0$; $T_c = T_{co}$ $\qquad$ (8.15a, 8.15b, 8.15c)

At $z = 0$ (for all r) $\quad v_{c,r} = 0$; $v_{c,z} = v_{c,in}$; $T_c = T_{c,in}$ $\qquad$ (8.16a, 8.16b, 8.16c)

At $r = 0$ (for all z) $\quad v_{c,r} = v_{c,z} = $ finite; $T_c = $ finite $\qquad$ (8.17a, 8.17b)

At $r = R_i$ (for all z) $\quad v_{c,r} = v_{c,z} = 0$; $q_c = - h_e(T_b - T_c)$ $\qquad$ (8.18a, 8.18b)

All the physical properties of pure reactive gases and solids were estimated from expressions given in Appendix E. In case of mixtures, average values were calculated based on volume or weight fractions. Coolant (air) properties were estimated as a function of temperature and pressure and the same is also presented in Appendix E.

All parameters used in above equations for both oxidation and reduction are given in Table 8.1. The inlet velocities used for simulation were estimated from respective actual flowrates.

Table 8.1

Simulation parameters

Parameter	Units	Description	Values (Oxidation)	Values (Reduction)
ε_g		Void fraction	0.6	0.6
v_g	m/s	Velocity of gas	0.4	0.5
m		Reaction order (solid)	0 (Cu)	0 (CuO)
n		Reaction order (gas)	1 (O_2)	0.4 (CH_4)
k_o	$mol^{1-n} / m^{3-3n} s$	Pre-exponential factor	1587	171000
E	J/mol	Activation energy	15000	60000
R'	J/mol K	Universal gas constant	8.314	8.314
ΔH_{rx}	kJ/mol	Heat of reaction	-312	-178
M_{O_2}	kg/kmol	Molecular weight of O_2	32	
M_{N_2}	kg/kmol	Molecular weight of N_2	28	28
M_{CH_4}	kg/kmol	Molecular weight of CH_4		16
M_{Cu}	kg/kmol	Molecular weight of Cu	63.5	
M_{CuO}	kg/kmol	Molecular weight of CuO		79.5
c_{go}	mol/m^3	Initial concentration	0 (O_2)	0 (CH_4)
T_{bo}	K	Initial bed temperature	873.15	873.15
$c_{g,in}$	mol/m^3	Inlet reactive gas concentration	4 (O_2)	1.93 (CH_4)
$T_{b,in}$	K	Inlet temperature of reactive gas	873.15	873.15
$T_{c,in}$	K	Inlet coolant temperature	298.15	298.15
T_{co}	K	Initial coolant temperature	298.15	298.15
$v_{c,in}$	m/s	Coolant inlet velocity	9	9

8.3   Solution procedure (COMSOL Multiphysics[TM])

A 2-D axi-symmetric geometry with different domains as shown in Fig. 8.1 was created. Suitable in-built COMSOL modules, based on the governing modeling equations, were chosen for the packed bed and coolant section. Relevant constants, variables and expressions were specified for respective model equations (Table 8.1 and Appendix E) and appropriate initial and boundary conditions were incorporated. The modeling equations with prescribed inlet conditions were solved numerically by dividing respective domains and boundaries into finite elements using an appropriate mesh size with time stepping based on a backward differentiating formula (BDF) incorporated into COMSOL. The equations were discretized using Galerkin finite element method and solved using an iterative method based on Newton Raphson technique. A suitable convergence criterion was adopted for the iterations related to dependent variables as well as for time stepping. COMSOL modules used for simulations purposes along with meshing, solver and convergence related details are presented in Table 8.2. Simulations were performed subsequently to study the effect of various parameters on the bed temperature profiles.

Table 8.2

COMSOL – Modules, meshing and convergence criteria used in the present study

Transient Modules	Packed bed section: Transport of diluted species in porous media and Heat transfer in porous media
	Coolant section: $k - \epsilon$ turbulence model and Heat transfer in fluids
Discretization	Galerkin finite element method (incorporated in COMSOL)
Meshing	Fine meshing
	Number of triangular domain elements: 12313
	Number of boundary elements: 1098
Solver	PARDISO
Convergence	Newton-Raphson based iterative method; Tolerance: 10^{-3}
	Damping factor: 0.7

8.4   Model - Results and discussions

8.4.1   Model validation

As discussed in section 8.1, a dynamic pseudo-homogeneous model has been developed to predict transient behaviour of a UMC based PBR integrated with heat transfer to a coolant. Model results were obtained using COMSOL Multiphysics^{TM}, incorporating prescribed operating conditions and simulation parameters (see Table 8.1). Satisfactory convergence was obtained for the selected finite elements (Table 8.2) and time stepping. The total heat transfer to the coolant obtained using the model for two illustrative runs discussed in section 7.1 was compared with experimental data. Results obtained for one cycle of oxidation and reduction at "cyclic" steady state is tabulated in Table 8.3. In the case of the model, the total heat transfer from OSRM domain was calculated using the time averaged heat flux at the interface of the domain and coolant section and that from experimental data was based on coolant temperature rise and excluding any external power supplied at "cyclic" steady state. The values were found to be in agreement to within $\pm 2\%$.

Table 8.3

Comparison of model and experimental results for total heat transfer

Run. No.	Inlet Flowrates (LPM)				Inlet temperature (K)	Total heat transfer to coolant in one cycle (kJ)	
	Zero air	CH$_4$	N$_2$	Coolant air		Experimental*	Model
1	15	2	18	125	873.15	508 ± 10	512
2	15	2	18	150	873.15	541 ± 14	550

*At "cyclic" steady state

Model predictions were subsequently obtained in the OSRM domain under the same conditions as in run 1 for variation of temperature with time at two axial positions A and B (corresponding to TI – 14 and TI – 18 in the experiment). The same is plotted in Fig. 8.2 and Fig. 8.3 for oxidation and reduction respectively.
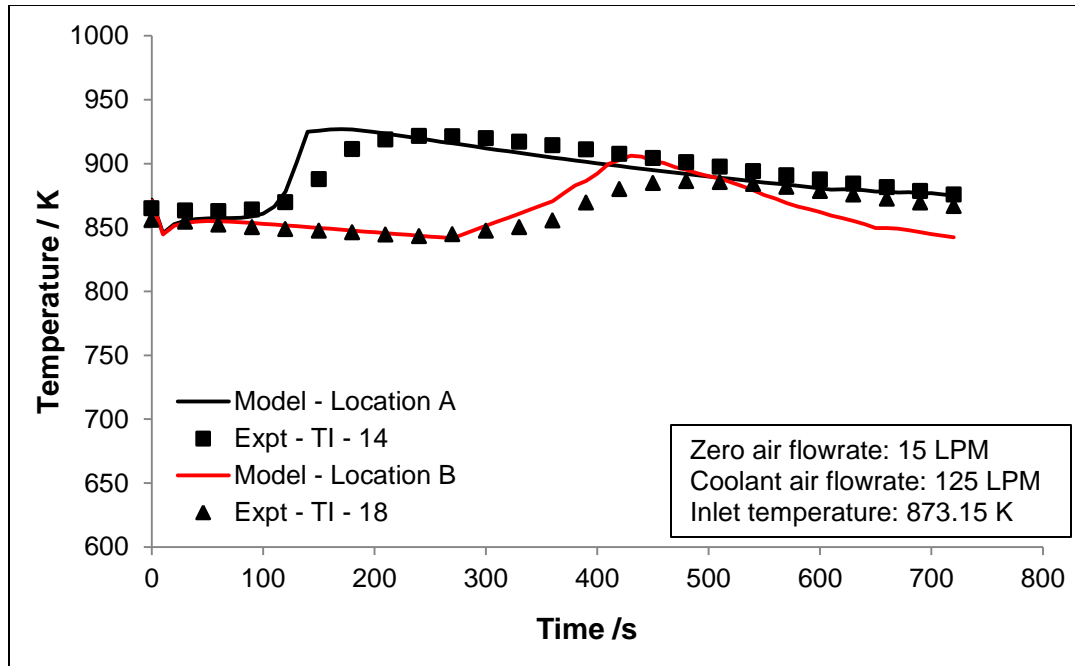
Fig. 8.2 Temperature variation with time at two locations during oxidation cycle at "cyclic" steady state (model vs. experiment)
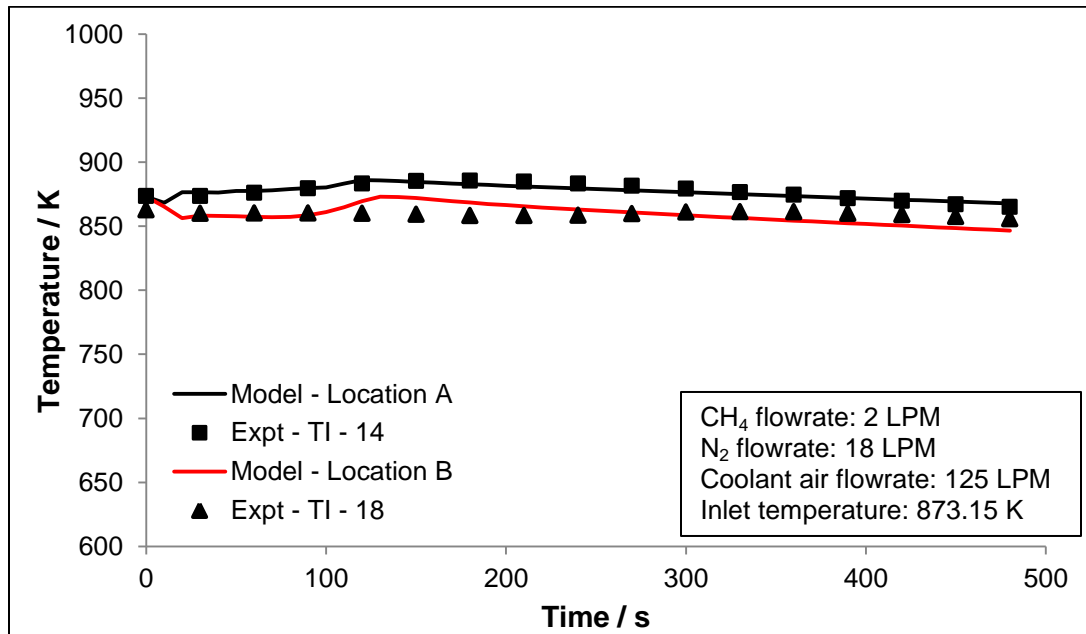
Fig. 8.3 Temperature variation with time at two locations during reduction cycle at "cyclic" steady state (model vs. experiment)

It is observed that the predicted values in these plots agree with those obtained from experiments to better than ± 7 %. The temperature variations are mainly governed by exothermicity of reactions involved, reaction and heat front velocities and cycle time. The model trends obtained can be explained using the arguments presented in section 7.1.1. In each oxidation and reduction cycle, the maximum temperature rise was found not to exceed 60 K and 10 K respectively.

In addition, the spatial variation of temperature in the axial and radial direction at two different times is plotted in Figs. 8.4 / 8.5 and Figs. 8.6 / 8.7 respectively for oxidation and reduction. Good agreement to within ± 6 % for oxidation and ± 9% for reduction between predicted and experimental values is observed. In view of this agreement, subsequent modifications were considered unnecessary and no empirical adjustments have been made in the model.
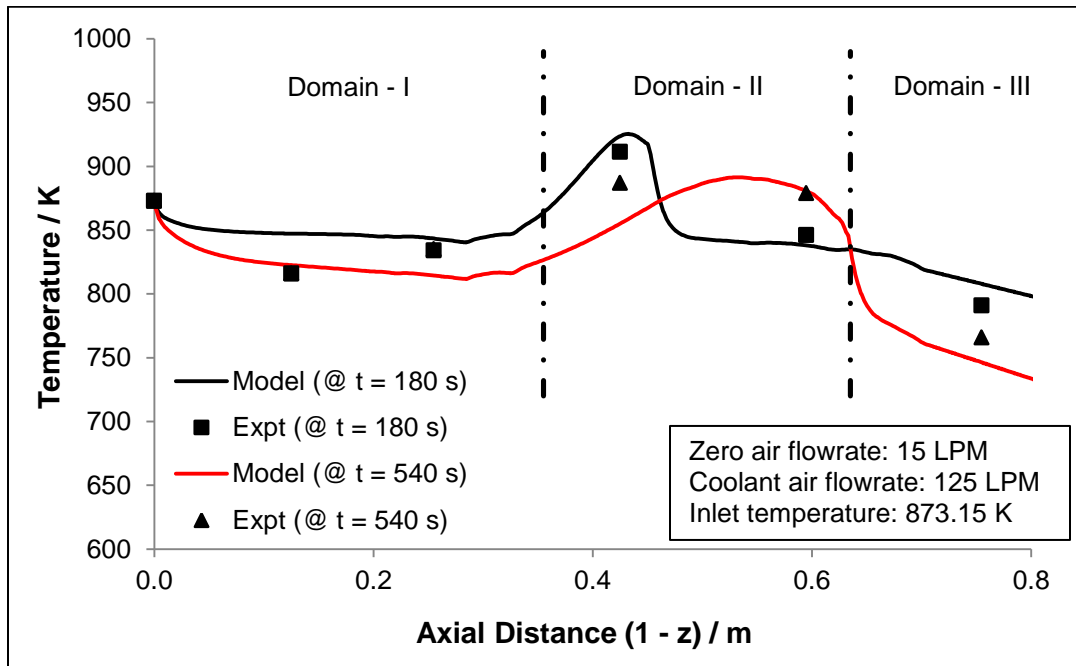
Fig. 8.4 Axial temperature variation in the bed during oxidation at $r = 0.0155$ m and at 180 and 540 seconds (model vs. experiment)
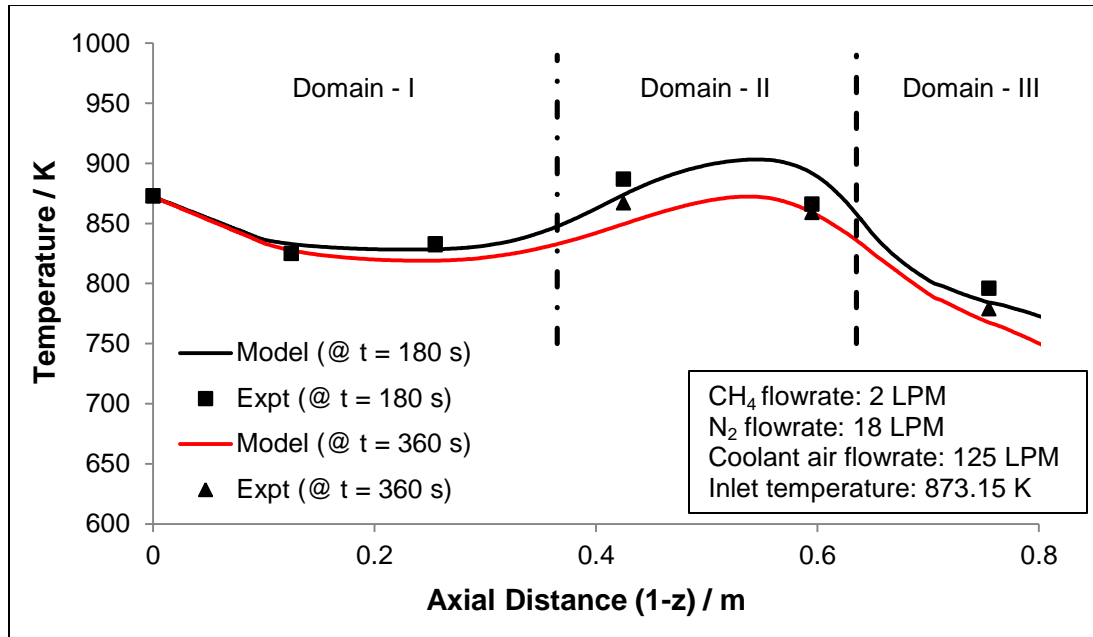
Fig. 8.5 Axial temperature variation in the bed during reduction at $r = 0.0155$ m and at 180 and 360 seconds (model vs. experiment)
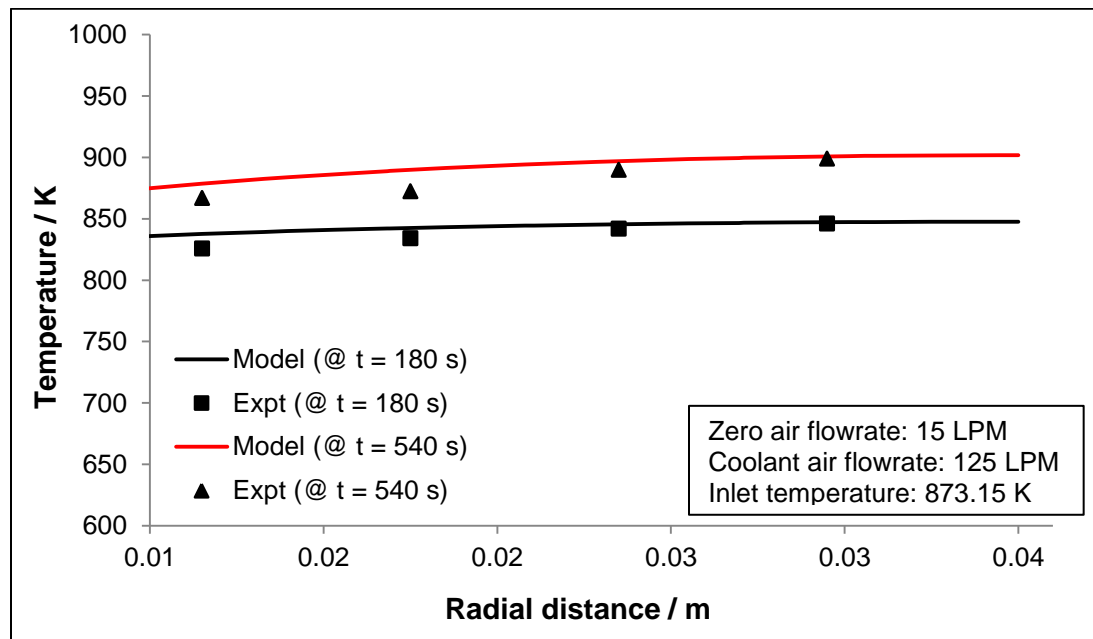
Fig. 8.6 Radial temperature variation in the bed during oxidation at $(1 - z) = 0.58$ m and at 180 and 540 seconds (model vs. experiment)
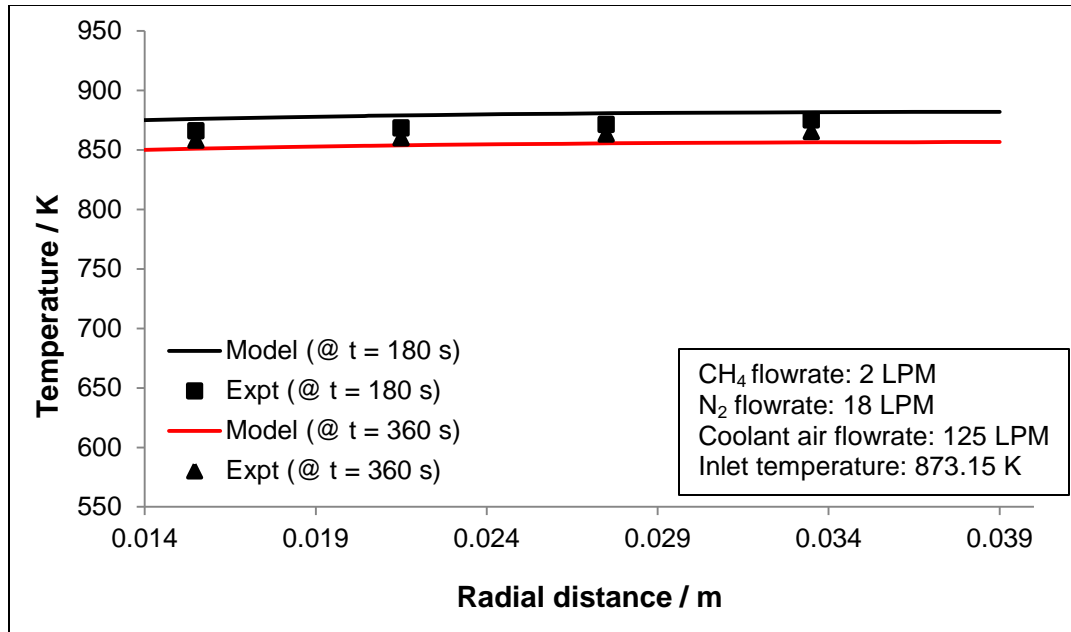
Fig. 8.7 Radial temperature variation in the bed during reduction at $(1 - z) = 0.58$ m and at 180 and 360 seconds (model vs. experiment)

Fig. 8.4 depicts the axial temperature variation at $r = 0.0155$ m. It is observed that at both times the temperature in the OSRM is higher than that in the inert domain on either sides due to absence of reaction in these domains. The reaction and heat front propagation is evident at 540 seconds as is indicated by a shift in the temperature profile. The decrease in temperature in domain – III is because of axial convection and counter current radial heat transfer to coolant. A similar trend is observed in the case of reduction (Fig. 8.5) with the exception that the temperature rise in the OSRM domain due to reaction is lower as compared to the rise in oxidation due to higher reaction enthalpy and reaction rate of the latter.

The radial temperature profile at a location $((1 - z) = 0.58$ m$)$, for oxidation, at two different times of 180 and 540 seconds is shown in Fig. 8.6. It is observed that the temperature at 540 seconds is relatively higher as compared to that at 180 seconds. This can be attributed to the reaction front moving past this location only after 180 seconds. The radial temperature drop is also higher at 540 seconds (~ 24 K) against that at 180 seconds (~ 10 K) due to the lower effective thermal conductivity associated with alumina

and CuO, the latter formed during this reaction. This decrease in thermal conductivity is however compensated for by the larger temperature difference between the OSRM bed and coolant, thereby sustaining radial heat transfer.

Results are presented at 180 and 360 seconds for reduction at the same location in Fig. 8.7. The temperature at 180 seconds is relatively higher as compared to 360 seconds. In this case, the reaction front moves past this location at 180 seconds due to its higher velocity as compared to that in the case of oxidation. At 360 seconds, axial convection in combination with the radial heat transfer results in cooling of the bed. The radial temperature drop is however the same for both cases, with the effective thermal conductivity of alumina and Cu now compensating for the lower temperature difference between the OSRM bed and coolant at 180 seconds enabling sustained radial heat transfer.

8.4.2   Parametric studies

The effect of relevant operating parameters on the OSRM bed temperature profile was predicted using the 2-D pseudo-homogeneous model and the same is presented in this section. For a change in a specific parameter, all other operating conditions were maintained the same as those in illustrative run 1 shown in Table 8.3. Model predictions for temperature profiles were obtained at two axial locations A ($r = 0.0155$ m, $z = 0.58$ m) and B ($r = 0.0155$ m, $z = 0.42$ m). Results are presented for zero air flowrates of 5 and 20 LPM, coolant flowrates of 100 and 175 LPM and a methane flowrate of 6 LPM corresponding to 30 mol % concentration.

As depicted in Fig. 8.8, at a zero air flowrate of 5 LPM, no temperature rise at location B due to reaction exothermicity is observed. The reaction front does not propogate to this location in the 12 minutes of the cycle time associated with oxidation and the bed remain partially oxidized indicated by a rise in temperature at location A. At 20 LPM, the OSRM domain temperature drops due to convective cooling arising from excess zero air supply, the effect being more prominent at location A.
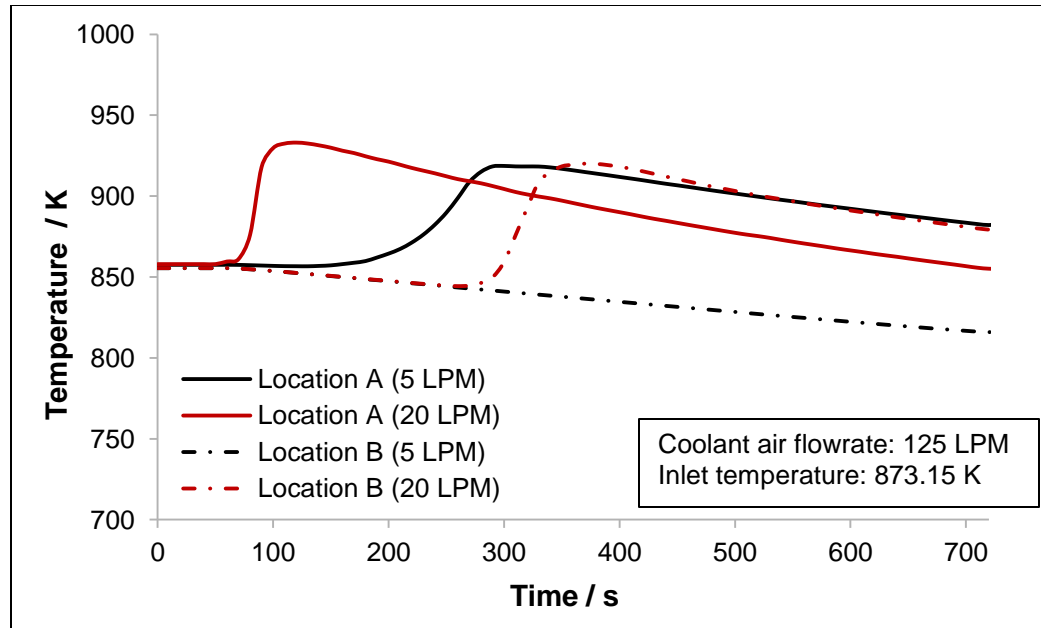
Fig. 8.8 Model predictions of bed temperature profiles at two axial locations during oxidation for two different zero air flowrates (5 and 20 LPM)

The effect of coolant flowrate at 100 LPM and 175 LPM is shown in Fig. 8.9. The bed temperature is observed to be higher in the case of 100 LPM at location A due to a lower temperature difference between the OSRM domain and coolant which limits the heat transfer. At location B, there exists an increased temperature difference between the bed and the coolant as a result of counter-current flow arrangement which increases the radial heat transfer and limits the temperature rise at this location. At 175 LPM, the temperature at both locations is observed to decrease to 835 K and 804 K at which sustaining the combustion process becomes a challenge.

The effect of increasing methane concentration is shown in Fig. 8.10. At a methane concentration ~ 30 mol% corresponding to methane flowrate of 6 LPM, the OSRM temperature is seen to decrease to 811 K and 817 K at locations A and B respectively. Under these conditions, combustion cannot be sustained.

The above results are in alignment with experimental results related to parametric effects discussed in section 7.1.2.
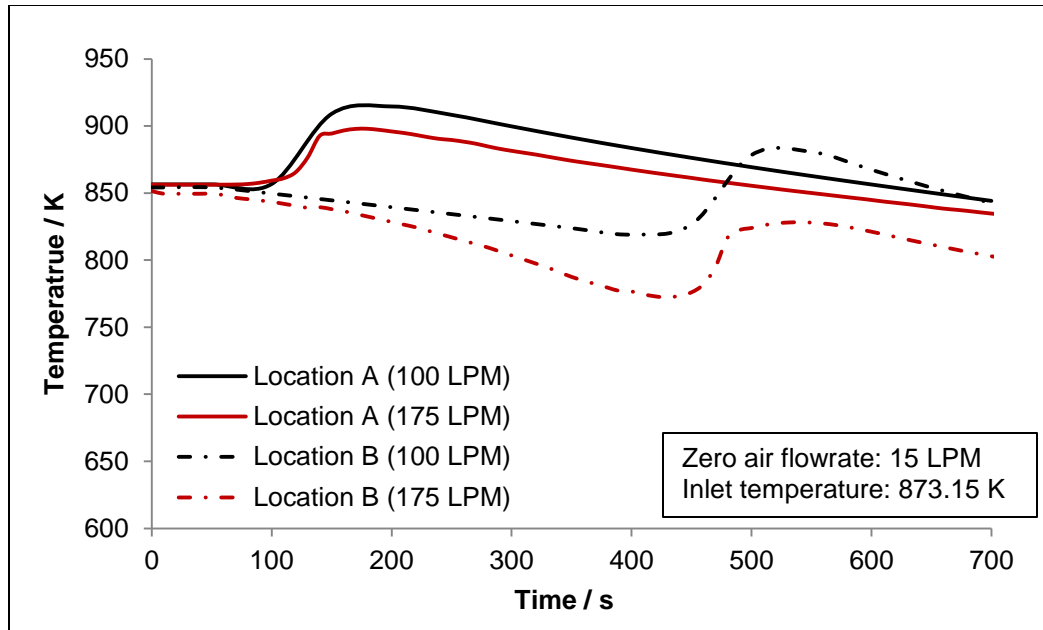
Fig. 8.9 Model predictions of bed temperature profiles at two axial locations during oxidation for two different coolant flowrates (100 and 150 LPM)
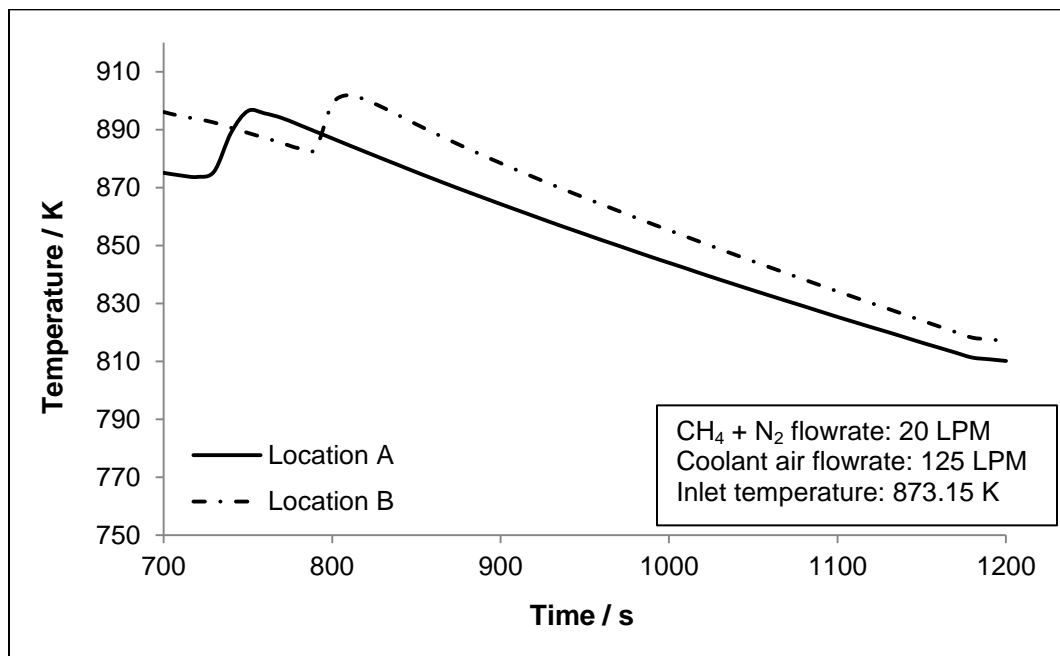
Fig. 8.10 Model predictions of bed temperature profiles at two axial locations during reduction for 30 mol % of CH_4 concentration

Chapter 9

Conclusions and Recommendations

9.1   UMC based heat transfer investigations

The feasibility of using a dynamically operated UMC based packed bed reactor for heat transfer applications with CuO/Cu on alumina as a representative OSRM has been experimentally demonstrated for the first time at a national level and to the best of knowledge internationally. Sustained cyclic UMC operation under near isothermal conditions is possible incorporating radial heat transfer primarily by conduction to a coolant. Stable coolant outlet temperature was obtained with minimal bed temperature rise due to reaction exothermicity of both oxidation and reduction.

A test rig involving an annular packed bed reactor for investigating UMC and its effect on heat transfer was designed, fabricated and successfully commissioned. Under a prescribed OSRM loading of 1.25 kg and fixed reaction cycle times, radial heat transfer primarily by conduction to coolant air was maximized at $95 \pm 2\%$ of the total energy in the bed for zero-air, methane and coolant flowrates of 15 LPM, 2 LPM and 150 LPM respectively and an inlet temperature of 873.15 K. Under these conditions, at "cyclic" steady state, external heating was limited to less than 10% indicating that sustained combustion with heat transfer is possible. The maximum bed temperature rise was found not to exceed 10 K and 60 K for reduction and oxidation respectively. The temperature rise was greater in the case of oxidation as compared to reduction due to higher reaction enthalpy and reaction rate. The coolant outlet temperature variation at "cyclic" steady state was restricted to $\pm$ 3K. A parametric study related to the effect of zero air, methane and coolant flowrate on the radial heat transfer was also carried out. At a zero air flowrate around 5 LPM, the OSRM bed was partially oxidized. In subsequent reduction cycles, the convective flow of methane and nitrogen was found to decrease the temperature difference between the bed and coolant that is required for radial transfer. The bed temperature was found to decrease at higher flowrates of air (~ 20 LPM) due to

convective flow of excess air in the axial direction over the reacted portion of the bed resulting in cooling. At higher methane flowrates of 4 and 6 LPM, the radial heat transfer was observed to be again limited by convective cooling. The heat transfer was also found to be inhibited by insufficient coolant flowrate at 100 LPM. At higher coolant flowrates, the bed temperature and hence the temperature difference for heat transfer was found to decrease. Under all of the above conditions, the external power supply contribution to the total heat transfer was found to increase. The choice of reaction cycle time was influential in facilitating radial heat transfer with minimal variations in bed and coolant outlet temperature.

The results obtained in the present study provide an excellent case to promote the use of UMC for process heat transfer applications. However, addressing the issues related to choice of OSRM, reactor material of construction and formation of coke at higher temperature will be the key drivers for successful application of this concept at a large scale. The installation of online analyzers to measure the gas concentrations at the outlet of the OSRM bed can help predict cycle times more accurately and prevent carryover of unreacted oxygen and methane in respective product streams. The results obtained can be extended to applications like boilers, steam reforming, gasification and possibly E/C engines. In boiler applications, the enthalpy of exothermic reactions associated with UMC can be transferred across a surface by conduction and convection to heat water and generate steam. In steam reforming with Ni as OSRM, the exothermicity of oxidation can be utilized to simultaneously carry out reforming and calcination in a fixed bed. Ni in this case also acts as a catalyst for the reforming reaction. But the scale-up of suitable reactors for any of these applications and difficulties involved in operating the system in a cyclic mode while maintaining sustained combustion at such a scale would need further investigations at a pilot level.

9.2   PMR based kinetic studies

The potential of a PMR to estimate global kinetic parameters of non-catalytic gas-solid reactions has been demonstrated experimentally and theoretically using representative Cu

oxidation and CuO reduction reactions, encountered in UMC. Careful experimental measurements under plug flow conditions were conducted using this reactor system for these reactions. The amount of OSRM and sample volume size to be injected was critical in ensuring that accurate kinetic data was obtained. Flow and thermal perturbation effects during the test runs were negligible. Temperature variations in the bed due to exothermicity were minimal and data was obtained under near isothermal conditions. A uniform reaction based methodology has been proposed to estimate the values of pre-exponential factor and activation energy for such reactions. The predicted values of reaction orders for oxidation were obtained as 0.1 and 1 with respect to Cu and O_2 respectively and those for reduction were 0 and 0.4 with respect to CuO and CH_4 respectively. The values of activation energies for both reactions and pre-exponential factor for oxidation estimated from respective Arrhenius plots are in excellent agreement with the results obtained by Garcia – Labiano et. al. [23] using a TGA. The pre-exponential factor for reduction however was lower in value compared to that obtained by Garcia – Labiano et. al. [23] due to the use of steam in their investigations. Both reactions were initially assumed to be surface reaction controlled. The influence of external mass transfer and intra-particle diffusion on the reaction rates was investigated using the Mears' and Weisz-Prater criteria. These effects based on these criterions were found to be inconsequential and validated the assumption made in this regard. The present investigation validates the use of this methodology for reactions which are surface reaction controlled. The methodology allows for use of this reactor system to study linear and non-linear kinetics of non-catalytic gas-solid reactions. In addition the PMR prima facie provided useful data related to OSRM stability under cyclic conditions, operating conditions and coke formation prior to the design and fabrication of the UMC – heat transfer test rig.

With its simple construction and operational protocol based on small quantities of solid and plug flow conditions, it provides experimental data efficiently and is amenable to obtaining kinetic parameters under acceptable reaction engineering conditions when access to the more expensive TGA and TAP reactors are not easily available. The PMR data obtained can also be used in conjunction with other particle reaction models

established in literature when internal transport limitations are significant. A suitable methodology to interpret the data needs to be accordingly developed and the PMR system may need to be modified accordingly. With an increasing demand to reduce costs and maximize information during early stages of kinetic experimentation, the PMR is well placed as a good workhorse for those reaction systems where it can be applied.

9.3   Modeling and simulation studies

A 2-D pseudo-homogenous mathematical model for a UMC based packed bed system integrated with heat transfer to a coolant was also developed for the first time. COMSOL Multiphysics^{TM} was used for model implementation and a finite element based numerical method incorporated in COMSOL was adopted for solving respective governing equations and converged solutions were obtained for prescribed simulation parameters. The predicted model results of the total heat transfer to coolant for one cycle comprising of oxidation and reduction along with axial and radial temperature profiles in the bed show agreement to better than $\pm$ 9 % with respective experimental measurements. This agreement validates the use of a pseudo-homogeneous model for the relatively mild conditions used in this study. The effect of flowrates of zero air, coolant and methane on the bed temperature profiles was investigated by conducting simulation studies using the validated model. The results obtained helped in identifying limits of these operating variables to be used for a specific OSRM loading and fixed cycle times to achieve continuous radial heat transfer with sustained unmixed combustion in the reactor. In addition, the model results support the fact that heat transfer to coolant is primarily by conduction as radial convection in the ORSM bed was neglected.

The model results confirm the suitability of adopting a pseudo-homogeneous approach to predict the dynamic behavior of complex UMC based PBR systems for specific operating conditions as those encountered in the present study. However heterogeneous models may be required if operating conditions are more severe resulting in intra-particle concentration and temperature gradients due to structural changes in the solid.

Appendix A

Reactor: Dimensions and Thermo-well Locations
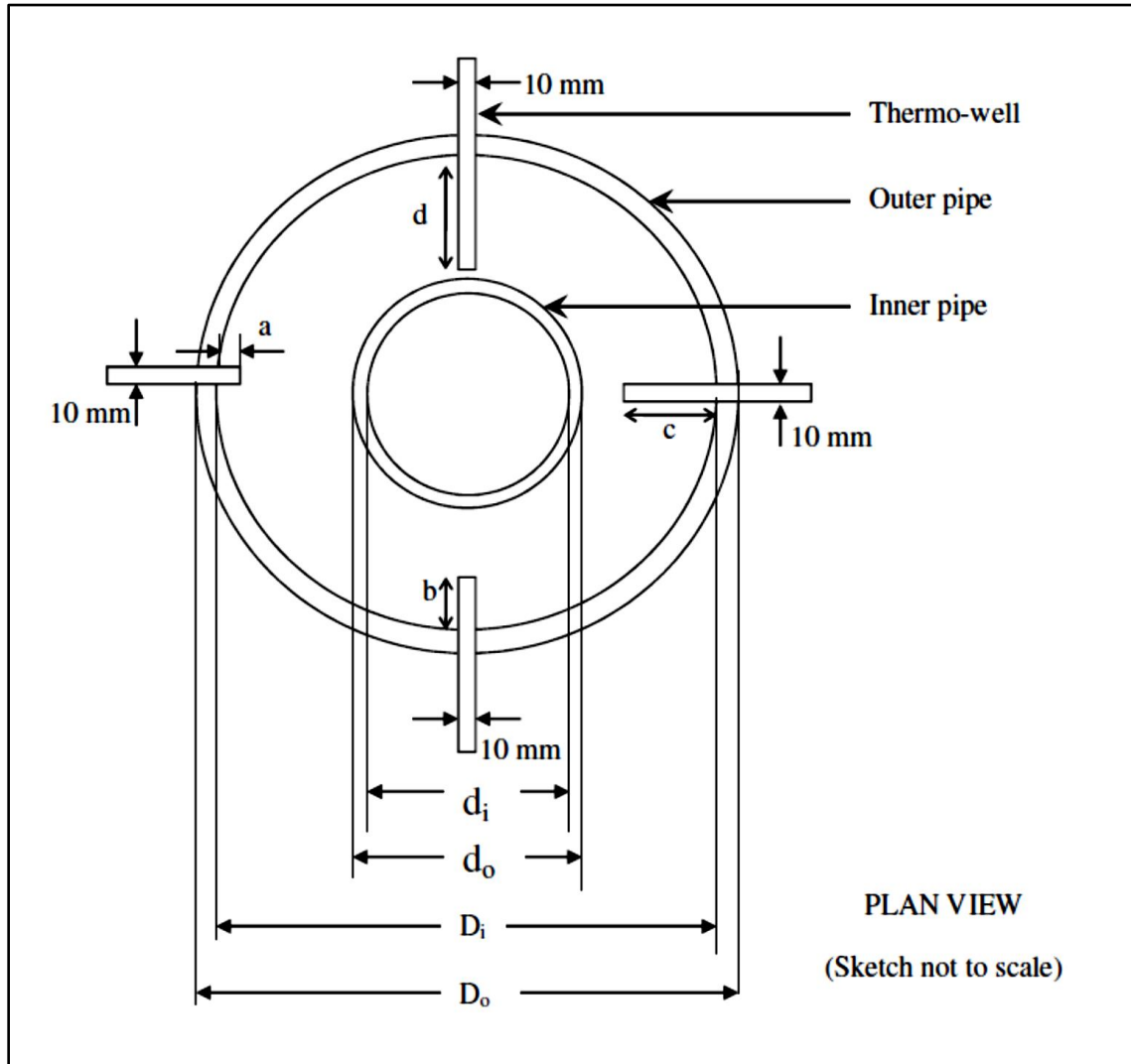
Fig. A.1 Reactor: Thermowell locations (radial)

d$_i$	d$_o$	D$_i$	D$_o$	a	b	c	d
26.6	33.4	77.9	88.9	2.5	8	13	18

All values are in mm.
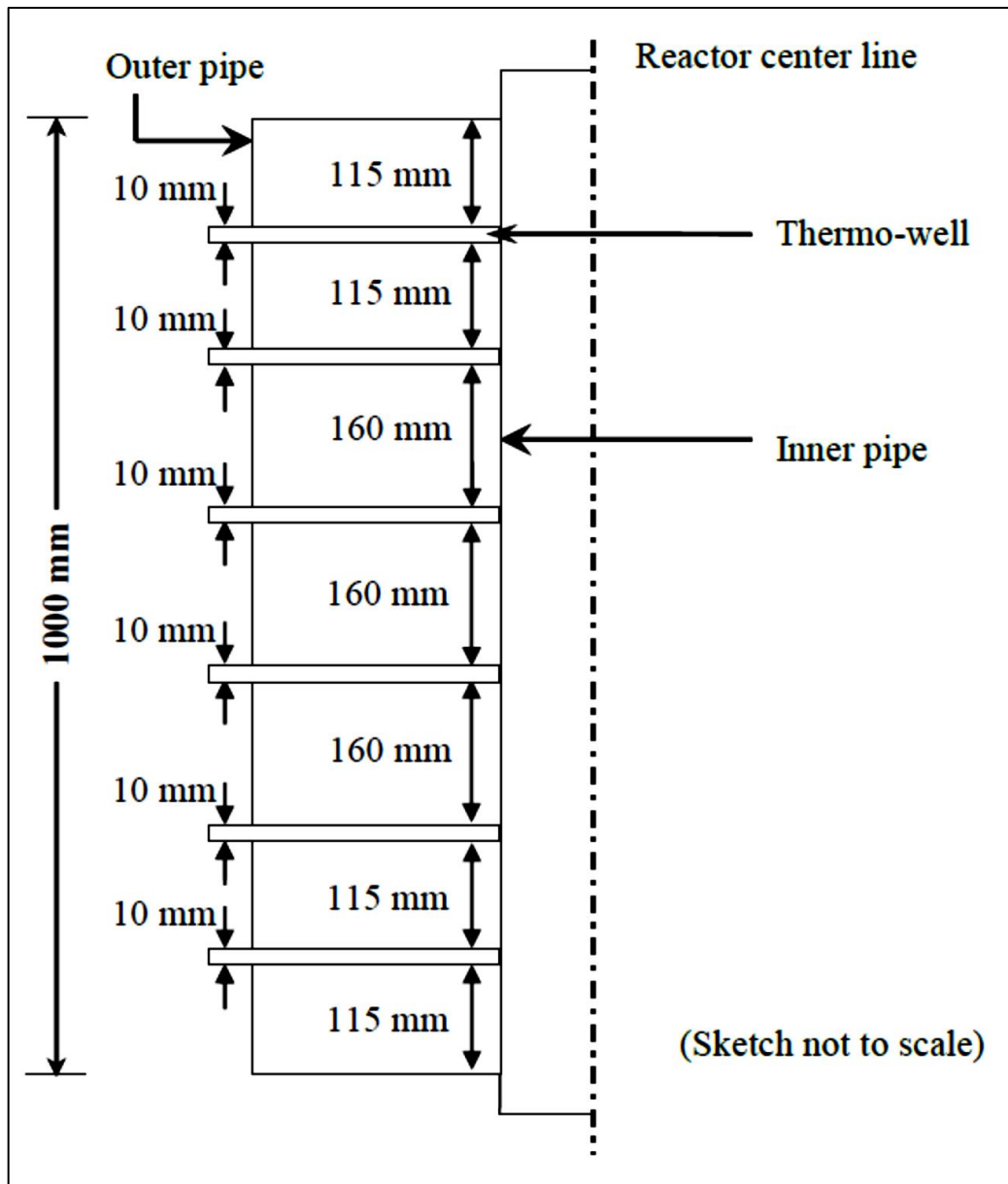
Fig. A.2 Reactor: Thermowell locations (axial)

Appendix B

Thermocouple Calibration

All the thermocouples used in the Pulsed Micro-reactor (PMR) and heat transfer test runs were made of nickel–chromium / nickel-aluminium (K-type) and calibrated in the range of 523.15 – 1373.15 K.

In all, 34 thermocouples were calibrated against a standard K-type thermocouple (calibrated by the National Accreditation Board for Testing and Calibration Laboratories (NABL), India) with the thermodynamic temperature deviation ranging in magnitude from 0.9 K to 3.2 K in the temperature range of 523.15 – 1473.15 K. The calibration data for the standard thermocouple at five different points are given in Table B.1

Table B.1

Calibration data for the standard K-type thermocouple

Sr. No.	Standard sensor	Standard K-type thermocouple		Deviation
	Temp ^{o}C	mV	Temp ^{o}C	Temp ^{o}C
1	249.66	10.10	248.71	− 0.95
2	499.29	20.54	497.51	− 1.78
3	799.90	33.17	797.51	− 2.39
4	1000.22	41.17	997.32	− 2.90
5	1200.59	48.74	1197.39	− 3.20

Temperature scale: ITS – 90   Ambient Temp.: $25 \pm 2\ ^o$C

To obtain a relation between the thermo-emf (e) reading in mV and temperature, the calibration data in Table B.1 were fitted by the following equation ($R^2 = 0.99$)

$$T \text{ (K)} = 0.043 \times (e)^2 + 21.92 \times (e) + 24.841 + 273.15 \tag{B.1}$$

With regard to the 34 thermocouples, the calibration runs were carried in the range 523.15 K to 1373.15 K at 18 different points in this interval. A dry temperature bath (supplied by Tempsens Instruments^{TM}) was used for calibration purposes. The bath was fitted with a heater and an automatic temperature controller which maintained a steady temperature to within ± 1 K in the entire range. At any time, this bath had an arrangement for simultaneously positioning 6 thermocouples of different diameters ranging from 1.5 mm to 4 mm. The thermocouples to be calibrated were positioned along with standard thermocouple at a pre-defined depth in the bath where the temperature variation was limited to 0.1 K. At each temperature, the thermo-emfs' of the thermocouples were noted along with that of the standard thermocouple within 3 minutes of each other. The readings were noted after steady state was attained where variation in the bath temperature was less than 1 K as indicated by standard thermocouple,

The calibration data obtained were fitted using the method of least squares resulting in the following form of an equation (with R^2 values ranging between 0.98 – 0.99) applicable to all 34 thermocouples.

$$T \text{ (K)} = C_1 \times (e)^2 + C_2 \times (e) + C_3 + 273.15 \qquad \text{(B.2)}$$

The values of the constants in the equation for individual thermocouples are given in Table B.2

Table B.2
Values of C_1, C_2 and C_3 in equation (B.2) for different thermocouples

Thermocouple Tag No*	C_1	C_2	C_3
TI – 01	0.1154	19.465	52.458
TI – 02	0.144	17.308	72.798
TI – 03	0.0316	22.269	24.762
TI – 04	0.031	22.316	20.653
TI – 05	0.0366	22.101	25.942
TI – 06	0.0232	22.752	20.589

TI – 07	0.0374	22.173	20.137
TI – 08	0.0248	22.318	26.764
TI – 09	0.0443	21.645	28.641
TI – 10	0.0395	21.938	24.722
TI – 11	0.0323	22.243	25.156
TI – 12	0.0248	22.570	19.292
TI – 13	0.043	21.831	26.363
TI – 14	0.0446	21.689	27.883
TI – 15	0.0312	22.372	23.054
TI – 16	0.0326	22.222	21.849
TI – 17	0.0288	22.424	20.854
TI – 18	0.0273	22.514	20.713
TI – 19	0.0351	22.302	19.316
TI – 20	0.0371	22.069	24.793
TI – 21	0.0263	22.608	21.747
TI – 22	0.0401	21.912	27.584
TI – 23	0.0436	21.985	21.574
TI – 24	0.0379	22.008	24.207
TI – 25	0.0261	22.633	18.454
TI – 26	0.0269	22.558	21.023
TI – 27	0.1217	19.512	54.213
TI – 28	0.1442	17.308	72.798
TI – 29	0.1336	17.739	66.611
TI – 30	0.0386	22.096	21.879
TI – 31	0.0436	22.017	21.406
TI – 32	0.0276	22.894	20.56
TI – 33	0.0195	23.223	14.64
TI – 34	0.1442	17.672	66.81

* Tag numbers correspond to the thermocouples located at positions shown in Fig. 4.2.

Thermocouples TI – 01 and TI – 02 were also used in PMR test rig for kinetic study to

measure temperatures at the reactor wall and at a location inside the reactor respectively.

A MASIBUS Scanner (indicator) was then calibrated against each of these 34 thermocouples using the dry temperature bath in the same temperature range and at the same 18 temperatures used earlier. The standard K-type thermocouple was also used as part of the calibration runs to measure the bath temperature (using equation B.1). At every temperature, the emf values of each of the 34 thermocouples was converted to temperature values using equation B.2 The calibration data obtained in this case was fitted using the method of least squares resulting in the following equation (with R^2 values ranging between 0.98 – 0.99)

$$T_{T/C}(K) = A \times (T_{ind})^2 + B \times (T_{ind}) + C + 273.15 \tag{B.3}$$

where $T_{T/C}$ and T_{ind} denote temperature indicated by thermocouples and MASIBUS scanner respectively. The values of constants A, B and C obtained from the curve fit for all the 34 thermocouples are presented in Table B.3 below.

Table B.3

Values of A, B and C in equation (B.3) for different thermocouples

Thermocouple Tag No*	A	B	C
TI – 01	-4.00E-05	1.043	-12.45
TI – 02	2.00E-05	0.984	-3.016
TI – 03	7.00E-06	0.992	-2.353
TI – 04	-2.00E-05	1.018	-10.06
TI – 05	-9.00E-06	1.008	-5.396
TI – 06	-6.00E-06	1.006	-6.104
TI – 07	-5.00E-06	1.005	-6.87
TI – 08	-2.00E-05	1.028	-20.79
TI – 09	-3.00E-05	1.024	-10.4
TI – 10	-1.00E-05	1.01	-7.374

TI – 11	-1.00E-05	1.012	-6.98
TI – 12	2.00E-05	0.979	1.29
TI – 13	-1.00E-05	1.009	-5.919
TI – 14	7.00E-06	0.993	-3.72
TI – 15	-3.00E-05	1.034	-15.09
TI – 16	2.00E-06	0.995	-3.125
TI – 17	2.00E-05	0.972	1.564
TI – 18	2.00E-05	0.973	3.572
TI – 19	-8.00E-06	1.004	-4.594
TI – 20	-2.00E-05	1.022	-11.82
TI – 21	1.00E-05	0.979	1.692
TI – 22	-3.00E-05	1.026	-10.82
TI – 23	-1.00E-06	1.001	-4.563
TI – 24	-3.00E-05	1.033	-14.98
TI – 25	8.00E-06	0.986	-0.48
TI – 26	-3.00E-06	1.002	-5.198
TI – 27	-2.00E-05	1.02	-5.787
TI – 28	2.00E-05	0.984	-3.016
TI – 29	-8.00E-07	1.001	-5.23
TI – 30	-1.00E-05	1.012	-7.429
TI – 31	-8.00E-06	1.005	-4.84
TI – 32	-5.00E-05	1.055	-17.07
TI – 33	-2.00E-05	1.019	-9.441
TI – 34	7.00E-05	0.92	17.53

* Tag numbers correspond to the thermocouples located at positions shown in Fig. 4.2.

Appendix C

Gas Chromatograph Settings in PMR based Kinetic Studies

A Gas Chromatograph (GC) was an integral part of the Pulsed Micro-reactor (PMR) test rig which was used to estimate kinetic parameters of reactions involving Cu and CuO. Product gases exiting the PMR after injection of each pulse were analyzed using the GC. The product gases were O_2 and N_2 during oxidation of Cu and CH_4 and CO_2 during reduction of CuO. The GC settings used in this study are given in Table C.1.

Table C.1

GC settings

	Oxidation of Cu	Reduction of CuO
Column	Molecular Sieve	Porapak Q
Injector temperature	373.15 K	473.15 K
Column and Oven temperature	333.15 K (10 min)	333.15 K (5 min) ramped to 423.15 K (20 K / min) 423.15 K (15 min)
Detector used	TCD	TCD
TCD temperature	373.15 K	473.15 K
Carrier gas	Argon (Ar)	Argon (Ar)
Ar flowrate	35 SCCM	35 SCCM

The retention time for each gas was inclusive of the time the gas spends in the PMR and GC column prior to detection. The retention times are as

1. O_2 – 4.4 min
2. N_2 – 5.1 min
3. CH_4 – 2.1 min
4. CO_2 – 11.2 min

Appendix D

OSRM Sample Analysis Report

Fresh 13 wt% CuO on alumina sample procured from Sigma Aldrich[TM] was used as a representative OSRM and the same was characterized to estimate BET surface area and pore volume distribution. This analysis was carried out by the expert analyst at Aditya Birla Science and Technology Ltd. The reports of this analysis is provided below:

ADITYA BIRLA

SCIENCE & TECHNOLOGY CO. LTD

Analytical Science &Technology

Date- 1/09/2014
R.A-Mangesh Jadhav

Surface Area Report

Background

Samples: Sample A was submitted for Nitrogen surface area, pore distribution & pore volume analysis.

Customer: Mr.Amol Niphade

Date submitted: 26th Aug 2014

Instrument: Surface area analyzer- Autosorb-1C

Experimental

Sample Preparation for analysis

➢ Degassing is by **vacuum degassing** method at 200 ± 5°C for 180min.

Measurement Procedure

➢ Dewar is filled with liquid nitrogen and allowed to set for 10-15min.

➢ Selected relative pressure (p/p⁰) ranging from 0.025-0.995 (79point BET)

Results: BJH adsorption pore size distribution data is tabulated in Table-1

Table-1

Diameter	Pore Vol	Pore Surf Area	Dv(d)	Ds(d)	Dv(log d)	Ds(log d)
Å	[cc/g]	[m²/g]	[cc/Å/g]	[m²/Å/g]	[cc/g]	[m²/g]
28.05	6.37E-003	9.09E+000	4.65E-003	6.63E+000	3.00E-001	4.28E+002
29.46	1.34E-002	1.86E+001	4.82E-003	6.55E+000	3.27E-001	4.44E+002
30.96	2.04E-002	2.77E+001	4.59E-003	5.93E+000	3.27E-001	4.23E+002
32.65	2.88E-002	3.80E+001	4.52E-003	5.54E+000	3.40E-001	4.16E+002
34.37	3.50E-002	4.51E+001	3.90E-003	4.53E+000	3.08E-001	3.59E+002
36.17	4.29E-002	5.39E+001	3.89E-003	4.31E+000	3.24E-001	3.59E+002
38.22	5.03E-002	6.16E+001	3.60E-003	3.77E+000	3.17E-001	3.32E+002
40.35	5.79E-002	6.92E+001	3.47E-003	3.44E+000	3.22E-001	3.19E+002
42.63	6.52E-002	7.60E+001	3.07E-003	2.88E+000	3.02E-001	2.83E+002
45.14	7.28E-002	8.28E+001	2.86E-003	2.54E+000	2.98E-001	2.64E+002
47.92	8.06E-002	8.93E+001	2.70E-003	2.25E+000	2.98E-001	2.49E+002
51.05	8.85E-002	9.55E+001	2.34E-003	1.84E+000	2.75E-001	2.16E+002
54.52	9.67E-002	1.02E+002	2.29E-003	1.68E+000	2.87E-001	2.11E+002
58.38	1.06E-001	1.08E+002	2.27E-003	1.56E+000	3.05E-001	2.09E+002
62.86	1.15E-001	1.14E+002	1.88E-003	1.19E+000	2.71E-001	1.73E+002
68.16	1.25E-001	1.20E+002	1.79E-003	1.05E+000	2.80E-001	1.64E+002
74.18	1.36E-001	1.25E+002	1.61E-003	8.69E-001	2.75E-001	1.48E+002
81.14	1.47E-001	1.31E+002	1.51E-003	7.46E-001	2.83E-001	1.39E+002
89.52	1.59E-001	1.36E+002	1.29E-003	5.75E-001	2.65E-001	1.18E+002
99.96	1.73E-001	1.42E+002	1.17E-003	4.68E-001	2.69E-001	1.08E+002
113.14	1.87E-001	1.47E+002	9.69E-004	3.43E-001	2.52E-001	8.91E+001
130.46	2.03E-001	1.52E+002	8.20E-004	2.51E-001	2.46E-001	7.54E+001
153.51	2.23E-001	1.57E+002	7.48E-004	1.95E-001	2.64E-001	6.87E+001
186.78	2.45E-001	1.61E+002	5.44E-004	1.17E-001	2.33E-001	4.99E+001
239.98	2.70E-001	1.66E+002	3.85E-004	6.42E-002	2.11E-001	3.52E+001
341.75	3.01E-001	1.69E+002	2.26E-004	2.65E-002	1.75E-001	2.05E+001
594.61	3.29E-001	1.71E+002	7.53E-005	5.06E-003	9.97E-002	6.71E+000
2207.65	3.48E-001	1.72E+002	6.74E-006	1.22E-004	2.88E-002	5.21E-001

BJH desorption pore size distribution data is tabulated in Table-2

Table-2

Diameter	Pore Vol	Pore Surf Area	Dv(d)	Ds(d)	Dv(log d)	Ds(log d)
Å	[cc/g]	[m²/g]	[cc/Å/g]	[m²/Å/g]	[cc/g]	[m²/g]
28.03	5.73E-003	8.18E+000	3.78E-003	5.39E+000	2.44E-001	3.48E+002
29.48	1.09E-002	1.51E+001	3.71E-003	5.04E+000	2.52E-001	3.42E+002
30.95	1.65E-002	2.24E+001	3.61E-003	4.66E+000	2.57E-001	3.32E+002
32.49	2.21E-002	2.93E+001	3.66E-003	4.50E+000	2.73E-001	3.37E+002
34.26	3.08E-002	3.94E+001	4.35E-003	5.08E+000	3.43E-001	4.00E+002
36.2	4.17E-002	5.15E+001	5.77E-003	6.38E+000	4.81E-001	5.31E+002
38.14	5.51E-002	6.56E+001	6.76E-003	7.09E+000	5.93E-001	6.22E+002
40.28	7.32E-002	8.35E+001	7.89E-003	7.84E+000	7.32E-001	7.27E+002
42.65	9.07E-002	9.99E+001	7.13E-003	6.69E+000	7.00E-001	6.57E+002
45.22	1.02E-001	1.10E+002	4.04E-003	3.58E+000	4.21E-001	3.72E+002
48.01	1.12E-001	1.19E+002	3.73E-003	3.11E+000	4.12E-001	3.43E+002
51.13	1.24E-001	1.28E+002	3.50E-003	2.74E+000	4.11E-001	3.22E+002
54.62	1.36E-001	1.36E+002	3.24E-003	2.38E+000	4.08E-001	2.99E+002
58.47	1.48E-001	1.44E+002	2.90E-003	1.98E+000	3.90E-001	2.67E+002
62.96	1.61E-001	1.53E+002	2.71E-003	1.72E+000	3.93E-001	2.50E+002
68.16	1.75E-001	1.61E+002	2.58E-003	1.52E+000	4.05E-001	2.38E+002
74.03	1.91E-001	1.70E+002	2.53E-003	1.37E+000	4.31E-001	2.33E+002
81.1	2.10E-001	1.79E+002	2.46E-003	1.21E+000	4.59E-001	2.27E+002
89.54	2.32E-001	1.89E+002	2.43E-003	1.08E+000	5.00E-001	2.23E+002
100.07	2.58E-001	1.99E+002	2.11E-003	8.43E-001	4.86E-001	1.94E+002
113.51	2.84E-001	2.08E+002	1.75E-003	6.17E-001	4.57E-001	1.61E+002
129.99	3.08E-001	2.16E+002	1.33E-003	4.09E-001	3.97E-001	1.22E+002
153.03	3.27E-001	2.21E+002	6.84E-004	1.79E-001	2.40E-001	6.28E+001
186.36	3.43E-001	2.24E+002	4.22E-004	9.05E-002	1.80E-001	3.87E+001
238.02	3.54E-001	2.26E+002	1.73E-004	2.90E-002	9.40E-002	1.58E+001
338.64	3.63E-001	2.27E+002	6.21E-005	7.33E-003	4.77E-002	5.64E+000
588.05	3.70E-001	2.28E+002	1.95E-005	1.33E-003	2.56E-002	1.74E+000
2202.89	3.76E-001	2.28E+002	2.01E-006	3.65E-005	8.54E-003	1.55E-001

DH adsorption pore size distribution data is tabulated in Table-3

Table-3

Diameter	Pore Vol	Pore Surf Area	Dv(d)	Ds(d)	Dv(log d)	Ds(log d)
Å	[cc/g]	[m²/g]	[cc/Å/g]	[m²/Å/g]	[cc/g]	[m²/g]
28.05	6.16E-003	9.17E+000	4.69E-003	6.69E+000	2.90E-001	4.32E+002
29.46	1.30E-002	1.88E+001	4.87E-003	6.61E+000	3.16E-001	4.48E+002
30.96	1.97E-002	2.80E+001	4.63E-003	5.98E+000	3.16E-001	4.26E+002
32.65	2.79E-002	3.84E+001	4.57E-003	5.60E+000	3.29E-001	4.21E+002
34.37	3.38E-002	4.55E+001	3.92E-003	4.57E+000	2.97E-001	3.61E+002
36.17	4.14E-002	5.44E+001	3.93E-003	4.35E+000	3.13E-001	3.62E+002
38.22	4.86E-002	6.22E+001	3.63E-003	3.80E+000	3.06E-001	3.34E+002
40.35	5.60E-002	6.98E+001	3.50E-003	3.47E+000	3.11E-001	3.22E+002
42.63	6.30E-002	7.67E+001	3.10E-003	2.91E+000	2.91E-001	2.85E+002
45.14	7.03E-002	8.35E+001	2.89E-003	2.56E+000	2.87E-001	2.66E+002
47.92	7.79E-002	9.01E+001	2.72E-003	2.27E+000	2.87E-001	2.50E+002
51.05	8.55E-002	9.63E+001	2.36E-003	1.85E+000	2.66E-001	2.17E+002
54.52	9.34E-002	1.02E+002	2.31E-003	1.69E+000	2.77E-001	2.12E+002
58.38	1.02E-001	1.09E+002	2.29E-003	1.57E+000	2.94E-001	2.11E+002
62.86	1.11E-001	1.15E+002	1.89E-003	1.20E+000	2.62E-001	1.74E+002
68.16	1.21E-001	1.21E+002	1.80E-003	1.06E+000	2.70E-001	1.66E+002
74.18	1.31E-001	1.26E+002	1.62E-003	8.76E-001	2.65E-001	1.50E+002
81.14	1.42E-001	1.32E+002	1.53E-003	7.53E-001	2.73E-001	1.41E+002
89.52	1.53E-001	1.37E+002	1.30E-003	5.80E-001	2.56E-001	1.20E+002
99.96	1.67E-001	1.43E+002	1.18E-003	4.72E-001	2.60E-001	1.09E+002
113.14	1.80E-001	1.48E+002	9.78E-004	3.46E-001	2.44E-001	9.00E+001
130.46	1.96E-001	1.53E+002	8.28E-004	2.54E-001	2.38E-001	7.62E+001
153.51	2.15E-001	1.58E+002	7.56E-004	1.97E-001	2.55E-001	6.94E+001
186.78	2.37E-001	1.63E+002	5.50E-004	1.18E-001	2.26E-001	5.05E+001
239.98	2.61E-001	1.67E+002	3.90E-004	6.50E-002	2.05E-001	3.57E+001
341.75	2.91E-001	1.71E+002	2.29E-004	2.68E-002	1.70E-001	2.08E+001
594.61	3.18E-001	1.73E+002	7.64E-005	5.14E-003	9.69E-002	6.81E+000
2207.65	3.37E-001	1.73E+002	6.83E-006	1.24E-004	2.79E-002	5.28E-001

DH desorption pore size distribution data is tabulated in Table-4

Table-4

Diameter	Pore Vol	Pore Surf Area	Dv(d)	Ds(d)	Dv(log d)	Ds(log d)
Å	[cc/g]	[m²/g]	[cc/Å/g]	[m²/Å/g]	[cc/g]	[m²/g]
28.03	5.53E-003	8.23E+000	3.80E-003	5.43E+000	2.35E-001	3.50E+002
29.48	1.05E-002	1.52E+001	3.73E-003	5.06E+000	2.42E-001	3.43E+002
30.95	1.58E-002	2.25E+001	3.62E-003	4.68E+000	2.47E-001	3.34E+002
32.49	2.12E-002	2.94E+001	3.67E-003	4.52E+000	2.63E-001	3.38E+002
34.26	2.96E-002	3.97E+001	4.39E-003	5.12E+000	3.31E-001	4.04E+002
36.2	4.02E-002	5.18E+001	5.82E-003	6.43E+000	4.64E-001	5.36E+002
38.14	5.32E-002	6.61E+001	6.82E-003	7.15E+000	5.73E-001	6.28E+002
40.28	7.06E-002	8.41E+001	7.97E-003	7.92E+000	7.08E-001	7.34E+002
42.65	8.76E-002	1.01E+002	7.20E-003	6.75E+000	6.77E-001	6.63E+002
45.22	9.81E-002	1.10E+002	4.08E-003	3.61E+000	4.07E-001	3.76E+002
48.01	1.08E-001	1.20E+002	3.76E-003	3.13E+000	3.98E-001	3.46E+002
51.13	1.20E-001	1.29E+002	3.53E-003	2.76E+000	3.97E-001	3.25E+002
54.62	1.31E-001	1.37E+002	3.27E-003	2.40E+000	3.94E-001	3.01E+002
58.47	1.43E-001	1.46E+002	2.92E-003	2.00E+000	3.76E-001	2.69E+002
62.96	1.55E-001	1.54E+002	2.74E-003	1.74E+000	3.80E-001	2.52E+002
68.16	1.69E-001	1.62E+002	2.60E-003	1.53E+000	3.91E-001	2.40E+002
74.03	1.84E-001	1.71E+002	2.55E-003	1.38E+000	4.16E-001	2.35E+002
81.1	2.03E-001	1.81E+002	2.49E-003	1.23E+000	4.44E-001	2.29E+002
89.54	2.24E-001	1.91E+002	2.45E-003	1.10E+000	4.83E-001	2.26E+002
100.07	2.49E-001	2.01E+002	2.13E-003	8.52E-001	4.70E-001	1.96E+002
113.51	2.74E-001	2.10E+002	1.77E-003	6.24E-001	4.42E-001	1.63E+002
129.99	2.97E-001	2.18E+002	1.34E-003	4.13E-001	3.84E-001	1.23E+002
153.03	3.16E-001	2.23E+002	6.92E-004	1.81E-001	2.33E-001	6.35E+001
186.36	3.32E-001	2.26E+002	4.26E-004	9.15E-002	1.75E-001	3.91E+001
238.02	3.42E-001	2.28E+002	1.75E-004	2.94E-002	9.11E-002	1.60E+001
338.64	3.51E-001	2.29E+002	6.30E-005	7.44E-003	4.64E-002	5.72E+000
588.05	3.58E-001	2.30E+002	1.98E-005	1.35E-003	2.49E-002	1.77E+000
2202.89	3.63E-001	2.30E+002	2.04E-006	3.70E-005	8.29E-003	1.57E-001

Surface area data is tabulated in Table-5

Table-5

Multipoint BET	210.3m²/g
BJH Method Cumulative Adsorption Surface Area	171.5m²/g
BJH Method Cumulative Desorption Surface Area	227.7m²/g
DH Method Cumulative Adsorption Surface Area	173.1m²/g
DH Method Cumulative Desorption Surface Area	229.7m²/g
t-Method External Surface Area	210.3m²/g
t-Method Micro Pore Surface Area	0.000 m²/g

Pore volume data is tabulated in Table-6

Table-6

Total Pore Volume for pores with Diameter less than 3636.6 Å at P/Po = 0.99465	0.3659cc/g
BJH Method Cumulative Adsorption Pore Volume	0.3481cc/g
BJH Method Cumulative Desorption Pore Volume	0.3755cc/g
DH Method Cumulative Adsorption Pore Volume	0.3369cc/g
DH Method Cumulative Desorption Pore Volume	0.3631cc/g
t-Method Micro Pore Volume	0.000cc/g
HK Method Cumulative Pore Volume	0.1342cc/g
SF Method Cumulative Pore Volume	0.1350cc/g

Pore size data is tabulated in Table-7

Table-7

BJH Method Adsorption Pore Diameter (Mode)	29.46Å
BJH Method Desorption Pore Diameter (Mode)	40.28Å
DH Method Adsorption Pore Diameter (Mode)	29.46Å
DH Method Desorption Pore Diameter (Mode)	40.28Å
HK Method Pore Width(Mode)	4.315Å
SF Method Pore Diameter (Mode)	4.569Å

Conclusion:

A) Multi BET Surface of sample is found to be 210.3m²/g.

B) Total Pore Volume for pores with Diameter less than 3636.6 Å at P/Po = 0.99465 is found to be 0.3659cc/g.

Disclaimer:

The above test result relate to sample submitted to the lab for testing and not to any other sample or sample lot. The laboratory shall not be held financially liable for losses incurred by clients on account of inferences and interpretations made on the basis of the test results. The lab shall also not be responsible to stand by the results of sample taken away from lab by the client. Whenever required, this test report shall be reproduced only in full and not in part and this shall be done with the written permission of the lab. This is report is for information purpose only and ABSTC is not responsible for any legal/ statutory implications in the regard.

Appendix E

Thermophysical Properties

E.1   Properties of air

Molecular weight (M)

$M = 28.96$

Thermal conductivity of air (k_{air}) [72]

$$k_{\text{air}} = \frac{1.195 \times 10^{-3} T^{1.6}}{118 + T} \tag{E.1}$$

Dynamic viscosity of air (μ_{air}) [72]

$$\mu_{\text{air}} = \frac{1.488 \times 10^{-6} T^{\frac{3}{2}}}{118 + T} \tag{E.2}$$

Density of air (ρ_{air}) [72]

$$\rho_{\text{air}} = (3.4833 \times 10^7)\left(\frac{P}{T}\right) \tag{E.3}$$

The pressure P is in Pa.

Specific isobaric heat capacity of air ($C_{p,\text{air}}$) [72]

$$C_{p,\text{air}} = (1 + 2.5 \times 10^{-10} T^3) \times 10^3 \tag{E.4}$$

E.2   Properties of nitrogen (N₂), methane (CH₄) and oxygen (O₂)

The molecular weight of N_2, CH_4 and O_2 are tabulated in Table E.1. Densities were calculated using the ideal gas law. Thermal conductivities were calculated using Chapman-Enskog and Eucken's empirical expressions [49] for monoatomic and polyatomic gases respectively

Table E.1

Molecular weights of N_2, CH_4 and O_2 [49]

Gas	Molecular weight (kg/kmol)
N_2	28.03
CH_4	16.04
O_2	32.08

Specific heat

$$C_{p,g} = a_1 + (b_1 \times 10^{-3})T + (c_1 \times 10^{-6})T^2 + (d_1 \times 10^{-9})T^3 \tag{E.5}$$

where $C_{p,g}$ is in kJ/kmol.K and T is in K. The values of a_1, b_1, c_1 and d_1 are given in Table E.2

Table E.2

Values of constants for estimating specific heat using expression (E.5) [73]

Gas component	a_1	b_1	c_1	d_1
N_2	29.5909	−5.1410	13.1829	−4.9680
CH_4	19.2494	52.1135	11.9730	−11.3173
O_2	26.0257	11.7551	−2.3426	−0.5623

E.3   Properties of solids

The molecular weights and density of copper (Cu), copper (II) oxide (CuO) and alumina (Al_2O_3) are tabulated in Table E.3

Table E.3

Properties of Cu, CuO and Al_2O_3 [70, 74, 75, 76]

Solid component	Molecular weight (kg/kmol)	Density (kg/m^3)	Thermal conductivity* (W/m K)
Cu	63.50	8920	354 – 368
CuO	79.50	6400	5 – 7
Al_2O_3	101.96	3965	8.1 – 10.91

* In the temperature range of 773 – 973 K

Specific heat

$$C_{p,s} = A + (B \times 10^{-3})T + (C \times 10^{-5})T^2 \tag{E. 8}$$

where $C_{p,s}$ is in J/kg.K and T is in K. The values of A, B and C are given in Table E.4

Table E.4

Values of constants for estimating specific heat using expression (E.8) [73]

Solid component	A	B	C
Cu	382	7.46	6.76
CuO	430	4.26	−15.30
Al_2O_3	843	5.40	−16.10

Appendix F

Experimental Data – UMC based Heat Transfer Investigations

Table F.1

Experimental data -UMC based heat transfer investigations

Run No	Flowrate (indicated) (LPM)				Flowrate (actual) (LPM)				Inlet temperature (K)	Coolant air ΔT (K)	Conversion[a]		Total heat generated in 7 cycles (kJ)*	External power supply (%)		Total heat transfer to coolant air in 7 cycles	
	Zero air	CH_4	N_2	Coolant air	Zero air	CH_4	N_2	Coolant air			Oxidation	Reduction		Total in 7 cycles	In 6th and 7th cycles	Amount (kJ)	(% of Total)
1	5	2	18	125	31.2	12.5	112.3	300	873.15	28	0.65	0.71	3783 ± 79	48	11	2005 ± 41	53 ± 1
2	10	2	18	125	62.4	12.5	112.3	300	873.15	39	0.77	0.80	3956 ± 92	42	9	3204 ± 78	81 ± 2
3	15	2	18	125	93.6	12.5	112.3	300	873.15	48	0.85	0.80	3686 ± 67	32	6	3170 ± 73	86 ± 2
4	20	2	18	125	124.8	12.5	112.3	300	873.15	47	0.80	0.80	3889 ± 62	41	8	3383 ± 78	87 ± 2
5	15	4	16	125	93.6	25.0	99.8	300	873.15	47	0.84	0.85	3702 ± 66	38	6	3220 ± 74	87 ± 2
6	15	6**	14	125	93.6	37.4	87.4	300	873.15	41	0.86	0.76	3375 ± 84	32	5	2328 ± 68	69 ± 2
7	15	2	18	100	93.6	12.5	112.3	240	873.15	46	0.85	0.80	2458 ± 42	20	3	1917 ± 49	78 ± 2
8	15	2	18	150	93.6	12.5	112.3	360	873.15	33	0.85	0.80	3856 ± 71	35	7	3663 ± 77	95 ± 2
9	15	2	18	175	93.6	12.5	112.3	420	873.15	29	0.85	0.80	3920 ± 73	41	9	3646 ± 78	93 ± 2
10	15	2	18	125	93.6	12.5	112.3	300	898.15	53	0.87	0.87	3663 ± 65	35	6	3113 ± 73	85 ± 2
11	15	2	18	125	93.6	12.5	112.3	300	923.15	55	0.90	0.89	4256 ± 88	40	8	3872 ± 126	91 ± 3

a   Conversion uncertainty is ± 0.03

*   Total heat generated includes heat generated due to reactions (oxidation and reduction) and from external power supply

**   Reduction cycle time was reduced to 5 minutes in this case.

Appendix G

Temperature Profiles – UMC based Heat Transfer Studies

In UMC – heat transfer studies, the temperature at different axial and radial locations in the OSRM bed have been measured at regular intervals of time. The bed temperature profiles with time, at two different radial (TI – 12 and TI – 14) and axial (TI – 14 and TI – 18) locations, are presented and discussed in section 7.1 (Figs. 7.1 – 7.4 and 7.8 – 7.11). The profiles obtained at same radial and axial locations for different selected runs (extreme cases of parametric studies) have been presented here in this Appendix. The trends were similar in nature and can be explained on the lines of the discussion presented in section 7.1. For a change in a specific parameter, all other operating conditions were maintained same as those in run 1 (Table 7.1).

Temperature profiles (Effect of zero air flowrate)
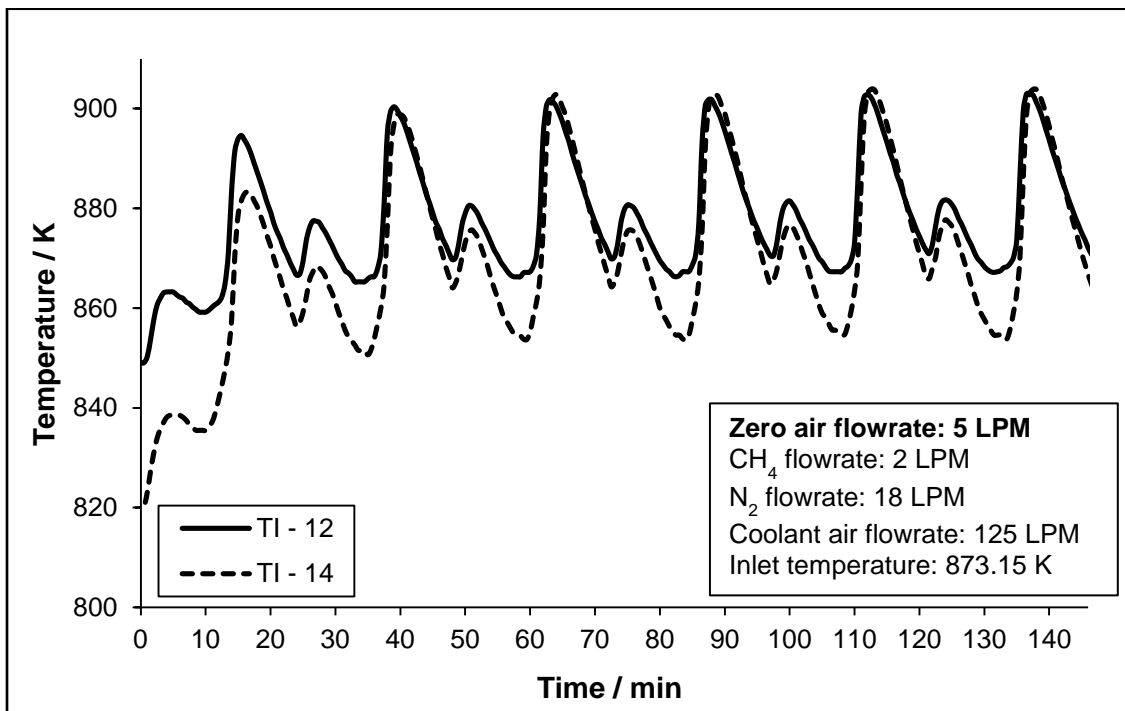
Fig. G.1 Variation of bed temperature with time at two radial locations for zero air flowrate of 5 LPM
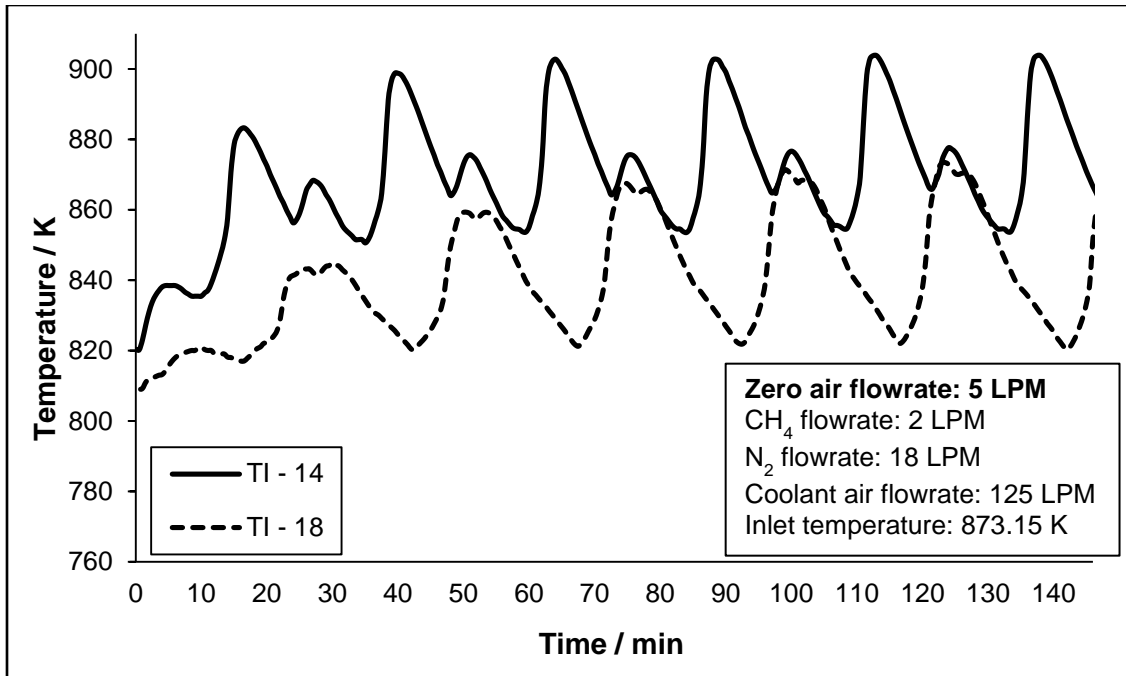
Fig. G.2 Variation of bed temperature with time at two axial locations for zero air flowrate of 5 LPM

Fig. G.3 Variation of bed temperature with time at two radial locations for zero air flowrate of 20 LPM

Fig. G.4 Variation of bed temperature with time at two axial locations for zero air flowrate of 20 LPM

Temperature Profiles (Effect of methane flowrate)

Fig. G.5 Variation of bed temperature with time at two radial locations for methane flowrate of 4 LPM
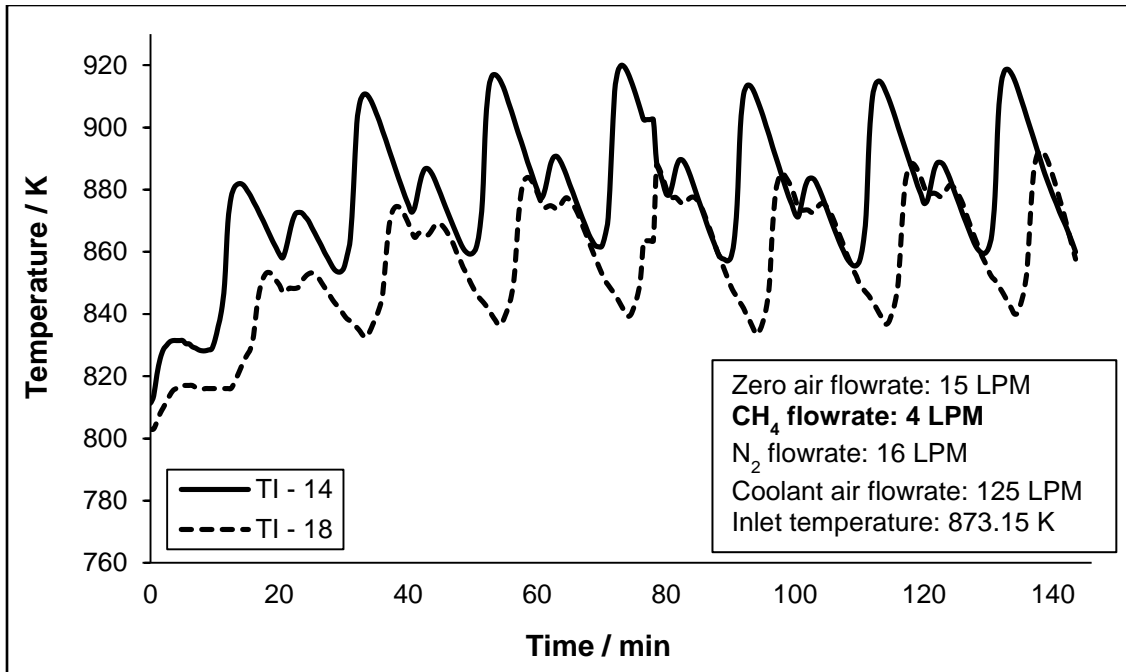
Fig. G.6 Variation of bed temperature with time at two axial locations for methane flowrate of 4 LPM

Fig. G.7 Variation of bed temperature with time at two radial locations for methane flowrate of 6 LPM
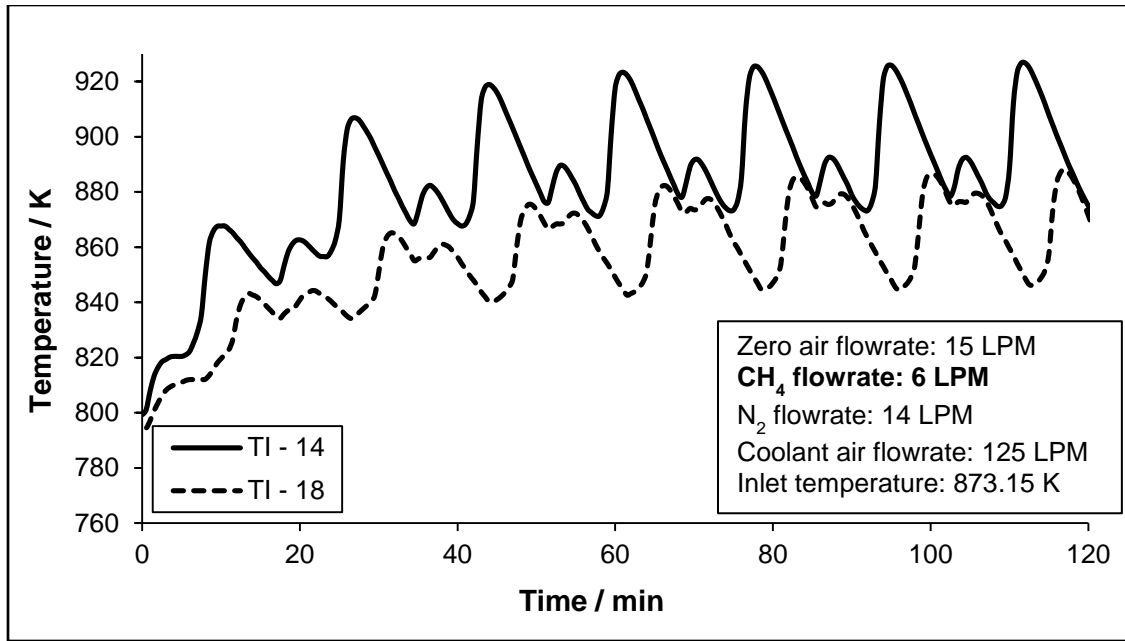
Fig. G.8 Variation of bed temperature with time at two axial locations for methane flowrate of 6 LPM
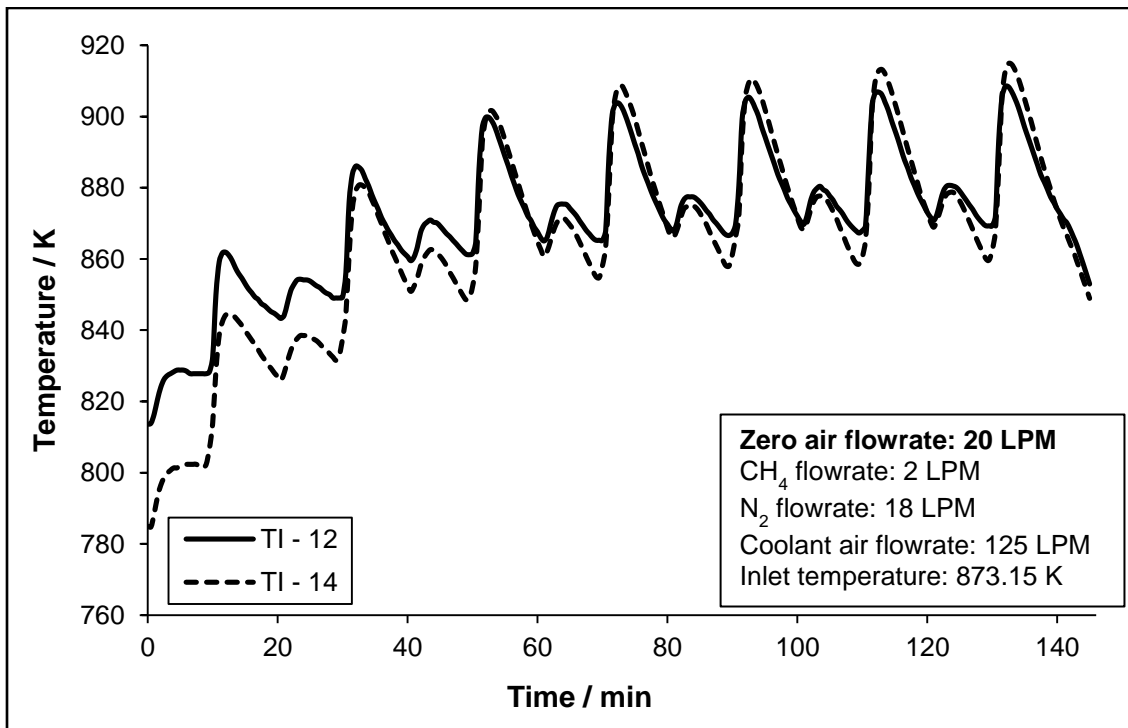
Temperature Profiles (Effect of coolant air flowrate)
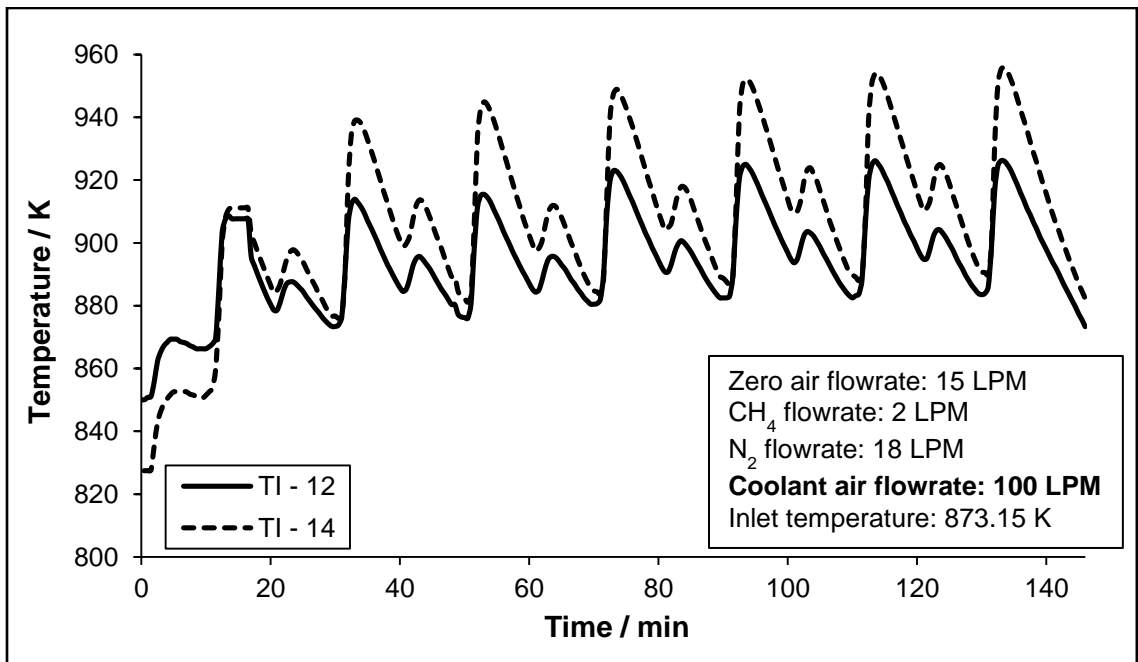
Fig. G.9 Variation of bed temperature with time at two radial locations for coolant air flowrate of 100 LPM
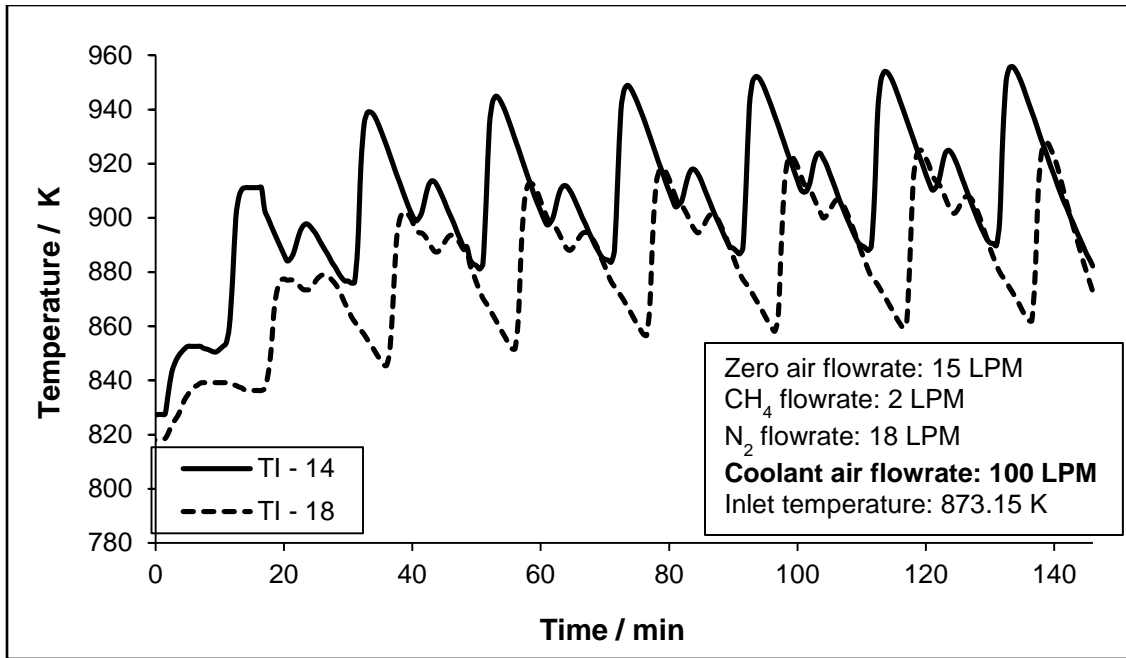
Fig. G.10 Variation of bed temperature with time at two axial locations for coolant air flowrate of 100 LPM
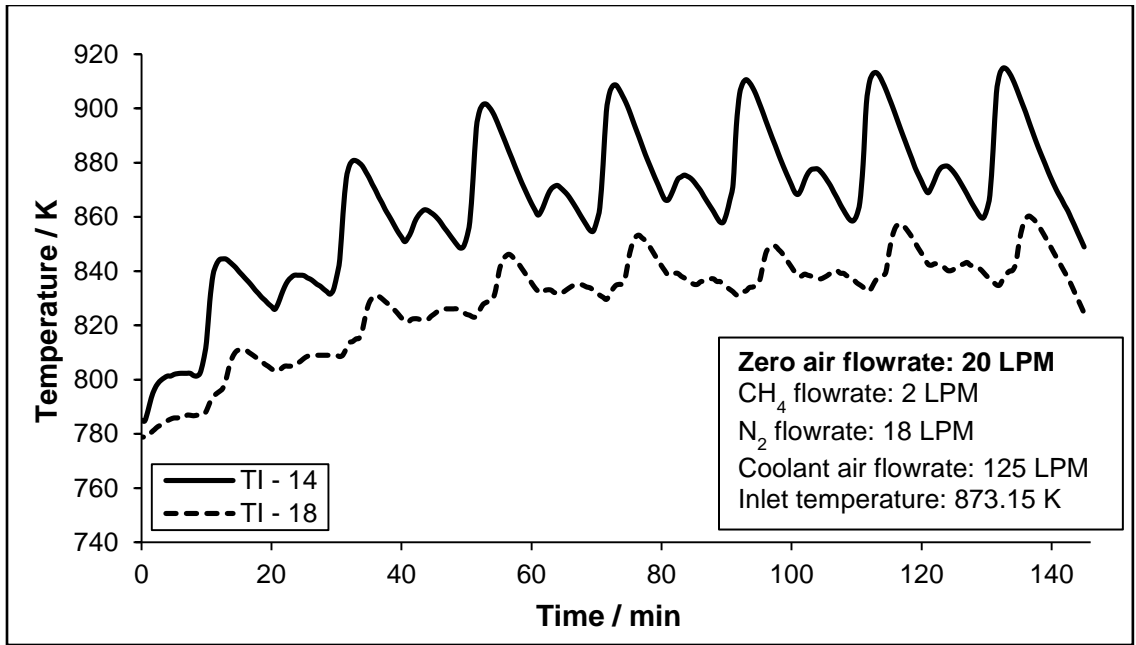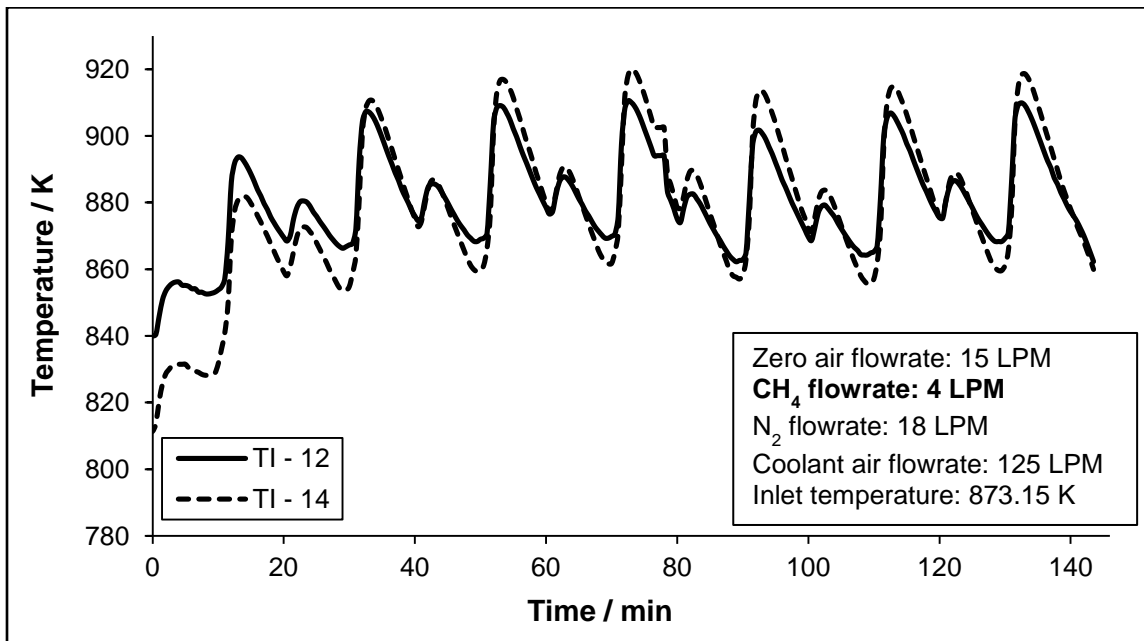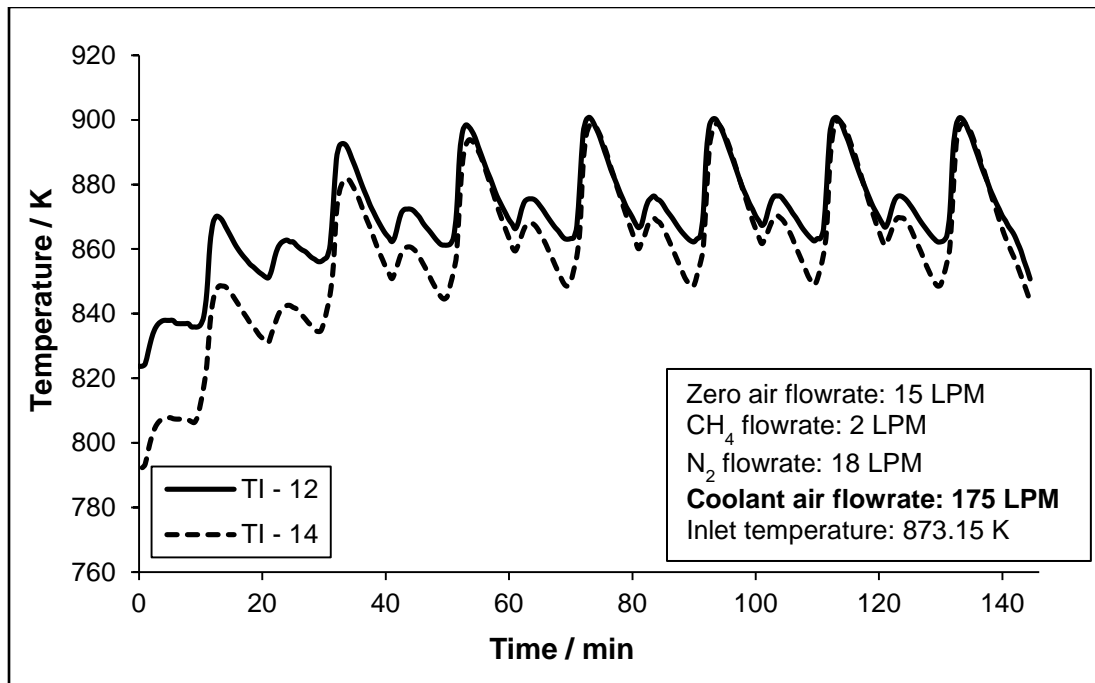

Fig. G.11 Variation of bed temperature with time at two radial locations for coolant air flowrate of 175 LPM
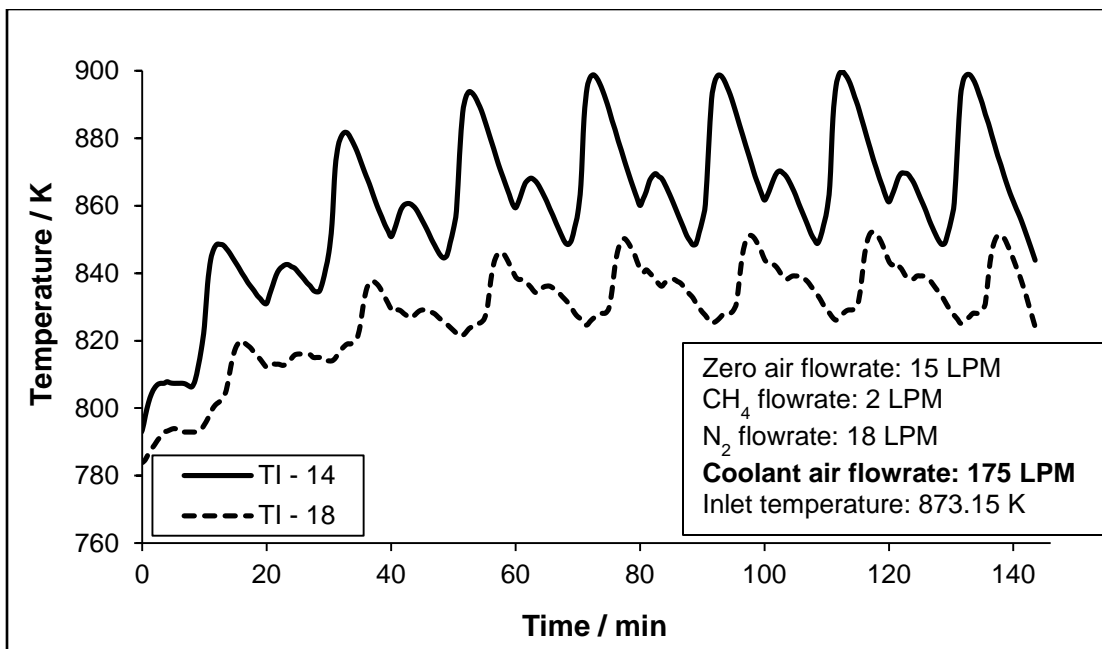
Fig. G.12 Variation of bed temperature with time at two axial locations for coolant air flowrate of 175 LPM

Temperature Profiles (Effect of reactive gas inlet temperature)
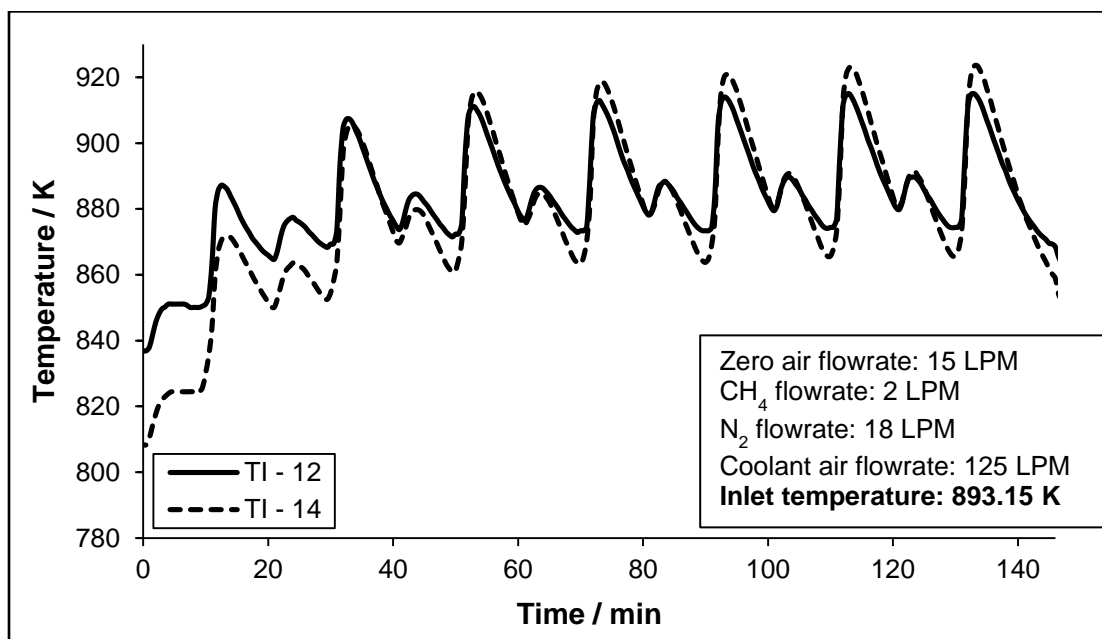
Fig. G.13 Variation of bed temperature with time at two radial locations for reactive gas inlet temperature of 893.15 K
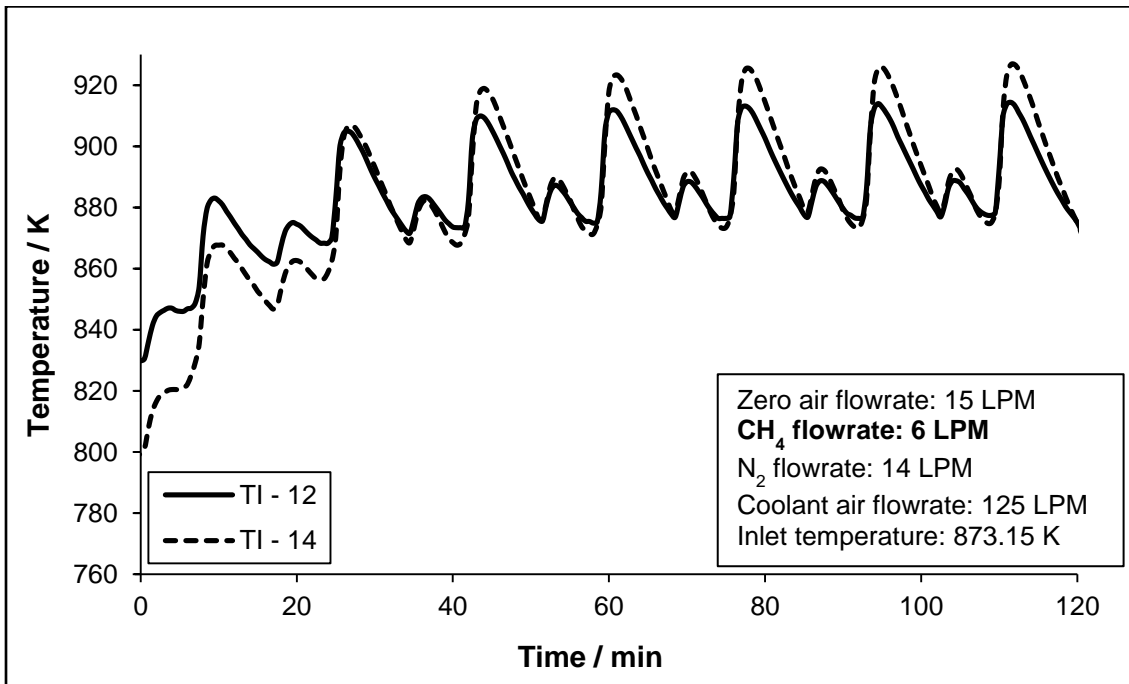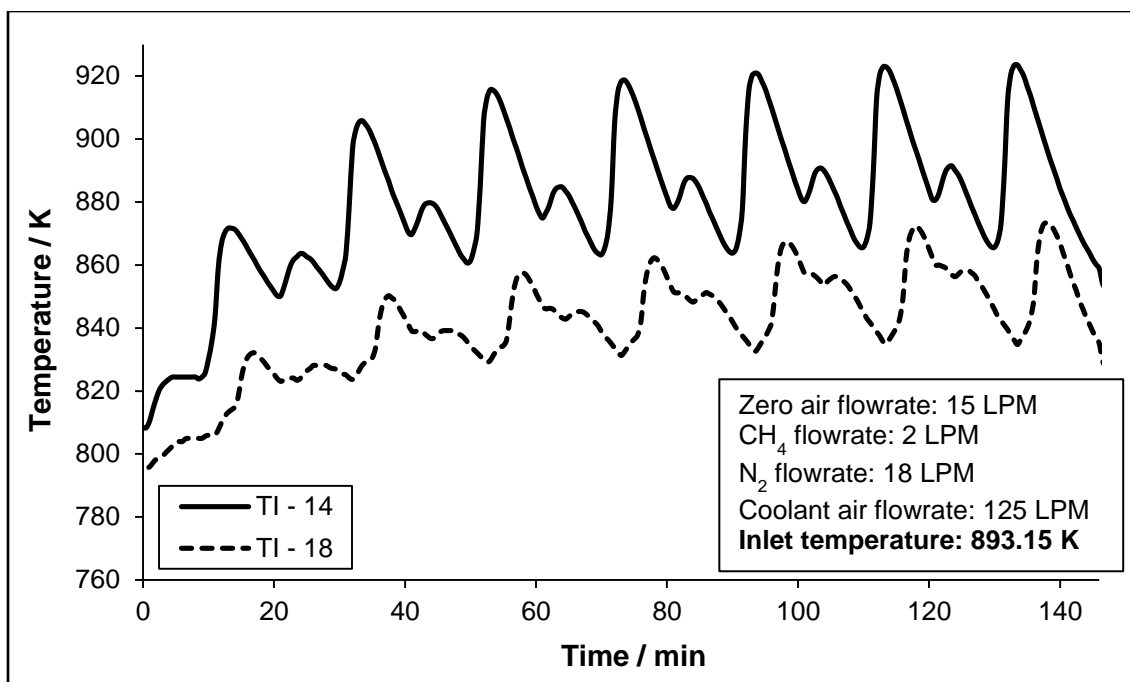
Fig. G.14 Variation of bed temperature with time at two axial locations for reactive gas

inlet temperature of 893.15 K

Appendix H

Dispersion Number

Dispersion number (Di) is defined as the ratio of diffusive transport to convective transport. In case of fluid flow through a tubular or packed bed reactor, the Dispersion number is used to characterize plug flow conditions in the reactor or the extent of axial dispersion. For the values of $Di < 0.001$, the flow inside the reactor can be considered as plug flow and axial dispersion can be neglected [56]. The Dispersion number is estimated based on data from pulse tracer experimentation, in which the effluent concentration of the reactor is first measured as a function of time. Using this data, Di is calculated as

$$Di = \frac{-1 + \sqrt{1 + 8\sigma_\theta^2}}{8} \tag{H.1}$$

where dimensionless parameter σ_θ^2 is estimated from the mean residence time (τ) and the variance (σ_t^2), thus

$$\sigma_\theta^2 = \frac{\sigma_t^2}{\tau^2} \tag{H.2}$$

Mean residence time and variance are obtained from the experimental data using

$$\tau = \frac{\sum (t_j c_j)}{\sum c_j} \tag{H.3}$$

$$\sigma_t^2 = \frac{\sum (t_j^2 c_j)}{\sum c_j} - \left[\frac{\sum (t_j c_j)}{\sum c_j} \right]^2 \tag{H.4}$$

Appendix I

Concentration Data - RTD Study

In order to verify plug flow condition in the PMR system integrated with a GC column, a RTD study was carried out and the obtained concentration vs time data was used to estimate Dispersion number, the results of which are discussed in section 7.2.1.1. Representative data of concentration of O_2 and CH_4 at different times, obtained after injection of respective samples are shown in Table I.1 and Table I.2 respectively.

Table I.1

Concentration of O_2 vs time

Time (s)	Concentration of O_2 (mol/m^3)	Concentration of O_2 (%)
0 – 200	0	0
205	1.68	8
210	2.52	12
215	3.78	18
220	5.04	24
225	3.78	18
230	2.52	12
235	1.68	8
240	0	0

Table I.2

Concentration of CH_4 vs time

Time (s)	Concentration of CH_4 (mol/m^3)	Concentration of CH_4 (%)
0 – 110	0	0
112	0	0
114	2.02	2
116	3.03	3
118	12.11	12
120	66.60	66
122	12.11	12
124	3.03	3
126	2.02	2
128	0	0

Appendix J

Experimental Data - Kinetic Studies

In the PMR – kinetic study, the GC data was used to calculate the fraction of unconverted solid and gas reactants at the end of each pulse. The values of these fractions evaluated during test runs to study oxidation of Cu and reduction of CuO at three different representative temperatures are given in Table J.1 and J.2 respectively. These fractions were then used to determine respective reaction orders and rate constants as given in section 7.2.

The results of rate constants estimated at different temperatures for oxidation and reduction are presented in Table J.3.

Table J.1

Fraction of unconverted solid and gas reactant at each pulse during oxidation of Cu

	673.15 K		773.15 K		873.15 K	
Pulse No	c_{si}/c_{so}	$c_{gi}/c_{go,N}$	c_{si}/c_{so}	$c_{gi}/c_{go,N}$	c_{si}/c_{so}	$c_{gi}/c_{go,N}$
0	1.00	1.00	1.00	1	1.00	1.00
1	0.89	0.93	0.87	0.91	0.84	0.90
2	0.78	0.87	0.74	0.82	0.68	0.80
3	0.68	0.8	0.61	0.73	0.53	0.70
4	0.57	0.73	0.48	0.64	0.37	0.60
5	0.46	0.67	0.36	0.55	0.23	0.51
6	0.36	0.60	0.23	0.45	0.14	0.45
7	0.25	0.53	0.14	0.39	0.08	0.41
8	0.18	0.48	0.09	0.35	0.03	0.38

Table J.2

Fraction of unconverted solid and gas reactant at each pulse during reduction of CuO

Pulse No	873.15 K		923.15 K		973.15 K	
	c_{si}/c_{so}	$c_{gi}/c_{go, N}$	c_{si}/c_{so}	$c_{gi}/c_{go, N}$	c_{si}/c_{so}	$c_{gi}/c_{go, N}$
0	1.00	1.00	1.00	1.00	1.00	1.00
1	0.81	0.85	0.84	0.85	0.83	0.84
2	0.62	0.71	0.68	0.71	0.66	0.69
3	0.43	0.57	0.51	0.57	0.49	0.53
4	0.25	0.43	0.35	0.43	0.32	0.38
5	0.11	0.32	0.20	0.30	0.19	0.27
6	0.03	0.27	0.09	0.20	0.11	0.20

Table J.3

Estimated rate constant at different temperatures for oxidation and reduction

Oxidation		Reduction	
Actual Temperature (K)	Rate constant (k''_1) $(mol^{1-m-n}m^{3m+3n-2}s^{-1})$	Actual Temperature (K)	Rate constant (k''_1) $(mol^{1-m-n}m^{3m+3n-2}s^{-1})$
681.15	2.76E-07	878.15	4.43E-08
705.15	2.84E-07	902.15	5.39E-08
730.15	3.54E-07	930.15	7.42E-08
756.15	3.62E-07	952.15	8.93E-08
783.15	4.16E-07	978.15	9.40E-08
805.15	4.36E-07		
831.15	5.01E-07		
857.15	4.49E-07		
880.15	4.90E-07		

Appendix K

Correlations for Effective Transport Parameters

The correlations of effective radial mass dispersion coefficient, radial thermal conductivity and heat transfer coefficient used in the model simulation are presented here.

Effective radial mass dispersion coefficient (D_{er}) [50]

$$\frac{1}{Pe_{\mathrm{m},r}} = \frac{0.09}{1 + \dfrac{10}{Re_{\mathrm{p}}\, Sc}} + \frac{0.4}{\left(Re_{\mathrm{p}}\, Sc\right)^{0.8}} \tag{K.1}$$

where

$$Pe_{\mathrm{m},r} = \frac{d_{\mathrm{p}} v_{\mathrm{g}}}{D_{er}} \tag{K.2}$$

$$Re_{\mathrm{p}} = \frac{\rho_{\mathrm{g}} d_{\mathrm{p}} v_{\mathrm{g}}}{\mu} \tag{K.3}$$

$$Sc = \frac{\mu}{\rho_{\mathrm{g}} D_{AB}} \tag{K.4}$$

Effective radial thermal conductivity (λ_{er}) [50]

$$\lambda_{er} = \lambda_{\mathrm{e}}^{0} + \lambda_{\mathrm{e}}^{\mathrm{d}} \tag{K.5}$$

where

$$\frac{\lambda_e^0}{\lambda_g} = \varepsilon_g + (1 - \varepsilon_g) \left[\frac{0.895}{0.03 + \frac{2}{3} \frac{\lambda_g}{\lambda_s}} \right] \tag{K.6}$$

$$\lambda_e^d = \frac{0.0025}{1 + 46 \left(\frac{d_p}{d_t}\right)^2} Re_p \tag{K.7}$$

Effective heat transfer coefficient (h_e) [50]

$$\frac{1}{h_e} = \frac{1}{h_w} + \frac{1}{h_c} \tag{K.8}$$

where h_c is calculated using Dittus $-$ Boelter equation and h_w is calculated using the following expression

$$\frac{h_w d_p}{\lambda_{er}} = 0.186 Re_p{}^{0.8} \tag{K.9}$$

References

1. R. K. Lyon, Unmixed combustion: A new technology for prevention of puffing by rotary kiln incinerators and other applications, 205th ACS National meeting in Denver, Colorado 38 (2) (1993).

2. R. K. Lyon, N. J. Pittstown, Methods and systems for heat transfer by unmixed combustion, U. S. Patent 005827496 (1998).

3. R. K. Lyon, J. A. Cole, Unmixed combustion: An alternative to fire, Combust. Flame 121 (2000) 249–261.

4. G. Rizeq, P. Kulkarni, R. Subia, W. Wei, Catalytic unmixed combustion of coal with zero pollution, Technical report, GE (2005).

5. J. A. Pihl, C. S. Daw, V. K. Chakravarthy, J. Conkliln, T. M. Besmann, T. J. Toops, R. L. Graves, Unmixed combustion for high-efficiency energy conversion − Project No. 5179 Laboratory directed research and development program − Annual report, Oak Ridge National Laboratory (2008) 27–28.

6. J. A. Pihl, C. S. Daw, V. K. Chakravarthy, J. Conkliln, T. M. Besmann, T. J. Toops, R. L. Graves, Unmixed combustion for high-efficiency energy conversion − Project No. 5179 Laboratory directed research and development program − Annual report, Oak Ridge National Laboratory (2009) 126–127.

7. H. J. Richter, K. F. Knoche, Reversibility of combustion processes, ACS Symposium Series 235 (1983) 71–85.

8. A. Lyngfelt, B. Leckner, T. Mattisson, A fluidized bed combustion process with inherent CO_2 separation; application of chemical-looping combustion, Chem. Eng. Sci. 56 (2001) 3101–3113.

9. E. Jerndal, T. Mattisson, A. Lyngfelt, Thermal analysis of chemical looping

combustion, Chem. Eng. Res. Des. 84 (A9) (2006) 795–806.

10. M. M. Hossain, I. H. de Lasa, Chemical-looping combustion (CLC) for inherent CO_2 separations – a review, Chem. Eng. Sci. 63 (2008) 4433–4451.

11. H. Fang, L. Haibin, Z. Zengli, Advancements in development of chemical-looping combustion: A review, Int. J. Chem. Eng. Sci. 2009 (2009) 1–16.

12. J. Adanez, A. Abad, F. Garcia – Labiano, P. Gayan, L. F. de Diego, Progress in chemical looping combustion and reforming technologies – a review, Prog. Energy Combust. Sci. 38 (2012) 215–282.

13. S. Noorman, M. van Sint Annaland, H. Kuipers, Packed bed reactor technology for chemical-looping combustion, Ind. Eng. Chem. Res. 46 (2007) 4212–4220.

14. S. Noorman, M. van Sint Annaland J. A. M. Kuipers, Experimental validation of packed bed chemical-looping combustion, Chem. Eng. Sci. 65 (2010) 92–97.

15. S. Noorman, F. Gallucci, M. van Sint Annaland, J. A. M. Kuipers, Experimental investigation of chemical looping combustion in packed beds: A parametric study, Ind. Eng. Chem. Res. 50 (2011) 1968–1980.

16. P. Cho, T. Mattison, A. Lyngfelt, Comparison of iron-, nickel-, copper- and manganese-based oxygen carriers for chemical looping combustion, Fuel 83 (2004) 1215–1225.

17. L. F. de Diego, F. Garcia – Labiano, J. Adanez, P. Gayan, A. Abad, B. M. Corbella, J. M. Palacios, Development of Cu-based oxygen carriers for chemical-looping combustion, Fuel 83 (2004) 1749–1757.

18. J. Adanez, L. F. de Diego, F. Garcia – Labiano, P. Gayan, A. Abad, Selection of oxygen carriers for chemical-looping combustion, Energy Fuels 18 (2004) 371–377.

19. A. Albert, J. Adanez, F. Garcia − Labiano, L. F. de Diego, P. Gayan, J. Celaya, Mapping of the range of operational conditions for Cu-, Fe-, and Ni-based oxygen carriers in chemical-looping combustion, Chem. Eng. Sci. 62 (2007) 533–549 .

20. S. Y. Chuang, J. S. Dennis, A. N. Hayhurst, S. A. Scott, Development and performance of Cu based oxygen carriers for chemical-looping combustion, Combust. Flame 154 (2008) 109–121.

21. M. K. Chandel, A. Hoteit, A. Delebarre, Experimental investigation of some metal oxides for chemical looping combustion in a fluidized bed reactor, Fuel 88 (2009) 898–908.

22. S. Noorman, F. Gallucci, M. van Sint Annaland, H. J. A. M. Kuipers, Experimental investigation of a CuO/Al_2O_3 oxygen carrier for chemical-looping combustion, Ind. Eng. Chem. Res. 49 (2010) 9720–9728.

23. F. Garcıa-Labiano, L. F. De Diego, J. Adanez, A. Abad, P. Gayan, Reduction and oxidation kinetics of a copper-based oxygen carrier prepared by impregnation for chemical-looping combustion, Ind. Eng. Chem. Res. 43 (2004) 8168–8177.

24. J. L. Dirion, C. Reverte, M. Cabassud, Kinetic parameter estimation from TGA: Optimal design of TGA experiments, Chem. Eng. Res. Des. 86 (2008) 618–625.

25. V. Prigiobbe, A. Polettini, R. Baciocchi, Gas-solid carbonation kinetics of air pollution control residues for CO_2 storage, Chem. Eng. J. 148 (2009) 270–278.

26. S. M. Al-Salem, P. Lettieri, Kinetic study of high density polyethylene (HDPE) pyrolysis, Chem. Eng. Res. Des. 88 (2010) 1599–1606.

27. A. Abad, J. Adanez, A. Cuadrat, F. Garcia − Labiano, P. Gayan, L. F. de Diego, Kinetics of redox reactions of ilmenite for chemical-looping combustion, Chem. Eng. Sci. 66 (2011) 689–702.

28. K. Slopiecka, P. Bartocci, F. Fantozzi, Thermogravimetric analysis and kinetic study of poplar wood pyrolysis, Appl. Energy 97 (2012) 491–497.

29. J. T. Gleaves, J. R. Ebner, T. C. Kuechler, Temporal Analysis of Products (TAP) – A unique catalyst evaluation system with sub millisecond time resolution, Catal. Rev. Sci. Eng. 30 (1988) 49 –116.

30. G. S. Yablonsky, M. Olea, G. B. Marin, Temporal analysis of products: basic principles, applications, and theory, J. Catal. 216 (2003) 120–134.

31. J. T. Gleaves, G. Yablonsky, X. Zheng, R. Fushimi, P. L. Mills, Temporal analysis of products (TAP)—Recent advances in technology for kinetic analysis of multi-component catalysts, J. Mol. Catal. A: Chem.315 (2010) 108–134.

32. A. Attar, Pulsed differential reactors and their use for kinetic studies of gas-solid reactions-application to mechanistic studies of the reactions of hydrogen sulfide and the alkaline minerals in coal, Rev. Sci. Instrum. 50 (1979) 111–117.

33. P. Zamostny, Z. Belhohlav, L. Starkbaumova, A multipurpose micro-pulse reactor for studying gas-phase reactions, Chem. Biochem. Eng. Q. 21(2) (2007) 105–113.

34. S. Nand, M. K. Sarkar, Kinetics of thermal cracking of light hydrocarbon mixture by pulsed micro-reactor, The Chem. Eng. J. 17 (1979), 183–190.

35. Y. Li, X. Chang, Z. Zeng, Kinetics study of the isomerization of xylene on HZSM-5 Zeolite. 1. Kinetics model and reaction mechanism, Ind. Eng. Chem. Res. 31 (1992) 187–192.

36. A. M. Sica, E. M. Valles, C. E. Gigola, Kinetic data from a pulse microcatalytic reactor – Hydrogenation of benzene on a nickel catalyst, J. Catal. 51 (1978) 115–125.

37. V. R. Choudhary, V. H. Rane, Pulse microreactor studies on conversion of methane, ethane and ethylene over rare earth oxides in the absence and presence of free oxygen, J. Catal. 135 (1992) 310–316.

38. E. Ruckensteim, H. Y. Wang, Effect of support on partial oxidation of methane to synthesis gas over supported rhodium catalysts, J. Catal. 187 (1999) 151–159.

39. Z. Ma, Y. Yue, X. Deng, Z. Gao, Nanosized anatase TiO_2 as precursor for preparation of sulfated titania catalysts, J. Mol. Catal. A: Chem. 178 (2002) 97–104.

40. L. Intriago, E. Diaz, S. Ordonez, A. Vega, Combustion of trichloroethylene and dichloromethane over protonic zeolites: influences of adsorption properties on the catalytic performance, Microporous Mesoporous Mater. 91 (2006) 161–169.

41. D. Ciuparu, E. Altman, L. Pfefferle, Contributions of lattice oxygen in methane combustion over PdO-based catalysts, J. Catal. 203 (2001) 64–74.

42. Z. Renjun, L. Olangkun, Z. Bingchang, C. Hongwu, G. Zhushan, S. Xlaorul, Simultaneous pyrolysis of ethane-propane mixture in pulsed micro-reactor system, Ind. Eng. Chem. Proc. DD. 25 (1986) 12–17.

43. A. Attar, F. Dupuis, The rate and the fundamental mechanisms of the reaction of hydrogen sulfide with the basic minerals in coal, Ind. Eng. Chem. Proc. DD. 18(4) (1979) 607–618.

44. G. F. Froment, K. B. Bischoff, Chemical reactor analysis and design, John Wiley and sons (1979).

45. J. Park, Modeling of transient heterogeneous two-dimensional catalytic packed bed reactor, Korean J. Chem. Eng. 12(1) (1995) 80–87.

46. B. Koning, Heat and mass transport in tubular packed bed reactors at reacting and non-reacting conditions, PhD Thesis, University of Twente (2002).

47. A. A. Lordanidis, Mathematical modeling of catalytic fixed bed reactors, PhD Thesis, University of Twente (2002).

48. H. A. Jakobsen, Chemical reactor modeling – Multiphase reactive flows, Springer – Verlag Berlin Heidelberg (2008).

49. R. B. Bird, W. E. Stewart, E. N. Lightfoot, Transport Phenomena, second ed., Wiley, New York (2002).

50. B. D. Kulkarni, L. K. Doraiswamy, Estimation of effective transport properties in packed bed reactors, Catal. Rev. Sci. Eng. 22(3) (1980) 431–483.

51. B. A. Finlayson, Packed bed reactor analysis by orthogonal collocation, Chem. Eng. Sci. 26 (1971) 1081–1091.

52. R. Khanna, J. H. Seinfeld, Mathematical modeling of packed bed reactors: Numerical solutions and control model development, Adv. Chem. Eng. 13 (1987) 113–191.

53. S. K. Gupta, Numerical methods for chemical engineers, New age international (P) limited publishers, New Delhi (1995).

54. V. V. Ranade, Computational flow modelling for chemical reactor engineering, Academic Press, London (2002).

55. A. E. Varela, J. C. Garcia, Multiphyiscs simulation of a packed bed reactor, COMSOL Conference, Boston (2009).

56. H. S. Fogler, Elements of Chemical Reaction Engineering, Second ed., Prentice Hall: Englewood Cliffs, NJ (1992).

57. V. Balakotaiah, S. M. S. Dommeti, Effective models for packed bed catalytic reactors, Chem. Eng. Sci. 54 (1999) 1621–1638.

58. S. M. S. Dommeti, V. Balakotaiah, Analytical criteria for validity of pseudo-homogeneous models of packed bed catalytic reactors, Ind. Eng. Chem. Res. 38 (1999) 767–777.

59. J. J. Lerou, G. F. Froment, Velocity, temperature and conversion profiles in fixed bed catalytic reactors, Chem. Eng. Sci. 32 (8) (1977) 853–861.

60. P. S. Mehta, W. N. Sams, D. Luss, Wrong-way behavior of packed bed reactors: 1. The pseudo-homogeneous model, AIChE J. 27(2) (1981) 234–246.

61. V. Balakotaiah, E. L. Christoforatou, D. H. West, Transverse concentration and temperature non-uniformities in adiabatic packed-bed catalytic reactors, Chem. Eng. Sci. 54(1) (1999) 1725 –1734.

62. S. A. Logtenberg, M. Nijemeisland, A. G. Dixon, Computational fluid dynamics simulations of fluid flow and heat transfer at the wall-particle contact points in a fixed bed reactor, Chem. Eng. Sci. 54 (13-14) (1999) 2433–2439.

63. A. Srinivasan, One-dimensional pseudo-homogeneous packed bed reactor modeling including NO–CO kinetics, M.Sc. Thesis, University of Kansas (2011).

64. A. Srinivasan, C. Depcik, One-dimensional pseudo-homogeneous packed-bed reactor modeling: I. Chemical species equation and effective diffusivity, Chem. Eng. Tech. 36 (1) (2013) 22–32.

65. A. Srinivasan, C. Depcik, One-dimensional pseudo-homogeneous packed-bed reactor modeling: II. Energy equation and effective thermal conductivity, Chem. Eng. Tech. 36 (3) (2013) 379–389.

66. J. R. Fernandez, J. C. Abanades, R. Murillo, Modeling of Cu oxidation in adiabatic fixed-bed reactor with N_2 recycling in a Ca/Cu chemical loop, Chem. Eng. J. 232 (2013) 442–452.

67. S. Noorman, F. Gallucci, M. van SintAnnaland, J. A. M. Kuipers, A theoretical investigation of CLC in packed beds. Part 1: Particle model, Chem. Eng. J. 167 (2011) 297–307.

68. S. Noorman, F. Gallucci, M. van SintAnnaland, J. A. M. Kuipers, A theoretical investigation of CLC in packed beds. Part 2: Reactor model, Chem. Eng. J. 167 (2011) 369–376.

69. J. M. Smith, Chemical Engineering Kinetics, McGraw-Hill: New York (1981).

70. F. Garcia – Labiano, L. F. de Diego, J. Adanez, A. Abad, P. Gayan, Temperature variations in the oxygen carrier particles during their reduction and oxidation in a chemical looping combustion, Chem. Eng. Sci. 60 (2005) 851–862.

71. J. A. Sofranko, J. F. Leonard, C. A. Jones, The oxidative conversion of methane to higher hydrocarbons, J. Catal. 103 (1987), 302 – 310.

72. S. Krishnaswamy, Filmwise condensation inside a non-circular horizontal tube in the presence of forced convection and a non-condensing gas, PhD Thesis, Queen Mary College, University of London (2004).

73. B. I. Bhatt, S. B. Thakore, Stoichiometry, 5th edition, Tata McGraw-Hill Pvt. Ltd., New Delhi (2010).

74. F. P. Incropera, D. P. Dewitt, T. L. Bergman, A. S. Lavine, Fundamentals of heat and mass transfer, sixth ed., Wiley, UK (2007).

75. Pure Copper (2015, January 2015). Retrieved from http://www-ferp.ucsd.edu/LIB/PROPS/PANOS/cu.html

76. Aluminium oxide (Al_2O_3) (2015, January 2015). Retrieved from http://www-ferp.ucsd.edu/LIB/PROPS/PANOS/al2o3.html

List of Publications

1. **Amol Deshpande,** Srinivas Krishnaswamy, Krishnaswamy Ponnani, Experimental investigations on Unmixed Combustion for heat transfer applications. **Chemical Engineering Science** 164 (2017) 122 – 132. (http://dx.doi.org/10.1016/j.ces.2017.01.072)

2. **Amol Deshpande**, Srinivas Krishnaswamy, Krishnaswamy Ponnani, Pulsed Micro-reactor: An alternative to estimating kinetic parameters of non-catalytic gas-solid reactions. **Chemical Engineering Research and Design** 117 (2017) 382 – 393. (http://dx.doi.org/10.1016/j.cherd.2016.10.044)

3. **Amol Deshpande**, Srinivas Krishnaswamy, Krishnaswamy Ponnani, Experimental studies on unmixed combustion: packed bed reactor technology for heat transfer applications, **AIChE Annual Meeting 2015**, Salt Lake City, Utah, USA, November 8 – 13, 2015 (Conference and Proceedings: **Scopus indexed**)

4. **Amol Deshpande**, Srinivas Krishnaswamy, Krishnaswamy Ponnani, Micro-pulsed differential reactors: a viable alternative for estimating kinetics of gas-solid reactions, 67th Annual session of IIChE, **CHEMCON – 2014**, Chandigarh, December 27 – 30, 2014 (Conference and Proceedings)

5. **Amol Deshpande**, Srinivas Krishnaswamy, Krishnaswamy Ponnani, Modeling of Unmixed Combustion based packed bed reactor system used for heat transfer applications, 69th Annual session of IIChE, **CHEMCON – 2016**, Anna university, Chennai, December 27 – 30, 2016 (Accepted for oral presentation and proceedings)

Curriculum Vitae – Prof. Srinivas Krishnaswamy

Dr. Srinivas is presently a Professor in the Department of Chemical Engineering at BITS Pilani K. K. Birla Goa campus. He obtained his Bachelor's Degree in Chemical Engineering from Shivaji University in 1991 and his Doctoral Degree from the University of London in 2004.

Between 1991 and 1993, he worked as Trainee and Production Engineer at Vijay Kumar refractories and Oswal Petrochemicals respectively. Subsequently in 1993, he was selected to be part of 38th Batch of the one year Training school programme at Bhabha Atomic Research Centre (BARC). On completion of the training programme in 1994, he joined the Chemical Engineering Division at BARC as Scientific Officer. In January 2000, he joined Queen Mary College, University of London to study for a PhD in the area of condensation heat transfer in the presence of a non-condensing gas with emphasis on fuel cell exhaust condensers proposed to be used in vehicles. In August 2003, he joined the University of Sheffield, United Kingdom as a Post-doctoral Research Assistant. In January 2005, he joined the Chemical Engineering Group (presently Department of Chemical Engineering) at BITS Pilani, K K Birla Goa campus as Assistant Professor. He was also a Visiting Professor at the Department of Chemical and Materials Engineering at Lunghwa University of Institute of Science and Technology, Taiwan from May to July 2009.

His main focus of research involves addressing challenges posed in developing practical cost effective, energy efficient and environment friendly systems from a commercialization point of view. His area of research is process intensification. He has successfully completed five research projects and currently working on two more projects, mainly funded by various Government funding agencies and industries. His projects include unmixed combustion for heat transfer applications, new technology for desalination, coke reduction in refinery systems, etc. He has published and presented papers in national and international journals and conferences.

As a teacher, Prof. Srinivas' interests lie in Chemical Engineering Thermodynamics, Chemical Reaction Engineering, Process Design, Modeling and Simulation. Besides teaching and research, Prof. Srinivas has been associated with BITS Pilani administration assuming diverse responsibilities - Group Leader, Chemical Engg. (2006 - 2010), HOD (2010 - 2015), Resident Warden, Faculty-in-charge (Student Sporting Activities), Prof. in-Charge (Chemical Engineering Students Association), Chairperson (Departmental Research Committee), Member of Senate & Faculty Recruitment Committee etc. As part of the Mission 2012 - Vision 2020 initiative of BITS Pilani, he was Task Force leader for the Campus Life thrust area and subsequently with regard to Mission 2015 leads a team involved in Industry Engagement Imperative. More recently he has been appointed as Professor in-Charge (University wide) of the Centre for Innovation, Incubation & Entrepreneurship. He is also an Associate Member of the Institution of Chemical Engineers (IChemE), United Kingdom and Life Member of the Indian Institute of Chemical Engineers (IIChE).

Curriculum Vitae – Mr. Amol Deshpande

Mr. Amol Deshpande has been working as a Lecturer in the Department of Chemical Engineering at BITS Pilani K. K. Birla Goa Campus since June 2010. He obtained his Bachelors and Masters degrees in Chemical Engineering from BITS Pilani, Pilani Campus in 2003 and 2006 respectively. He is also pursuing his PhD at BITS Pilani K. K. Birla Goa, Campus, Goa since August 2011.

Prior joining BITS, he worked in an industry for close to 4 years. He worked as a Field Service Advisor in UOP India Pvt Ltd (A Honeywell Company), Gurgaon in 2006 – 2010, where he was involved in activities related to start-up and commissioning of UOP process units at various petroleum refineries and petrochemical plants in the world. He also worked as a Teaching Assistant while completing his Masters degree (Aug 2003 – Dec 2005) at BITS Pilani, Pilani Campus.

His research areas include Unmixed Combustion for heat transfer, Transport phenomena, Reaction engineering, Modeling and simulation of Chemical engineering processes and Computational Fluid Dynamics (CFD).

He is currently involved in teaching undergraduate and postgraduate Chemical engineering students at BITS Goa and his teaching interests include Transport phenomena, Fluid mechanics, Heat transfer and CFD. He has also guided several undergraduate students on research topics related CFD applications to Chemical engineering problems using COMSOL Multiphysics software.

He is a life member of the Indian Institute of Chemical Engineers (IIChE) since 2014 and a senior member of Americal Institute of Chemical Engineers (AIChE), USA since 2015.